STATISTICAL SHAPE ANALYSIS OF NEUROANATOMICAL STRUCTURES BASED ON SPHERICAL WAVELET TRANSFORMATION

by

PENG YU

Master of Science, Biomedical Engineering
Xi'an Jiaotong University, 2001

Submitted to the Harvard - MIT Division of Health Sciences and Technology
in partial fulfillment of the requirements for the Degree of
Doctor of Philosophy in
Health Sciences and Technology/Radiological Sciences Joint Program
at the

MASSACHUSETTS INSTITUTE OF TECHNOLOGY

FEBRUARY 2008

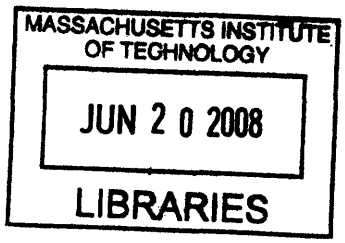

Signature of Author: _____
Harvard - MIT Division of Health Sciences and Technology
February 1, 2008

Certified by: _____
Bruce Fischl, Ph.D.
Associate Professor of Radiology at Harvard Medical School
Thesis Supervisor

Accepted by: _____
Martha L. Gray, Ph.D.
Edward Hood Taplin Professor of Medical and Electrical Engineering
Director, Harvard-MIT Division of Health Sciences and Technology

STATISTICAL SHAPE ANALYSIS OF NEUROANATOMICAL STRUCTURES BASED ON SPHERICAL WAVELET TRANSFORMATION

by

PENG YU

Submitted to the Harvard - MIT Division of Health Sciences and Technology
on Feb. 1, 2008 in partial fulfillment of the
requirements for the Degree of Doctor of Philosophy in
Health Sciences and Technology/Radiological Sciences Joint Program

Abstract

Evidence suggests that morphological changes of neuroanatomical structures may reflect abnormalities in neurodevelopment, or relate to a variety of disorders, such as schizophrenia and Alzheimer's disease (AD). Advances in high-resolution Magnetic Resonance Imaging (MRI) techniques allow us to study these alterations of brain structures *in vivo*. Previous work in studying the shape variations of brain structures has provided additional localized information compared with traditional volume-based study. However, challenges remain in finding an accurate shape presentation and conducting shape analysis with sound statistical principles. In this work, we develop methods for automatically extracting localized and multi-scale shape features and conducting statistical shape analysis of neuroanatomical structures obtained from MR images.

We first develop a procedure to extract multi-scale shape features of brain structures using bi-orthogonal spherical wavelets. Using this wavelet-based shape representation, we build multi-scale shape models and study the localized cortical folding variations in a normal population using Principal Component Analysis (PCA). We then build a shape-based classification framework for detecting pathological changes of cortical surfaces using advanced classification methods, such as predictive Automatic Relevance Determination (pred-ARD), and demonstrate promising results in patient/control group comparison studies. Thirdly, we develop a nonlinear temporal model for studying the temporal order and regional difference of cortical folding development based on this shape representation. Furthermore, we develop a shape-guided segmentation method to improve the segmentation of sub-cortical structures, such as hippocampus, by using shape constraints obtained in the wavelet domain. Finally, we improve upon the proposed wavelet-based shape representation by adopting a newly developed over-complete spherical wavelet transformation and demonstrate its utility in improving the accuracy and stability of shape representations.

By using these shape representations and statistical analysis methods, we have demonstrated promising results in localizing shape changes of neuroanatomical structures related to aging, neurological diseases, and neurodevelopment at multiple spatial scales. Identification of these shape changes could potentially lead to more accurate diagnoses and improved understanding of neurodevelopment and neurological diseases.

Thesis Supervisor: Bruce Fischl
Title: Associate Professor of Radiology at Harvard Medical School
Thesis Committee Chair: Bruce R. Rosen
Title: Professor of Radiology at Harvard Medical School
Thesis Committee: Polina Golland
Title: Assistant Professor of EECS Department and CSAIL at MIT
Thesis Committee: David G. Cory
Title: Professor of Nuclear Engineering at MIT

Acknowledgments

I would like to express my gratitude to all those who helped and supported me over the years to complete this thesis. First and foremost, I would like to thank my thesis advisor, Professor Bruce Fischl at Harvard Medical School, for introducing me to the exciting research area of medical image analysis and giving me generous support and invaluable guidance in the past six years. I met Bruce and visited the group he led in the summer of 2001. I was fascinated with the research direction in his group and expressed my strong interest in working with him on my Ph.D. thesis. I still feel blessed today that Bruce agreed to be my thesis supervisor back then. In the past six year, I have never ceased to admire his extraordinary intellects, clarity of thought and enviable scientific insights. I have learned from him not only the advanced techniques in medial image analysis, but also the ability to analyze and solve scientific problems. Throughout the past six years, Bruce has made him available in the evening and weekend, and has guaranteed an astonishingly fast reply to emails. His scientific guidance and constant encouragement have led me to a place I could not have otherwise reached. I thank him forever for providing such a wonderful environment and the great opportunity for me to learn and grow during my graduate study at MIT.

I am grateful to Professor Bruce R. Rosen, the Director of the Athinoula A. Martinos Center for Biomedical Engineering, for his boundless support over the years and for serving as the chair of my thesis committee. Professor Rosen introduced me to the Athinoula A. Martinos Center for Biomedical Engineering, and the research group led by my thesis advisor. With his extraordinary scientific insights, leadership, and enthusiasm, he has set a role model for me to emulate in my own career.

I am also grateful to Professor Polina Golland at MIT CSAIL for her stimulating advice, close collaboration, and her service on my thesis committee. I greatly benefited from working with her on method development, algorithm implementation and final results presentation. I am especially thankful for her tutoring and help with my scientific writing and presentation skills.

I also give warm thanks to my thesis committee member and academic advisor, Professor David Cory. I met Professor Cory when I started my study at MIT in 2001 and took a class with him before taking the qualification exam. His advice and encouragement have been always inspiring in the past seven years.

I have been very fortunate to work with Dr. Ellen Grant, who is the Chief of Pediatric Radiology at Massachusetts General Hospital. I feel very lucky to work with her on an MRI dataset of newborn for studying neurodevelopment. Her invaluable suggestions, keen insights, and profound experiences on neuroscience have been the driving forces of the success of our collaboration, which has not only led to publications, but also been reported as a feature story in the MIT newspaper.

I would also like to thank Professor Randy Buckner at Harvard University, Professor Randy Gollub at Harvard Medical School, Dr. Arthur Liu and Dr. Russell Poldrack at the Children's Hospital for making their MRI data available and for providing feedback on our work along the way.

This thesis is a multidisciplinary work conducted at Athinoula A. Martinos Center for Biomedical Engineering and MIT. I have been very fortunate to work with many talented scientists and researchers from both institutions. At Athinoula A. Martinos Center, I own much gratitude to all the current and former members of the Freesurfer group, including Evelina Busa, Doug Greve, Xiao Han, Jenni Pacheco, Rudolph Pienaar, Nick Schmansky, Kevin Teich, Thomas Witzel, and Lilla Zollei for their collaborative work in advancing the Freesurfer software package, which I have been relying on throughout my entire thesis work. I am especially thankful to Dr. Xiao Han for his

indispensable help with my thesis work. I have benefited greatly from his enrich experiences in medical image analysis and computer skills. Although we only overlapped for less than two years, he remained evolved with my thesis work since then. I am also very grateful to Dr. Lilla Zollei, who always supports and inspires me in so many ways as both a wonderful friend and the best lab-mate one can ever ask for.

At MIT, I give thanks to my fellow graduate students in the Medical Vision Group at Computer Science and Artificial Intelligence Laboratory, including Anna Custo, Wanmei Ou, Florent Ségonne, and Boon Thye (Thomas) Yeo. I met Florent, who was also supervised by Professor Bruce Fischl, six years ago when I just joined Bruce's group. I am very grateful to Florent for his friendship and strong influence on my thesis work. I deeply appreciated him being actively evolved with my thesis work, and having a weekly meeting with me in our overlapped years. Flo, I owe you much gratitude for all your help. I started collaborating with Thomas in the last two years of my thesis work. His quick wit and strong programming skills have greatly helped me to speed up my thesis work. I give my special thank to Dr. Alan Qi, an expert in Bayesian machine learning, for his tremendous help with my thesis and great collaborative efforts. I admire his incomparable intellect, absolute determination toward excellence for himself and his field of study, as well as his unwavering enthusiasm to scientific research.

I give thanks to my fellow graduate students in HST and Nuclear Engineering Department including Shuning Huang, Thomas Heldt, Jelena Mirkovic, Christopher S. Melhus, Megan Hepler Blackwell, Mark Haig Khachaturian, and Leeland Ekstrom. I am especially thankful to Shuning Huang, who joined the HST/RSJP in the same year, accompanied me during difficult times in the past seven years, and supported me in so many ways. I give special thank to Thomas Heldt, who I have been very fortunate to work with during my first summer at MIT. I admire his dedication to scientific study, as well as his strong linguistic prowess. I am very grateful for having Jelena Mirkovic as my roommate in the past four years. She has been a wonderful friend and a resource of spiritual strength in this long journey. I thank Mitra Osqui for offering to be my teammate in a first class I took at MIT in the spring of 2001, and for being so supportive and inspiring in the past seven years.

Moreover, I extend my thanks to all my Chinese friends with whom I have shared many good times during graduate school. I give special thank to Song Gao, who I spent the majority of my spare time and shared many memorable and happy moments with. Song, my life at MIT would not be so fun without you. I also thank Huiqin Jiang, Yi Zhang, Zhiying Chen, Li Yu, Wei Guo, Xioafeng Qian, Liang Xue, and Lin Han for bringing me so much joy.

I am forever grateful to Professor Roger Mark at HST, who introduced me to and encouraged me to apply to the Harvard-MIT Division of Health Sciences and Technology program during his visit to China in 1999.

Finally, I would like to express my deepest gratitude for the unconditional love and support I received from my family. This thesis is dedicated to my parents and sister.

Contents

1 Introduction **11**

1.1 Motivation 11

1.2 Previous Work 12

1.2.1 Shape Representation Methods 12

1.2.2 Statistical Analysis and Applications 13

1.2.3 Shape Analysis Results 14

1.3 Objective and Contributions 15

1.4 Thesis Overview 16

2 Shape Representation Based on Bi-orthogonal Spherical Wavelets **23**

2.1 Motivation 23

2.1.1 Limitation of Spherical Harmonic Descriptors in Shape Representation 24

2.1.2 Our Methods 25

2.2 Preprocessing 25

2.3 Shape Representation Based on Spherical Wavelets 27

2.3.1 Bi-orthogonal Spherical Wavelets 27

2.3.2 Spherical Wavelet Transformation of Cortical Surfaces 28

2.3.3 Comparison of SPHARM and Wavelets in Shape Representation 30

2.3.4 Applications 32

2.4 Contributions 32

A. Fast Spherical Wavelets Transformation 34

3 Multi-scale Shape Models Based on Principal Component Analysis **39**

3.1 Introduction 39

3.2 Methods 40

3.2.1 Shape Models Based on PCA in the Wavelet Domain 40

3.2.2 Shape Pattern Recognition in Synthetic Data 41

3.3 Experimental Results and Discussions 42

3.3.1 Shape Variation in Aged Normal Population 43

3.3.2 Shape Variation in Neonates 48

3.4 Contributions 48

4 Shape-based Classification **51**

4.1 Motivation 51

4.2 Methods 52

4.2.1 Feature Dimension Reduction in the Wavelet Domain 53
4.2.2 Classification Based on Predictive Automatic Relevance Determination 54
4.2.2 Classification Based on Support Vector Machines 55
4.3 Experimental Setup and Dataset 56
4.4 Results and Discussions. 58
4.4.1 Shape Discrimination of Synthetic Data 58
4.4.2 Shape Discrimination of Patients with Mild Dementia 58
4.4.3 Comparison of Pred-ARD and SVMs 59
4.5. Contributions 60

5 Cortical Folding Development Models 63
5.1 Motivation 63
5.2 Dataset and Methods 64
5.2.1 Dataset and Preprocessing 64
5.2.2 Nonlinear Cortical Folding Development Model 64
5.3 Results and Discussions. 67
5.3.1 Global Folding Development of the Cortical Surface 67
5.3.2 Regional Folding Development of the Cortical Surface. 69
5.3.3 Discussions 71
5.4. Contributions 74

6 Shape-guided Subcortical Structure Segmentation 77
6.1 Motivation 77
6.2 Methods 79
6.2.1 Preprocessing 79
6.2.2 Segmentation Guided with Shape Models in the Wavelet Domain 80
6.3 Experimental Design and Results 83
6.4. Contributions 86

7 Cortical Shape Study Based on Over-complete Spherical Wavelets 89
7.1 Motivation 89
7.1.1 Limitation of Shape Representation Based on Bi-orthogonal Spherical Wavelets . .89
7.1.2 Over-complete Spherical Wavelets 90
7.2 Shape Representation Based on Over-complete Spherical Wavelets 91
7.2.1 Over-complete Spherical Wavelets 91
7.2.2 Rotation Invariance and Aliasing. 93
7.2.3 Cortical Surface Shape Representation based on Over-complete Spherical Wavelets 94
7.3 Folding Development Study Based on Over-complete Wavelets 95
7.3.1 Experimental Setup 95

7.3.2 Cortical Folding Development Model 95
7.3.3 Overall Folding Development Study. 95
7.3.4 Regional Difference of Folding Development 98
7.4 Contributions 100

8 Conclusions **103**

Appendix: Publications of the Author

Chapter 1

Introduction

In vivo quantification of neuroanatomical shape variations is possible due to recent advances in medical imaging technology, and has proven useful in the study of neuropathology and neurodevelopment. In this chapter, we first introduce the previous work conducted in shape-based analysis of neuroanatomical structures. We state then our objectives and the major contributions of this dissertation, and give an overview of the structure of this thesis.

1.1 Motivation

Evidence suggests that morphological changes in neuroanatomical structures may reflect abnormalities in neurodevelopment, or relate to a variety of disorders, such as schizophrenia and Alzheimer's disease (AD). These morphological variations can be characterized by changes of volume, thickness, surface area and shape. With the advent and rapid development of Magnetic Resonance Imaging (MRI) techniques, it is now possible to conduct the *in vivo* analysis of neuroanatomical structures of the human being with controlled experimental designs. Therefore, it is highly desirable to develop automated tools to facilitate the morphological studies of brain structures on a large-scale with reliability and repeatability.

Efforts were originally made to characterize the volumetric and global-scale shape changes of various neuroanatomical structures, such as the cerebral cortex, hippocampus and corpus callosum. Recently, considerable effort has been focused on quantifying the localized changes in the 2-dimensional (2D) or 3-dimensional (3D) shape of brain structures. This effort is motivated by the fact that some neurological abnormalities affect only certain types of brain functions, and might cause only regional changes of neuroanatomical structures. Detecting the localized shape changes could provide new knowledge about structure-function relationships, discover the underlying biological processes related to various neurological diseases, and potentially lead to more accurate diagnoses, better treatments, and an improved understanding of neurodevelopment.

However, the difficulties in both finding an accurate shape presentation and conducting reliable statistical analysis present a challenge for the study of neuroanatomical structures. Furthermore, how to accurately and comprehensively represent the complex shape of the cerebral cortex in human beings remains one of the most interesting open questions in the field of computational anatomy, due

to the fact that the cortex is highly convoluted and greatly affected by neurodevelopment and neuropathy.

1.2 Previous Work

To accurately study shape variations of brain structures across different subjects, one would like to find not only an effective shape representation but also a registration method to preserve individual variation while aligning anatomically important structures. Different techniques employed in extracting shape features contribute to the merits and disadvantages of various shape analysis methods. In this section, we present an overview of the previous work studying the shape of neuroanatomical structures, including the cerebral cortex and subcortical brain structures such as hippocampus and ventricles. We discuss the shape representation and statistical methods, and summarize the types of statistical studies and results.

1.2.1 Shape Representation Methods

A – Understanding the complexity of cerebral cortex

The human cerebral cortex is highly convoluted, which is probably due in part to the need to increase its surface without increasing intracranial size. Quantitative measurements have been developed to characterize the geometry and folding patterns of the cortical surface.

One of the earliest and most popular measurements developed was to quantify cortical gyrification by calculating the Gyrification Index (GI), which measures the ratio of inner and outer cortical surface contours delineated on 2D coronal sections [1]. GI has been used extensively to quantify neurodevelopment and different neurological disorders such as autism, schizophrenia, and William's syndrome [2-8]. Subsequently, GI was extended to 3D by measuring a global GI across the whole cortical surface, or in a region of interest. Sulcal morphometry was also studied by assessing sulcal depth, length, width, or asymmetry index [9-11] based on the hypothesis that sulcal configuration can convey information about the early development of the cortex [12]. These methods have been used successfully to quantify the complex shape of the cortical surface, but they could not provide localized geometric information across the whole brain since they are calculated either in specifically delineated sulcal regions or on a globally scale.

Fractal Dimension (FD) was proposed by Cook *et al.* [13]and Thompson *et al.* [14] to estimate the complexity of the cortex. FD is an extremely compact measurement of shape complexity, condensing all geometrical information into a single numeric value. It has been used widely to assess normal and abnormal brain development, or quantify neurological disorders over the whole hemisphere or in lobar regions [13, 15-20] . However, it is also a global shape feature and can not be used to extract localized shape features. Furthermore, it remains a challenge to interpret the extracted geometrical information with FD measurement [21].

Recently, methods for extracting localized shape features of the cortical surface have been developed. For example, Luders *et al.* proposed an approach for estimating local gyrification index at thousands of points across the entire cortical surface by using smoothed absolute mean curvature [22]. Subsequently, Schaer *et al.* proposed to calculated the localized 3D GI in a circular region at each point on the cortical surface, which resembles the Gaussian curvature [23]. Furthermore, the automated Freesurfer tools [24] are used to calculate localized shape features of the cortical surface, which essentially measures the metric distortion at each point when the cortical surface is registered to a template using a surface-based registration method [25]. These methods can be used to quantify

localized cortical folding patterns across the whole cortical surface in an automated way. However, smoothing filters are often needed to determine the spatial extent of the shape variation when using these shape features. To achieve the best discriminative result in the subsequent statistical study, the width of filter kernel needs to be estimated empirically for each dataset under study.

B – Shape representation of subcortical structures

One of the earliest techniques developed in this field represents shapes implicitly by points sampled on the boundary of the object being studied, and the coordinates of the corresponding points on different subjects are directly used as shape features [26, 27]. Cootes *et al.* extended this method by building the point distribution model, which allows for global scale analysis of shape variation by applying Principal Component Analysis (PCA) to the positions of the boundary points [28]. This method, however, depends heavily on the accuracy of the inter-subject registration for group comparison.

Subsequently, parametric models were developed to decompose the boundary or surface using Fourier or spherical harmonic descriptors (SPHARM), and to use the decomposition coefficients as a shape descriptor [29-32]. A drawback of these models is the lack of ability to concisely represent local shape variation because of the global support of the basis functions. Recently, a weighted spherical harmonic representation has been developed and can potentially be used to conduct local analysis by differential weighting of the SPHARM coefficients [33].

Another popular method warps a template to individual subjects and studies the deformation field for shape variations [34-37]. Although this method is sensitive to the template selection and presents challenges in interpreting and comparing shape differences using the high-dimensional deformation field, a number of promising shape analysis results have been obtained and more advanced techniques based on this method have been developed.

Medial axis techniques, originally proposed by H. Blum [38] and used by Pizer *et al.* [39] and Golland *et al.* [40] in 3D and 2D, respectively, is a powerful tool for the shape analysis of a variety of subcortical structures. This technique allows for a separate study of the local position and thickness of the object at both coarse and fine levels. Another advantage of medial descriptions is due to an intrinsic coordinate system of the object, which facilitates the construction of correspondences between subjects and the subsequent statistical analysis. However, this method is sensitive to small perturbations of the boundary, which presents a challenge to the further development and application of medial representation in shape analysis.

In summary, we find that most of shape representation methods developed in the previous study can either extract global shape features at multiple spatial scales, such as methods based on SPHARM, or local shape features at a single spatial resolution, such as the measurement of local GI. However, since it is of great medical importance to study both the location and spatial extent of shape changes, it's highly desirable to extract local and multi-scale features, especially for the convoluted cortical surfaces.

1.2.2 Statistical Analysis and Applications

Using various shape representation models, shape features are extracted from the surfaces to study the relationships of these shape features with a set of explanatory variables, or examine the differences of these shape features between groups. Linear models, such as Analysis of Variance (ANOVA), multiple linear regression and General Linear Model (GLM), have been used to study

the effects of aging, gender, genetics, or drug treatments on the shape of neuroanatomical structures [21, 41, 42].

A variety of discriminative modeling techniques have been employed to select shape features that best separate the brain structures of two groups. Some use typical group mean statistics, such as *t* statistics, to study the shape differences between patients and normal controls by directly comparing the group averages [41, 43-47], while others employ more advanced feature selection tools based on vector feature input [48]. Non-parametric methods, such as permutation testing, have been proposed to correct for multiple comparisons in shape feature selection, which has been a great concern in shape analysis, as the large number of features, and therefore the large number of statistical tests involved, increases the chance of false detection [43]. Furthermore, classification methods such as the Linear Discriminate Analysis (LDA) and the Support Vector Machines (SVMs) have been used to detect the differences between classes, and construct classifiers from the training set to automatically assign new subjects to discriminative groups [49-51].

Recruiting more powerful statistical analysis techniques is crucial for the discrimination and understanding of differences between normal controls and diseased patients, as well as the correlation of shape features with various other potentially influential factors.

1.2.3 Shape Analysis Results

Statistical analysis methods have been applied to study aging [11, 41, 52], gender [22], and disease [23, 25, 53, 54] related shape changes of the cerebral cortex, as well as a number of subcortical brain structures. Various studies have demonstrated that shape measures reveal new information beyond what is obtained through volume measurements, which has improved our understanding of structural variances in normal populations and differences between healthy controls and patients. In this subsection, we introduce and compare results obtained from two of the most common types of shape-based studies of sub-cortical structures: the study of hippocampus shape changes related to schizophrenia and the study of lateral ventricle in twins.

A – Shape changes of the hippocampus related to schizophrenia

The goal of this type of study is to assess shape asymmetry between the left and right hippocampi, and also to analyze shape deformation in schizophrenic patients. Most groups found that the analysis of hippocampal shape can discriminate between schizophrenic and control subjects with greater power than volumetry [31, 47, 55]. Styner *et al.* and Shenton *et al.* found that the differences between patients and controls are located mostly in the tail [46, 56, 57]. However, Csernanasky *et al.* reported hippocampal abnormalities in schizophrenia located mainly in the head region [45, 47, 55]. The discrepancy may be due to the different methodologies or groups of subjects, but there is no clear explanation to date.

B – Lateral ventricle twin study

This type of study investigates the group differences of the lateral ventricles between Monozygotic (MZ) twins, Dizygotic (DZ) twins and Unrelated (NR) subjects. The goal of this study is to determine whether MZ twins have more similarly shaped lateral ventricles than DZ twins or NR subject pairs.

Without exceptions, twin studies have demonstrated that significant differences between MZ and DZ pairs could not be found by volume measurements but were revealed by shape analysis [39, 43, 58]. However, Styner *et al.* [31] found there was a significant group difference between MZ and DZ twin pairs for the right but not for the left ventricles.

In summary, a variety of shape analysis has been conducted in the previous work to quantify the shape changes of the cortex and sub-cortical structures. However, there is a lack of shape analysis on cortical surfaces using more advanced statistical analysis methods, such as classification, compared with the sub-cortical shape analysis.

1.3 Objective and Contributions

In order to accurately and efficiently extract multi-scale and localized shape features, we propose to represent the shape using a spherical wavelet transformation. Using the resulting wavelet coefficients as shape features, we develop a set of statistical analysis frameworks to study the localization and spatial extent of shape changes of neuroanatomical structures associated with idiosyncratic difference, neurological diseases and neurodevelopment. We also develop a method to improve the segmentation accuracy of sub-cortical structures by incorporating multi-scale shape information extracted using this wavelet-based shape representation. Our contributions can be broadly divided into three categories.

A – Multi-scale and localized shape representation of neuroanatomical structures

In this dissertation, we propose to decompose the surface of neuroanatomical structures using a spherical wavelet transformation, and to use the wavelet coefficients as shape features. These shape features represent the surface at multiple spatial scales and locations, as the underlying wavelet basis functions have local support in both space and frequency. This multi-scale and localized shape representation allows us to study the surface at different spatial resolutions, in contrast to the curvature-based shape features, and in a localized fashion, in contrast to global shape representations. We first develop a method to extract normalized shape features for a set of registered subjects based on a bi-orthogonal spherical wavelet transformation [59], which is easy to compute and has good compression properties. We then improve upon this proposed shape representation by adopting a newly developed over-complete wavelet transformation [60] and demonstrate its use in improving the accuracy and stability of shape representations. Our approach provides a novel way to study the shape of neuroanatomical structures, particularly the convoluted cortical surfaces, in a multi-resolution and localized fashion. Furthermore, we can easily visualize and interpret the shape information represented by each spherical wavelet coefficient by using the inverse wavelet transformation. The visualization property is of great use in the medical image analysis.

B – Statistical Shape analysis

We develop a set of statistical analysis frameworks based on our new shape representation, and apply them to study the convoluted folding of cortical surfaces. First, we develop a method to visualize the most distinct patterns of cortical folding variations in a population at multiple resolutions by using principal component analysis (PCA) in the wavelet domain. We apply this method to study cortical folding variations in an elderly normal population and visualize the shape variations in this dataset. These results can be used as a baseline for discriminative studies of

neurological diseases. Furthermore, we investigate the correlation of these cortical folding variations with age, gender and a set of neuropsychological scores and find that large-scale cortical folding variations are significantly related with age in the female group.

We then develop a new classification framework to detect the discriminative cortical folding differences in two groups using the wavelet-based shape representation. We employ a Bayesian classification method, predictive automatic relevance determination (pred-ARD), for feature selection and classification, and demonstrate that it outperforms the classical method such as SVMs in our cortical shape-based group comparison study. We also demonstrate promising classification results in the study of mild dementia. The developed framework provides a power tool for detecting shape changes related to neurological disease, and can be used for computer-aided diagnosis in the future.

Thirdly, we develop a nonlinear temporal model for studying the cortical folding development at coarse and progressively finer spatial resolutions in neurodevelopment based on the wavelet transformation. We develop a regularization framework to improve prediction performance on new MRI scans given the limited amount of training data and employ an efficient model estimation method. Using a dataset of newborn, we develop multi-scale folding models in late gestation and provide novel findings of the temporal order and regional differences in cortical folding development. These normal development models can be potentially used for the early detection of neurological defects.

C – Shape-guided segmentation

Finally, we develop a method to improve the segmentation of sub-cortical structures, such as the hippocampus, by incorporating multi-scale shape information in the wavelet domain obtained from a training set. By using image models that incorporate probabilistic information about label and intensity, we deform the surface to the boundary of the object guided by, but not limited to the shape priors obtained from the training set. We demonstrate that the proposed method improves the segmentation accuracy of the hippocampus in spite of the imperfections of MR images.

The methods developed in this dissertation, including spherical wavelet transformation, a set of statistical analysis procedures, and the shape-guided sub-cortical segmentation, are implemented as part of the Freesurfer [24], which is a publicly available software package for conducting a variety of MR image analyses. Together with the MR image preprocessing tools in the Freesurfer, this entire procedure can be used to conduct automated shape analysis on neuroanatomical structures of large sets of MR images.

1.4 Thesis Overview

This thesis is organized in three parts. The first part, corresponding to Chapter 2, presents our approach of using spherical wavelet transformation to extract shape features of neuroanatomical structures. We describe the developed procedures for obtaining normalized bi-orthogonal spherical wavelet coefficients for a set of registered subjects and demonstrate the superior ability of the wavelet-based shape representation in characterizing localized shape variation compared with SPHARM.

The second part, consisting of Chapters 3, 4, 5 and 6, presents our contributions to conducting statistical analysis based on the wavelet representation, and to using the shape information to

improve the accuracy of sub-cortical structure segmentation.

In Chapter 3, we build shape models at multiple resolutions by applying PCA in the spherical wavelet domain and demonstrate the use of this method in characterizing the most distinct patterns of cortical folding variations in a nondemented elderly population. Furthermore, we investigate the correlations of these observed cortical folding variations with age, gender and a set of neuropsychological measurements. In addition, we show the use of the proposed method in studying the cortical folding development in a small dataset of newborn.

In Chapter 4, we develop a classification framework to study cortical folding differences between two groups of subjects using the shape features extracted from spherical wavelet transformation. We employ a Bayesian classification method to train a classifier and select features by minimizing an estimate of prediction error. We introduce the entire framework including preprocessing, feature selection, classification and visualization of the cortical shape differences, which correspond to these selected features at multiple spatial scales and different locations. We demonstrate that the Bayesian classification method achieves better classification accuracy compared with a classical method in our shape-based patient/control study, and present potentially interesting biological results on real datasets.

In Chapter 5, we develop a nonlinear temporal model of cortical folding development at multiple spatial scales using the wavelet-based shape representation. We introduce in detail the model estimation method. We show the new findings regarding the temporal order of cortical folds of large and progressively smaller spatial scales and the regional differentiation in folding development by estimating these models on a MRI dataset of newborn.

Finally, in Chapter 6, we develop a method to improve the segmentation accuracy of sub-cortical structures by incorporating statistical shape information extracted from a training dataset with the spherical wavelet transformation. We introduce in detail the developed surface deformation method using image-based models with multi-scale shape constraints, and demonstrate the use of the proposed method in improving the segmentation of the hippocampus in a manually segmented MRI dataset.

In the third part of this thesis, which consists of Chapter 7, we develop a method to extract shape features using a newly developed over-complete spherical wavelet transformation. We demonstrate the theoretical advantage of over-complete wavelets over bi-orthogonal wavelets in terms of providing more accurate localization of shape changes. Lastly, we illustrate the power of over-complete wavelets in building more stable cortical folding development models, and detecting a wider array of regions of folding development in the dataset of newborn compared to the results in Chapter 5.

We conclude the thesis in Chapter 8. At the end of each chapter, we review the main contributions and indicate the associated publications. The bibliography and appendix are made for each chapter separately. The appendix at the end of this thesis lists all of our publications related to this work.

Bibliography

[1] K. Zilles, E. Armstrong, A. Schleicher, and H.-J. Kretschmann, "The human pattern of gyrification in the cerebral cortex," Anat. Embryology, vol. 179, pp. 173-179, 1988.

[2] J. J. Kulynych, L. F. Luevano, D. W. Jones, and D. R. Weinberger, "Cortical abnormality in schizophrenia: an in vivo application of the gyrification index," Biol Psychiatry, vol. 41, pp. 995-999, 1997.

[3] K. Vogeley, T. Schneider-Axmann, U. Pfeiffer, R. Tepest, T. A. Bayer, B. Bogerts, W. G. Honer, and P. Falkai, "Disturbed gyrification of the prefrontal region in male schizophrenic patients: A morphometric postmortem study," Am J Psychiatry, vol. 157, pp. 34-39, 2000.

[4] K. Vogeley, R. Tepest, U. Pfeiffer, T. Schneider-Axmann, W. Maier, W. G. Honer, and P. Falkai, "Right frontal hypergyria differentiation in affected and unaffected siblings from families multiply affected with schizophrenia: A morphometric mri study," Am J Psychiatry, vol. 158, pp. 494-496, 2001.

[5] S. R. Kesler, B. Vohr, K. C. Schneider, K. H. Katz, R. W. Makuch, A. L. Reiss, and L. R. Ment, "Increased temporal lobe gyrification in preterm children," Neuropsychologia, vol. 44, pp. 445-453, 2006.

[6] J. E. Schmitt, K. Watts, S. Eliez, U. Bellugi, A. M. Galaburda, and A. L. Reiss, "Increased gyrification in Williams syndrome: Evidence using 3D MRI methods," Dev Med Child Neurol, vol. 44, pp. 292-295, 2002.

[7] A. Y. Hardan, R. J. Jou, M. S. Keshavan, R. Varma, and N. J. Minshew, "Increased frontal cortical folding in autism: a preliminary MRI study," Psychiatry Res, vol. 131, pp. 263-268, 2004.

[8] J. M. Harris, H. Whalley, S. Yates, P. Miller, E. C. Johnstone, and S. M. Lawrie, "Abnormal cortical folding in high-risk individuals: A predictor of the development of schizophrenia," Biol Psychiatry, vol. 56, pp. 182-189, 2004.

[9] N. Molko, A. Cachia, D. Riviere, J. F. Mangin, M. Bruandet, D. Le Bihan, L. Cohen, and S. Dehaene, "Functional and structural alterations of the intraparietal sulcus in a developmental dyscalculia of genetic origin," Neuron, vol. 40, pp. 847-58, 2003.

[10] J. F. Mangin, D. Riviere, A. Cachia, E. Duchesnay, Y. Cointepas, D. Papadopoulos-Orfanos, P. Scifo, T. Ochiai, F. Brunelle, and J. Regis, "A framework to study the cortical folding patterns," Neuroimage, vol. 23, pp. 129-138, 2004.

[11] P. Kochunov, J. F. Mangin, T. Coyle, J. Lancaster, P. Thompson, D. Riviere, Y. Cointepas, J. Regis, A. Schlosser, D. R. Royall, K. Zilles, J. Mazziotta, A. Toga, and P. T. Fox, "Age-related morphology trends of cortical sulci," Hum Brain Mapp, vol. 26, pp. 210-220, 2005.

[12] J. Regis, J. F. Mangin, T. Ochiai, V. Frouin, D. Riviere, A. Cachia, M. Tamura, and Y. Samson, ""Sulcal root" generic model: a hypothesis to overcome the variability of the human cortex folding patterns," Neurol Med Chir, vol. 45, pp. 1-17, 2005.

[13] M. J. Cook, S. L. Free, M. R. Manford, D. R. Fish, S. D. Shorvon, and J. M. Stevens, "Fractal description of cerebral cortical patterns in frontal lobe epilepsy," Eur Neurol, vol. 35, pp. 327-335, 1995.

[14] P. M. Thompson, C. Schwartz, R. T. Lin, A. A. Khan, and A. W. Toga, "Three-dimensional statistical analysis of sulcal variability in the human brain.," Journal of Neuroscience, vol. 16, pp. 4261-4274, 1996.

[15] R. E. Blanton, J. G. Levitt, P. M. Thompson, K. L. Narr, L. Capetillo-Cunliffe, A. Nobel, J. D. Singerman, J. T. McCracken, and A. W. Toga, "Mapping cortical asymmetry and complexity patterns in normal children," Psychiatry Research: Neuroimaging, vol. 107, pp. 29-43, 2001.

[16] K. L. Narr, R. M. Bilder, S. Kim, P. M. Thompson, P. Szeszko, D. Robinson, E. Luders, and A. W. Toga, "Abnormal gyral complexity in first-episode schizophrenia," Biol Psychiatry, vol. 55, pp. 859-867, 2004.

[17] J. M. Lee, U. Yoon, J. J. Kim, I. Y. Kim, D. S. Lee, J. S. Kwon, and S. I. Kim, "Analysis of the hemispheric asymmetry using fractal dimension of a skeletonized cerebral surface," IEEE Trans Biomed Eng,, vol. 51, pp. 1494-1498, 2004.

[18] E. Luders, K. L. Narr, P. M. Thompson, D. E. Rex, L. Jancke, H. Steinmetz, and A. W. Toga, "Gender differences in cortical complexity," Nat Neurosci, vol. 7, pp. 799-800, 2004.

[19] T. H. Ha, U. Yoon, K. J. Lee, Y. W. Shin, J. M. Lee, I. Y. Kim, K. S. Ha, S. I. Kim, and J. S. Kwon, "Fractal dimension of cerebral cortical surface in schizophrenia and obsessive-compulsive disorder," Neurosci Lett, vol. 384, pp. 172-176, 2005.

[20] L. Zhang, J. Z. Liu, D. Dean, V. Sahgal, and G. H. Yue, "A three-dimensional fractal analysis method for quantifying white matter structure in human brain," J Neurosci Methods, vol. 150, pp. 242-253, 2006.

[21] K. Im, J. M. Lee, U. Yoon, Y. W. Shin, S. B. Hong, I. Y. Kim, J. S. Kwon, and S. I. Kim, "Fractal dimension in human cortical surface: Multiple regression analysis with cortical thickness, sulcal depth, and folding area," Hum Brain Mapp, vol. 27, pp. 994-1003, 2006.

[22] E. Luders, P. M. Thompson, K. L. Narr, A. W. Toga, L. Jancke, and C. Gaser, "A curvature-based approach to estimate local gyrification on the cortical surface," Neuroimage, vol. 29, pp. 1224-1230, 2006.

[23] M. Schaer, M. Bach Cuadra, L. Tamarit, F. Lazeyras, S. Eliez, and J.-P. Thiran, "A Surface-based approach to Quantify Local Cortical Gyrification," IEEE Trans on Med Imaging, 2007.

[24] "http://surfer.nmr.mgh.harvard.edu."

[25] J. J. Wisco, G. Kuperberg, D. Manoach, B. T. Quinn, E. Busa, B. Fischl, S. Heckers, and A. G. Sorensen, "Title: Abnormal cortical folding patterns within Broca's area in schizophrenia: Evidence from Structural MRI," Schizophr Res., vol. 94, pp. 317-327, 2007.

[26] I. Dryden and K. Mardia, "Multivariate shape analysis," Sankhya, vol. 55, pp. 460-480, 1993.

[27] F. L. Bookstein, "Morphometric Tools for Landmark Data: Geometry and Biology," 1991.

[28] T. Cootes, C. Taylor, D. Cooper, and J. Graham, "Active shape models - their training and application," Computer Vision and Image Understanding, vol. 61, pp. 38-59, 1995.

[29] C. Brechbuhler, G. Gerig, and O. Kubler, "Parametrization of Closed Surfaces for 3-D Shape Description," Computer Vision and Image Understanding, vol. 61, pp. 154-170, 1995.

[30] A. Kelemen, G. Szekely, and G. Gerig, "Elastic model-based segmentation of 3d neuroradiological data sets," IEEE Transactions on Medical Imaging, vol. 18, pp. 828-839, 1999.

[31] M. Styner, G. Gerig, J. Lieberman, D. Jones, and D. Weinberger, "Statistical shape analysis of neuroanatomical structures based on medial models," Medical Image Analysis, vol. 7, pp. 207-220, 2003.

[32] L. Shen, J. Ford, F. Makedon, and A. Saykin, "hippocampal shape analysis surface-based representation and classification," SPIE Medical Imaging, 2003.

[33] M. K. Chung, S. Wang, K. M. Dalton, R. J. Davidson, S. Robbins, and A. C. Evans, "Tensor-based Cortical Morphometry via Weighted Spherical Harmonic Representation," MMBIA, 2006.

[34] G. Christensen, R. Rabbitt, and M. Miller, "3d brain mapping using a deformable neuroanatomy," Physics in Medicine and Biology, vol. 39, pp. 609-618, 1994.

[35] C. Davatzikos, M. Vaillant, S. Resnick, J. Prince, S. Letovsky, and R. Bryan, "A computerized method for morphological analysis of the corpus callosum," Journal of Computer Assisted Tomography, vol. 20, pp. 88-97, 1996.

[36] S. C. Joshi, M. I. Miller, and U. Grenander, in press., "On the geometry and shape of brain sub-manifolds.," Processing of MR images of the human brain. International Journal of Pattern Recognition and Artificial Intelligence, Special Issue, 1997.

[37] P. Thompson, J. Giedd, R. Woods, D. MacDonald, A. Evans, and A. Toga, "Growth patterns in the developing brain detected by using continuum machanical tensor maps," Nature, pp. 190-193, 2000.

[38] T. Blum, "A transformation for extracting new descriptors of shape," Models for the Perception of Speech and Visual Form, 1967.

[39] S. Pizer, D. Fritsch, P. Yushkevich, V. Johnson, and E. Chaney, "Segmentation, registration, and measurement of shape variation via image object shape," IEEE Transactions on Medical Imaging, vol. 18, pp. 851-865, 1999.

[40] P. Golland, W. Grimson, and R. Kikinis, "Statistical shape analysis using fixed topology skeletons: Corpus callosum study," nformation Processing in Medical Imaging, pp. 382-388, 1999.

[41] V. A. Magnotta, N. C. Andreasen, S. K. Schultz, G. Harris, T. Cizadlo, D. Heckel, P. Nopoulos, and M. Flaum, "Quantitative in vivo measurement of gyrification in the human brain: changes associated with aging," Cerebral Cortex, vol. 9, pp. 151-160, 1999.

[42] G. Gerig, K. E. Muller, E. O. Kistner, Y.-Y. Chi, M. Chakos, M. Styner, and J. A. Lieberman, "Age and treatment related local hippocampal changes in schizophrenia explained by a novel shape analysis method," Proc. Medical Image Computing and Computer-Assisted Intervention, pp. 653-660, 2003.

[43] G. Gerig, M. Styner, D. Jones, D. Weinberger, and J. Lieberman, "Shape analysis of brain ventricles using spharm," Mathematical Methods in Biomedical Image Analysis, pp. 171-178, 2001.

[44] J. Martin, A. Pentland, and R. Kikinis, "Shape Analysis of Brain Structures Using Physical and Experimental Models," Proc. CVPR'94, pp. 752-755, 1994.

[45] J. G. Csernansky, L. Wang, D. Rastogi-Cruz, J. Posener, N. Brickel, G. Heydebrand, J. Philip Miller, and M. I. Miller, "Hippocampal deformities in schizophrenia characterized by high dimensional brain mapping," The American Journal of Psychiatry, vol. 159, pp. 1-7, 2002.

[46] S. M. Pizer, T. Fletcher, A. Thall, M. Styner, G. Gerig, and S. Joshi, "Object Models in Multiscale Intrinsic Coordinates via M-reps," mage and vision computing, vol. 21, pp. 5-15, 2002.

[47] L. Wang, S. C. Joshi, M. I. Miller, and J. G. Csernansky, "Statistical analysis of hippocampal asymmetry in schizophrenia.," NeuroImage, vol. 14, pp. 531-545, 2001.

[48] P. Golland, B. Fischl, M. Spiridon, N. Kanwisher, R. L. Buckner, M. E. Shenton, R. Kikinis, A. M. Dale, and W. E. L. Grimson, "Discriminative analysis for image-based studies," MICCAI, vol. 1, pp. 508-515, 2002.

[49] J. G. Csernansky, S. Joshi, L. Wang, J. W. Haller, M. Gado, J. P. Miller, U. Grenander, and M. Miller, "Hippocampal morphometry in schizophrenia by high dimensional brain mapping," Proc. Nat. Acad. of Science, vol. 95, pp. 11406-11411, 1998.

[50] A. Kelemen, G. Szekely, and Gerig G., "Three-dimensional Model-Based Segmentation," Proc. IEEE Intl. Workshop on Model Based 3D Image Analysis, Bombay, India, pp. 87-96, 1998.

[51] P. Yushkevich, S. Joshi, and S. Pizer, "Feature selection for shape-based classification of biological objects," Technical Report, University of Norht carolina, Chapel Hill, NC, USA,, 2002.

[52] M. E. Rettmann, M. A. Kraut, J. L. Prince, and S. M. Resnick, "Cross-sectional and longitudinal analyses of anatomical sulcal changes associated with aging," Cerebral Cortex, vol. 16, pp. 1584-1594, 2006.

[53] J. J. Kulynych, L. F. Luevano, D. W. Jones, and D. R. Weinberger, "Cortical abnormality in schizophrenia: An in vivo application of the gyrification index," Biological Psychiatry, vol. 41, pp. 995-999, 1997.

[54] R. Jou, A. Hardan, and M. Keshavan, "Reduced cortical folding in individuals at high risk for schizophrenia: a pilot study.," Schizophrenia Research, vol. 75, pp. 309-313, 2005.

[55] J. W. Haller, G. E. Christensen, S. Joshi, J. W. Newcomer, M. I. Miller, J. C. Csernansky, and M. W. Vannier, "Hippocampal mr imaging morphometry by means of general pattern matching," Radiology, vol. 199, pp. 787-791, 1996.

[56] M. E. Shenton, G. Gerig, R. W. McCarley, G. Szekely, and R. Kikinis, "Amygdala-hippocampal shape differences in schizophrenia: the application of 3D shape models to volumetric MR data," Psychiatry Research: Neuroimaging, vol. 115, pp. 15-35, 2002.

[57] M. Styner, J. Lieberman, and G. Gerig, "Boundary and Medial Shape Analysis of the Hippocampus in Schizophrenia," MICCAI 2003 Conference, 2003.

[58] G. Gerig, M. Styner, and J. Lieberman, "Shape versus Size: Improved understanding of the morphology of brain structures," Proc. MICCAI 2001, pp. 24-32, 2001.

[59] P. Schroder and W. Sweldens, "Spherical Wavelets: Texture Processing," in Rendering Techniques, 1995, pp. 252-263.

[60] B. T. T. Yeo, W. Ou, and P. Golland, "On the construction of invertible filterbank on the 2-sphere," Technical Report, http://people.csail.mit.edu/ythomas/IFB2006.pdf, 2006.

Chapter 2

Shape Representation Based on Bi-orthogonal Spherical Wavelets

In this chapter, we propose the use of a spherical wavelet transformation to extract shape features of neuroanatomical structures, such as cortical surfaces reconstructed from magnetic resonance (MR) images. The shape representation based on the spherical wavelet transformation can characterize the underlying surface locally in both space and frequency, in contrast to spherical harmonics (SPHARM) that have a global basis set. In this chapter, we develop a set of procedures for exacting the normalized bi-orthogonal spherical wavelet coefficients for a set of registered surfaces reconstructed. We introduce the preprocessing procedure employed to obtain and register cortical surfaces based on MR images, and our pipeline for conducting statistical analysis using this wavelet-based shape representation. We also demonstrate the ability of spherical wavelet-based shape representation to better capture localized shape variation compared with SPHARM

2.1 Motivation

For the purpose of quantitatively studying the shape of neuroanatomical structures, such as the cerebral cortex and the hippocampus, a variety of shape descriptors has been developed to extract shape features of the underlying object, as introduced in Chapter 1. Among them, parametric model was first developed to decompose the boundary, represented with a set of boundary points, using Fourier descriptors [1, 2]. Later on, this work was extended to extract multi-scale shape features of an object with spherical topology, usually represented by a surface mesh, using Spherical Harmonic descriptors (SPHARM) [3]. These methods essentially transform the underlying surface function into multiple spatial frequency bands. Therefore, by using the decomposition coefficients as shape features, we can hierarchically describe large-scale and progressively smaller scale shape properties. However, a drawback of these models is the lack of ability to concisely represent local shape variation because of the global support of the basis functions.

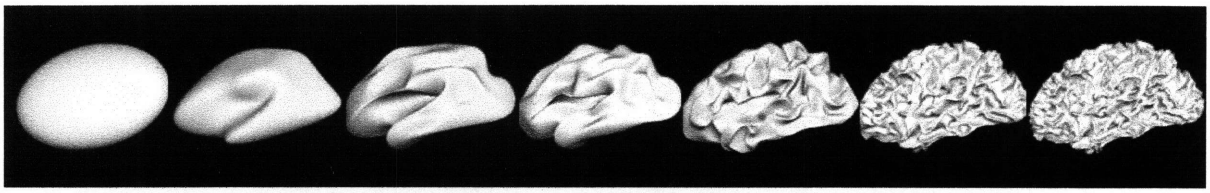

Figure 2-1: Reconstructed cortical surfaces using SPHARM coefficients truncated at degree 1, 2, 5, 10, 20, 40 and the original surface (from left to right). This figure demonstrates SPHARM's effectiveness for multi-resoluational representation of cortical surfaces. Note that by using a higher degree, one can always represent the surface more accurately. However, since SPHARM bases are global, SPHARM coefficients cannot represent local shape features concisely.

2.1.1 Limitation of Spherical Harmonic Descriptors in Shape Representation

Since the boundaries of many neuroanatomical structures have spherical topology, various methods have been developed to map their surfaces to a sphere while preserving the metric properties of the original surface. These surface mapping procedures make SPHARM, a natural extension of Fourier transformation on the sphere, a very popular tool for extracting multi-scale shape features.

The spherical harmonic basis functions Y_l^m of degree l and order m, $-l \le m \le l$ are defined on $\theta \in [0;\pi], \phi \in [0;2\pi)$ as:

$$Y_l^m(\theta,\phi) = \sqrt{\frac{2l+1}{4\pi}\frac{(l-m)!}{(l+m)!}} P_l^m(\cos\theta) e^{im\phi}, \qquad (2.1)$$
$$Y_l^{-m}(\theta,\phi) = (-1)^m Y_l^{m*}(\theta,\phi),$$

where $Y_l^{m*}(\theta,\phi)$ denotes the complex conjugate of $Y_l^m(\theta,\phi)$ and P_l^m denotes the associated Legendre polynomials

$$P_l^m(\omega) = \frac{(-1)^m}{2^l l!}(1-\omega^2)^{\frac{m}{2}} \frac{d^{m+l}}{d\omega^{m+l}}(\omega^2-1)^l. \qquad (2.2)$$

Brechbühler *et al.* fist introuduced the use of spherical harmonics to the analysis of neuroanatomical structures [3]. They proposed the idea that any surface mapped onto a sphere $\mathbf{v}(\theta,\varphi) = \{x(\theta,\varphi), y(\theta,\varphi), z(\theta,\varphi)\}^T$ can be expressed as the weighted summation of a set of spherical harmonics basis function:

$$\mathbf{v}(\theta,\varphi) = \sum_{l=0}^{\infty}\sum_{m=-l}^{l} c_l^m Y_l^m(\theta,\varphi) \quad , \qquad (2.3)$$

where the coefficient $\mathbf{c}_l^m = \left[\mathbf{c}_l^{m^x}, \mathbf{c}_l^{m^y}, \mathbf{c}_l^{m^z}\right]^T$ is a three-dimensional vector corresponding to the three spatial coordinates. We can obtain object shape representations at different levels of detail by truncating the spherical harmonic series at different degrees, as shown in Figure 2-1.

The coefficients c_l^m can be calculated by solving a least-squares problem [4]. For example, we gather the values of the basis functions in the matrix $\mathbf{z} = (\mathbf{z}_{n,j(l,m)})$ with $\mathbf{z}_{n,j(l,m)} = Y_l^m(\theta_n,\varphi_n)$, where $j(l,m)$ is a function assigning an index to every pair (l, m) and n denotes the indices of the N surface points. And we denote $\mathbf{v} = \left[\mathbf{v}_1, \mathbf{v}_2, \cdots, \mathbf{v}_N\right]^T$ as the $N \times 3$ position matrix of all the N points on the surface. Then the coefficient matrix $\mathbf{c} = (\mathbf{c}_0^0, \mathbf{c}_1^{-1}, \mathbf{c}_1^0, \cdots)^T$ that best approximate the points in a least-squares sense could be obtained by

$$\mathbf{c} = (\mathbf{z}^{\mathrm{T}}\mathbf{z})^{-1}\mathbf{z}^{\mathrm{T}}\mathbf{v} \ . \qquad (2.4)$$

By selecting an appropriate degree for the surface under study, the calculated coefficients can be used to represent the surface at different spatial resolution with sufficiently small approximation error. This shape representation has been used to conduct statistical analysis of the shape changes of brain structures such as the hippocampus and the lateral ventricles [5-7]. However, SPHARM coefficients cannot concisely indicate the location of shape differences because of the global support of the basis functions. Most recently, a weighted SPHARM technique has been developed and applied to cortical thickness analysis and voxel-based morphometry. This technique provides a new framework for weighting the SPHARM coefficients differently and can be potentially used to improve the localization property of SPHARM representation [8].

2.1.2 Our Methods

In order to represent the surface locally in both space and frequency, we develop a procedure to characterize the surface of neuroanatomical structures using spherical wavelets. The computed wavelet coefficients are used as shape features to study the folding pattern of cortical surfaces at different spatial scales and locations, as the underlying wavelet basis functions have local support in both space and frequency.

In this work, we first employ bi-orthogonal spherical wavelets developed by Schröder and Swelden [9] and conduct a variety of statistical analyses to study the shape of cortical surfaces, and build shape models to guide the segmentation of sub-cortical structures, such as the hippocampus, based on this wavelets transformation [10]. We then improve upon this wavelet-based shape representation by employing a newly developed over-complete wavelets [11], which will be introduced in Chapter 7.

To obtain the surface mesh of neuroanatomical structures based on MR images and register the surfaces across different subjects, we need to go through a set of preprocessing steps. In the following section, we first introduce the processing steps, and the automated pipeline we build to conduct the automated wavelet-based shape analysis of brain structures using MR images. We then introduce in detail the procedure of extracting shape features using bi-orthogonal spherical wavelet transformation. Lastly, we demonstrate the use of this wavelet-based shape representation in detecting shape variation, and compare it with SPHARM.

2.2 Preprocessing

In this section, we introduce the procedure used to reconstruct and refine the surface of neuroanatomical structures and conduct surface-based registration. Given a raw 3D MR image, we first segment out the structure of interest and reconstruct its surface. We then map the surface onto a parameterized sphere in order to transform this surface using basis functions defined in a spherical coordinate system, such as SPHARM and spherical wavelets. Then, we use a surface-based registration procedure to establish correspondence across subjects in order to carry out the statistical analysis based on the spherical transformation of the surfaces.

In this work, we use a set of automated tools distributed as part of the Freesurfer package [12] to preprocess the MR images, which includes surface reconstruction, spherical transformation, and registration in the spherical coordinate system, as shown in Figure 2-2. Together with the MR image preprocessing tools in the Freesurfer, this entire procedure can be used to conduct automated shape analysis on neuroanatomical structures of large sets of MR images. In this thesis, we present the application results of developed shape analysis tools on the cortex and the hippocampus. As an

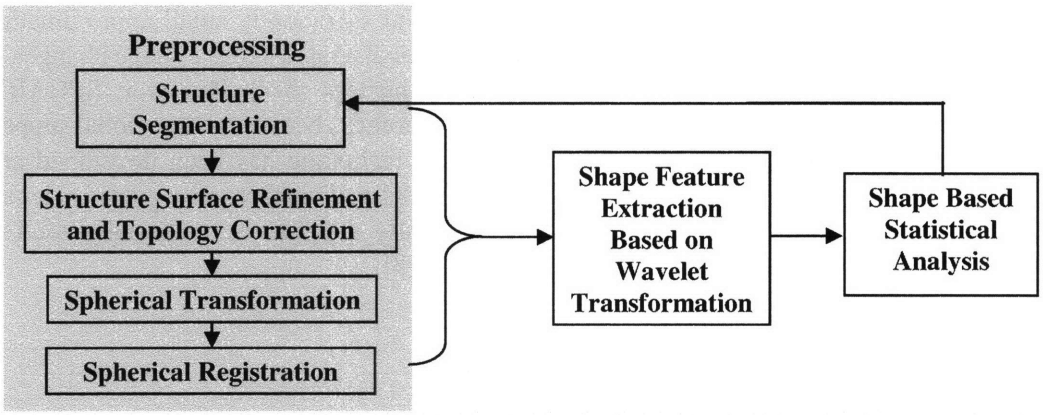

Figure 2-2: The automated procedure for conducting the shape analysis of neuroanatomical structures based on MRI.

example, we describe in this chapter the pipeline used to preprocess cortical surfaces based on MR images. In Chapter 6, we introduce the preprocessing procedure for subcortical structures, which uses the same pipeline with a slight change of processing parameters.

To reconstruct the cortical surfaces, which include the gray/white matter boundaries (hereafter referred to as white matter surfaces) and gray-matter/cerebrospinal fluid boundaries (CSF) boundaries (hereafter referred to as pial surfaces) of the left and right hemispheres, the MR images are first registered to a pre-built template in the Talairach space. The image intensity is normalized to remove spatial variations induced by inhomogeneities in the RF field, and used to guide skull stripping and white matter labeling. This white matter segmentation is further refined and cut to generate a single connected mass of each hemisphere. A surface tessellation is then constructed for each white matter volume by representing each square face separating the white matter voxels from other classes with two triangles as detailed in [13]. Topological defects are automatically detected and corrected for this tessellation to guarantee spherical topology. After that, we deform the surface in the normalized image volume under smoothness and boundary intensity constraints to generate a more accurate and smoother hemisphere. Finally, the resulting white matter surface is deformed outwards to the location in the volume that has the largest intensity contrast between the gray matter and CSF, and refined to generate the pial surface.

Next, the reconstructed white matter surface is mapped onto a sphere in two steps. First, the white matter surface is inflated and projected radially to a sphere. Then, the large folds and metric distortion introduced by the projection process are removed by the minimization of folded area and the preservation of the local and long range distances between vertices [14]. Surfaces of different subjects are then registered in the spherical coordinate system by minimizing an energy functional that is a combination of a topology preserving term, a folding alignment term and a metric preservation term. The alignment of gyral and sucal patterns enables us to find anatomically corresponding points on the reconstructed cortical surfaces across subjects, and the metric preservation term (including area and distance) allows us to preserve individual variations. The effectiveness of this spherical registration technique in finding correspondence across subjects is proven in [15].

Although the entire procedure can be used to analyze both the gray/white matter boundary and gray-matter/CSF, only the gray/white surface, which is a direct reflection of the gyral folding, is used in this work to exemplify the developed methods.

2.3 Shape Representation Based on Spherical Wavelets

The Euclidean wavelet transform is a powerful tool in image processing that represents a signal with component signals of different scales and spatial locations. It has been widely applied to compression, de-noising, and medical image analysis [16-18]. In the past decade, there has been extensive research focused on extending the general paradigm of linear filtering to the spherical domain. These newly developed spherical wavelets have been used for shape representation with a wide range of applications to computer graphics [19-25]. However, the use of this technique in multiresolution shape analysis of medical images, including CT and Magnetic Resonance Imaging (MRI), was not explored until recently. Greenshields *et al.* [26] was one of the first to use spherical wavelets decomposition to analyze the shape of pelvis based on computational tomography (CT) images in 2001. More recently, we develop a procedure for conducting wavelet-based shape analysis of neuroanatomical structures based on MRI [27]. A parallel study was conducted by Nain *et. al.* to learn a shape prior of anatomical structures (such as prostate and caudate nucleus) by using bi-orthogonal spherical wavelet transformation [28], and to use this prior for image segmentation based on the wavelets presentation [29].

2.3.1 Bi-orthogonal Spherical Wavelets

Broadly speaking, a wavelet representation of a function consists of a coarse overall approximation together with detail coefficients that influence the function at various spatial scales and locations. The classical form of wavelet analysis transforms signals by projecting them onto a set of basis functions, called wavelets, in which every wavelet is a scaled and translated copy of a single unique function, called the mother wavelet. The bi-orthogonal spherical wavelets employed in this chapter belong to the *second generation wavelets*, which maintain the notion that a basis function can be expressed as a linear combination of basis functions at a finer, more subdivided level.

A – Wavelet function construction

The construction of these bi-orthogonal spherical wavelets relies on a recursive subdivision of an icosahedron (subdivision level 0) (cf. [9]). Denoting the set of all vertices on the mesh before the j^{th} subdivision as $K(j)$, a set of new vertices $M(j)$ can be obtained by adding vertices at the midpoint of edges and connecting them with geodesics. Therefore, the complete set of vertices at the $(j+1)^{th}$ level is given by $K(j+1) = K(j) \bigcup M(j)$. As a result, the number of vertices at level j is $10 \times 4^j + 2$, e.g., 12 vertices at level 0, 42 at level 1, 162 at level 2, and etc.

Next, an interpolating subdivision scheme is used to construct the scaling functions $\varphi_{j,k}$ defined at level j and node $k \in K(j)$ such that a scaling function at level j is a linear combination of the scaling functions at a finer level j+1. Using these scaling functions, the wavelet $\psi_{j,m}$ at level j and node $m \in M(j)$ can be first initialized, and then improved by the lifting scheme, the basic idea of which is to start with a simple construction of wavelet, and then update it to a new, more complete one.

As detailed in Appendix 2-A, the bi-orthogonal spherical wavelet basis functions used in this work is constructed based on the Butterfly subdivision scheme so that the wavelet basis functions are smooth in the space domain, and therefore vanishing towards high frequency in the frequency domain. Also we initialize the wavelet function as the scaling function at a higher level, and choose a lifting scheme so that the constructed wavelet basis function has a vanishing integral (the

constructed wavelet functions vanish towards low frequency in the frequency domain) [30].

Spherical wavelets constructed in this way have local support in both space and frequency. Using the scaling function at level 0 and wavelets at level 0 and higher, a basis for the function space $L_2 = L_2(S^2, d\omega)$, where $d\omega$ is the usual area measure, is then constructed so that any functions with finite energy can be represented as a linear combination of these basis functions. As detailed in Appendix 1-A, the transformation is easy to carry out without explicitly constructing these wavelet and scaling functions, and fast to compute with a computation time linear in the number of vertices [9].

B – Bi-orthogonality

The spherical wavelets constructed this way are bi-orthogonal [31] (wavelets at the same level and between different levels are not orthogonal to each other such that they are correlated) because currently there are no wavelet bases on the sphere that consist of functions that are orthogonal, compactly supported, symmetric, and smooth [31].

To assess the correlation between a pair of wavelet basis functions, we calculate their correlation coefficients as:

$$\frac{\int \psi_{j,m}\psi_{j',m'}d\omega}{\sqrt{\int|\psi_{j,m}|^2 d\omega \int|\psi_{j',m'}|^2 d\omega}}, \tag{2.5}$$

where $j = j', m \in Neighbor(m')$ for a pair of wavelet functions at the same level, and $j = j'+1$, $m \in M(j)$, $m' \in M(j')$, $m' \in Neighbor(m)$ for a pair of wavelet functions across the consecutive levels.

As a result, we calculate that the averaged correlation coefficient over all the pairs is 0.0225 at the same level, and 0.106 across the adjacent levels. These results indicate fairly weak correlations between wavelet basis functions. Therefore, an approximately orthogonal decomposition can be expected using these spherical wavelet bases. Note that it is possible to apply PCA to completely orthogonalize the wavelet functions. However, the orthogonal PCA bases do not enjoy the locality property of bi-orthogonal wavelets in the spatial-frequency domain and this locality property is key to our subsequent analyses.

2.3.2 Spherical Wavelet Transformation of Cortical Surfaces

In this section, we present the details of using the bi-orthogonal spherical wavelets to transform cortical surfaces preprocessed using the procedure described above.

A – Surface interpolation

As described in Section 2.2, the reconstructed cortical surfaces are mapped onto a sphere and registered in a spherical coordinate system. Therefore, the original spatial coordinates of points on the cortical surface can be considered as functions defined on the sphere. To transform them into the wavelet domain, the spatial coordinates of each subject's cortical surface are first interpolated onto the mesh of an icosahedron mesh subdivided to level = 7 based on their corresponding spherical coordinates established by the spherical registration.

We choose an icosahedron at subdivision level 7 to represent a parameterized sphere because it has a total number of 163,842 vertices and is thus sufficient to represent the spherical map of a

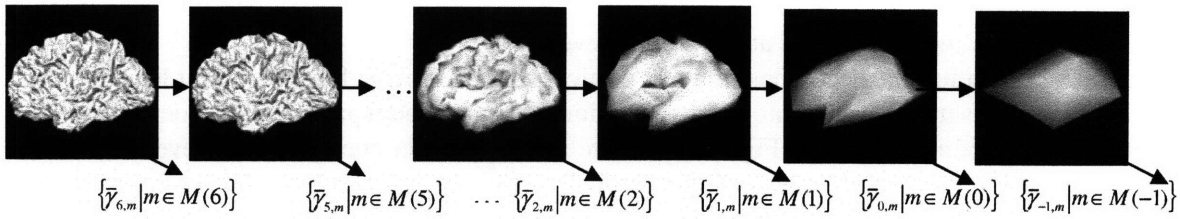

Figure 2-3: Spherical wavelet decomposition of cortical surface from level 7 (the leftmost image). At each level, the surface is further decomposed into lower resolution approximation and wavelet coefficients. Wavelet coefficients at level -1 characterize the overall shape of the cortical surface. Wavelet coefficients at subsequent levels encode the surface spatial variations at finer resolutions.

cortical surface reconstructed from ~1 mm isotropic MRI, which typically has about 120,000 vertices. An icosahedron subdivided 6 levels has only 40,962 vertices and may lead to loss of useful surface details if it is used to represent the finest level sphere parameterization. Conversely, further increasing the resolution of the spherical parameterization will unnecessarily and significantly increase the computation time (an icosahedron at subdivision level 8 has 655,362 vertices).

B – Coordinates normalization

Unlike intrinsic shape features such as curvatures, spatial coordinates of a surface depend on a rather arbitrary coordinate system that each individual subject is originally represented in, and reflects the position of the subject in the scanner at the time of acquisition. In order to use their wavelet coefficients in the following statistical analysis, we need to make these coordinate functions consistent in a dataset, in terms of the rotation, translation and scaling. For this purpose, they need to be normalized with respect to a common reference coordinate frame.

This normalization is initialized by first transforming each spatial coordinate function using the Talairach transformation matrix calculated previously for volume registration during surface reconstruction. Then the roughly normalized coordinate functions of all the surfaces are averaged to create a new template surface in the spatial domain for the second round normalization. Finally, each coordinate function is normalized by finding an optimal affine transformation that minimizes the mean square error between the transformed individual surface and the template.

The normalization process simply aims to bring each subject into the same coordinate system and remove the arbitrary affine components in their coordinate functions; inter-subject shape variations are still preserved after the normalization. In addition, since the surface correspondence is already found by the spherical registration, the affine normalization is robust to compute.

C – Spherical wavelet transformation

The normalized coordinate vector $\mathbf{v} = (x, y, z)^T$ is then expanded by the scaling function at the ground level and a set of spherical wavelet functions as

$$\mathbf{v} = \sum_{k=K(0)} \boldsymbol{\lambda}_{0,k} \varphi_{0,k} + \sum_{j=0,\ldots 6,\ m \in M(j)} \boldsymbol{\gamma}_{j,m} \psi_{j,m} \tag{2.6}$$

where $\boldsymbol{\gamma}_{j,m} = [\gamma^x_{j,m}, \gamma^y_{j,m}, \gamma^z_{j,m}]^T$ is the wavelet coefficient vector corresponding to the x, y and z

coordinates at level j, $j = 0,...6$ and location m, $m \in M(j)$. To simplify notation we define for the coarsest level $M(-1) = K(0)$, $\psi_{-1,k} = \varphi_{0,k}$ and $\gamma_{-1,m} = \lambda_{0,k}$ so that the wavelet coefficients at level -1 is actually the scaling coefficients at the ground level.

Figure 2-2 illustrates the decomposition of a cortical surface starting from the finest level. At each level, the cortical surface is split into a low resolution part and a detail part (wavelet coefficients). As shown in the rightmost figure in Figure 2-2, there are 12 wavelet coefficients at level -1, each of which represents the overall shape of the cortical surface in the region around a vertex on the icosahedron in the underlying spherical coordinate system. At subsequent levels, wavelet coefficients provide descriptions of the spatial variations of the surface at increasingly finer resolutions.

D – Computational time

In this study, both SPHARM and wavelets methods are implemented to compare their ability to capture local shape variations as shown in the next subsection. SPHARM coefficients are estimated by solving for the least square solution of the linear equation (2-4), which has approximately a computational complexity of the cube of the number of the SPHARM coefficients. Therefore, the SPHARM coefficients estimation (highest order = 40) of a typical cortical surface (120,000 vertices) constructed using methods detailed above requires about one hour of computation time on a standard PC architecture.

The spherical wavelet transformation is more efficient (about one minute for typical cortical surface) because it has a computational time linear to the number of vertices. However, the computational cost of SPHARM can be greatly minimized with advanced numerical implementation, such as the iterative residual fitting (IRF) method proposed in [32].

2.3.3 Comparison of SPHARM and Wavelets in Shape Representation

To compare the abilities of SPHARM and spherical wavelets to detect local shape variations, both methods were applied to represent an inflated cortical surface model with a synthesized shape deformation.

A – Experimental setup

A cortical surface model was synthesized by interpolating an inflated cortical surface onto an icosahedron at subdivision level 4 (2562 vertices). The deformation is simulated by moving the 1st and 2nd order neighbors of a vertex, denoted as v, outwards in their normal direction for 4 mm.

After spherical wavelet transformation, the total number of wavelet coefficients is $2562 \times 3 = 7686$, because each of the x, y, and z components in the coefficients vector $\gamma_{j,m}$, as shown in equation 2-6, is evaluated individually in this comparison. The highest order of SPHARM decomposition is chosen to be 60 to achieve a comparable accuracy in shape representation, which therefore results in a total number of $61 \times 61 \times 3 = 11163$ SPHARM coefficients.

With two sets of coefficients computed for both the original and deformed surfaces, a new set of coefficients is made by replacing a certain number of the original surface's coefficients with deformed surface's coefficients that are affected the most by this deformation, using both SPHARM and spherical wavelets methods. The change of coefficient is calculated by $\|c_d| - |c_o\|$, where c_d and

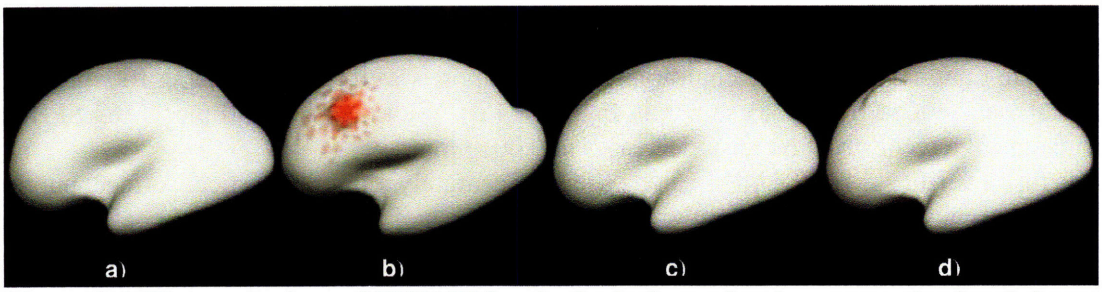

Figure 2-4: The comparison of SPHARM and spherical wavelets in representing local shape variation a). Original inflated cortical surface. b). The deformed surface with red dots indicating the location of the wavelet coefficients that are most affected by the simulated deformation. c). Surface reconstructed with a new set of SPHARM coefficients made by replacing 100 of the original surface's coefficients with deformed surface's coefficients that are most affected by the deformation. d). Surface reconstructed with 100 most varied spherical wavelet coefficients.

c_o denote the corresponding coefficients calculated from the deformed and original surfaces

Table 2.1

Comparison of the number of most varied coefficients used to achieve the same reconstruction error (mm) using SPHARM and spherical wavelets methods. Surface is reconstructed with a new set of coefficients made by replacing a certain number of the original surface's coefficients with deformed surface's coefficients that are most affected by the synthetic deformation. Reconstruction error is measured as the root mean square difference between the reconstructed surface and deformed surface in the deformed region.

Reconstruction Error (mm)	1	1.5	2.5
SPHARM	500	300	100
Wavelets	50	27	7

respectively.

We then reconstruct the deformed surface using this new coefficients set and measure the reconstruction error by $\frac{1}{V}\sum_{i\in\{N_1(v),N_2(v)\}}\left|\mathbf{v}_r^i-\mathbf{v}_d^i\right|$, where $\mathbf{v}_r^i$ and $\mathbf{v}_d^i$ are the coordinates of the i^{th} vertex on the reconstructed and deformed surfaces respectively, $N_1(v)$ and $N_2(v)$ denote the 1st and 2nd neighbors of the vertex v, and V is the total number of vertices in the deformed region.

B – Results

Figure 2-4 a) is the original surface and Figure 2-4 b) shows the set of wavelet coefficients with absolute changes larger than 0.1, with red dots indicating the centers of their support regions. Figure 2-4 b) illustrates the compactness of the wavelet representation as only the coefficients of wavelet functions in the neighborhood of the deformation region are affected. In contrast, the majority of the SPHARM coefficients have changed more than 0.1 compared with the original SPHARM coefficients.

A quantitative comparison of the number of most varied coefficients used to have the same

reconstruction error is given in Table 2.1. With the top 100 most varied SPHARM coefficients, the reconstruction error is 2.5 mm (shown in Table 2.1) and the synthetic bump is not well reconstructed, as shown in Figure 2-4 c). On the contrary, the deformation is well recovered using 100 most varied spherical wavelet coefficients as shown in Figure 2-4 d). With the use of all the 11163 SPHARM coefficients, the reconstruction error decreases to 0.0013 mm.

This result verifies that SPHARM can be used to accurately represent cortical surface, but not as compactly because local shape variation can cause changes of a large number of coefficients. The compactness and the data compression nature of the wavelet transformation are particularly important to reduce multiple comparison problems that often plague the statistical analysis of neuroimaging data.

2.3.4 Applications

As shown above, the developed shape representation based on a spherical wavelet transformation can be used to accurately and efficiently extract shape information in a local fashion in both space and frequency. In this work, we use the wavelet coefficients of the coordinate functions of cortical surfaces registered in the spherical coordinate system as shape features to build multi-scale cortical folding models, and to identify the cortical folding changes related to neuropathology and neurodevelopment.

We first study the patterns of cortical shape variation at different spatial-frequency levels by applying principal component analysis in the wavelet domain. Secondly, by using these wavelet coefficients of cortical surfaces as shape features, we employ statistical learning methods to select shape features that are related to a particular neurological disease, and train a classifier for discriminating patients from normal controls. Furthermore, we develop a nonlinear cortical folding development model based on the wavelet representation to study the change of cortical folds of large and progressively smaller scales in gestation. At last, we use shape models built at multiple spatial resolutions in the wavelet domain to guide the segmentation of the hippocampus based on image-driven models.

Although most of the shape analyses conducted in this thesis are based on transforming coordinates functions of cortical surfaces using spherical wavelets, we can apply the developed wavelet transformation procedure to other features measured for each point on the surface, such as curvature and thickness, and obtain their multi-scale representations. Also, we can use these statistical shape analysis frameworks to study the shape of other neuroanatomical structures that have spherical topology, such as the hippocampus and the caudate nucleus.

2.4 Contributions

In this chapter, we presented a new method to extract shape features at different locations and spatial scales of the surface of neuroanatomical structures, such as the cerebral cortex, by using a bi-orthogonal spherical wavelet transformation. The contributions of our work presented in this chapter are the following:

1) To our knowledge, this approach is the first one that has been proposed to extract multi-scale and localized shape features of neuroanatomical structure, particularly cortical surfaces, in parallel to the wavelet-based shape representation developed for sub-cortical structures by Nain *et. al* [28].

2) We develop a procedure to extract comparable shape features of a set of registered surfaces, which can be used in statistical analysis.

3) Our shape representation allows for easy visualization and interpretation of the shape information characterized by each shape feature, which is of great use in the medical context.

The entire procedure is implemented and integrated into a publicly available software package Freesurfer [12], which is downloaded and used by thousands of scholars worldwide.

A preliminary version of this work was presented at the *IEEE Computer Society Workshop on Mathematical Methods in Biomedical Image Analysis* in conjunction with *IEEE Computer Society Conference on Computer Vision and Pattern Recognition* [33]. A journal version of this work was published in *IEEE Transactions on Medical Imaging* [34].

APPENDIX 2-A. FAST SPHERICAL WAVELETS TRANSFORMATION

In this work, we used the interpolation scaling function defined as:

$$\varphi_{j,k}(v_{j,k'}) = \delta_{k-k'} \quad for \quad k,k' \in K(j)$$

where $v_{j,k}$ denotes the k^{th} vertex at subdivision level j ($k \in K(j)$). The same notation is used here as in the main text so that $K(j)$ and $M(j)$ denote all vertices on the mesh before and after the j^{th} subdivision. As a result, the scaling coefficients at level j of a function f interpolated on the j^{th} order icosahedron are the values of this function at each vertex, i.e.

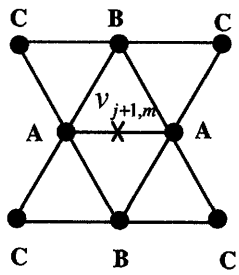

Fig. 2A-1. Local neighborhoods for the Butterfly scheme, where vertex sets A, B and C are used in determining the new value at the center edge midpoint.

$$\lambda_{j,k} = f(v_{j,k}), k \in K(j) \tag{2A.1}$$

A butterfly subdivision scheme is used such that the value of a scaling coefficient at level $j+1$ can be found as:

$$\lambda_{j+1,m} = 1/2\sum_{k\in A(j,m)}\lambda_{j,k} + 1/8\sum_{k\in B(j,m)}\lambda_{j,k} - 1/16\sum_{k\in C(j,m)}\lambda_{j,k} \tag{2A.2}$$

where $A(j,m)$, $B(j,m)$ and $C(j,m)$ are local neighbors of vertex $v_{j+1,m}$ as shown in Figure 2A-1. The butterfly procedure is used to generate smooth wavelet functions.

Next, a lifting algorithm is used to construct wavelet function as:

$$\psi_{j,m} = \varphi_{j+1,m} - \sum_{k\in A(j,m)} s_{j,k,m}\varphi_{j,k} \tag{2A.3}$$

where $s_{j,k,m} = I_{j+1,m}/2I_{j,k}$ with $I_{j,k} = \int \varphi_{j,k} d\omega$. This ensures that the constructed wavelet function has a vanishing integral, i.e. one vanishing moment. The wavelet function constructed in this way has a local support in frequency because its value is vanishing in both the high frequency due to the smoothness and low frequency due to the vanishing integral.

In this work, the coordinate function is interpolated onto the 7^{th} order icosahedron. The resulting scaling coefficients at the highest level are therefore the values of the interpolated coordinate function at each vertex on the icosahedron at subdivision level=7. The wavelet coefficients can be calculated in two steps (Analysis step I and II) recursively as shown below:

Analysis Step I: Calculate the $\gamma_{j,m}$ as follows

$$\begin{aligned}\forall m \in M(j): \gamma_{j,m} := \lambda_{j+1,m} - 1/2\sum_{k\in A(j,m)}\lambda_{j,k} - \\ 1/8\sum_{k\in B(j,m)}\lambda_{j,k} + 1/16\sum_{k\in C(j,m)}\lambda_{j,k}.\end{aligned} \tag{2A.4}$$

Analysis Step II: Calculate the $\lambda_{j,k}$ using the $\gamma_{j,m}$ from step I

$$\begin{aligned}\forall k \in K(j): \lambda_{j,k} = \lambda_{j+1,k} \\ \forall m \in M(j): \forall k \in A(j,m): \lambda_{j,k} += s_{j,k,m}\gamma_{j,m}.\end{aligned} \tag{2A.5}$$

The inverse transformation can be implemented in two steps (Synthesis step I and II) as well:

Synthesis Step I: Calculate the $\lambda_{j+1,k}$:

$$\begin{aligned}\forall k \in K(j): \lambda_{j+1,k} = \lambda_{j,k} \\ \forall m \in M(j): \forall k \in A(j,m): \lambda_{j+1,k} -= s_{j,k,m}\gamma_{j,m}.\end{aligned} \tag{2A.6}$$

Synthesis Step II: Calculate $\lambda_{j+1,m}$ using the $\lambda_{j+1,k}$ from step I:

$$\forall m \in M(j): \lambda_{j+1,m} := \gamma_{j,m} + 1/2 \sum_{k \in A(j,m)} \lambda_{j+1,k} + 1/8 \sum_{k \in B(j,m)} \lambda_{j+1,k} - 1/16 \sum_{k \in C(j,m)} \lambda_{j+1,k}. \quad \text{(2A.7)}$$

Bibliography

[1] L. Staib and J. Duncan, "Model-based deformable surface finding for medical images," IEEE Transactions on Medical Imaging, vol. 15, pp. 720-731, 1996.

[2] A. Kelemen, G. Szekely, and G. Gerig, "Elastic model-based segmentation of 3d neuroradiological data sets," IEEE Transactions on Medical Imaging, vol. 18, pp. 828-839, 1999.

[3] C. Brechbuhler, G. Gerig, and O. Kubler, "Parametrization of Closed Surfaces for 3-D Shape Description," Computer Vision and Image Understanding, vol. 61, pp. 154-170, 1995.

[4] C. Brechbuhler, G. Gerig, and O. Kubler, "Parametrization of Closed Surfaces for 3-D Shape Description," Computer Vision and Image Understanding, vol. 61, pp. 154-170, 1995.

[5] G. Gerig, M. Styner, D. Jones, D. Weinberger, and J. Lieberman, "Shape analysis of brain ventricles using spharm," Mathematical Methods in Biomedical Image Analysis, pp. 171-178, 2001.

[6] L. Shen, J. Ford, F. Makedon, and A. Saykin, "hippocampal shape analysis surface-based representation and classification," SPIE Medical Imaging, 2003.

[7] G. Gerig, M. Styner, and J. Lieberman, "Shape versus Size: Improved understanding of the morphology of brain structures," Proc. MICCAI 2001, pp. 24-32, 2001.

[8] M. K. Chung, K. M. Dalton, L. Shen, A. C. Evans, and R. J. Davidson, "Weighted Fourier series representation and its application to quantifying the amount of gray matter," IEEE Transactions on Medical Imaging, pp. 566-581, 2007.

[9] P. Schroder and W. Sweldens, "Spherical wavelets: Efficiently representing functions on a sphere," Proceedings of the 22nd annual conference on Computer Graphics and Interactive Techniques, vol. 29, pp. 161-172, 1995.

[10] P. Yu, P. E. Grant, Y. Qi, X. Han, F. Segonne, R. Pienaar, E. Busa, J. Pacheco, N. Makris, R. L. Buckner, P. Golland, and B. Fischl, "Cortical surface shape analysis based on spherical wavelets,," IEEE Transaction on Medical Imaging, vol. 26, pp. 582-598, 2007.

[11] B. T. T. Yeo, W. Ou, and P. Golland, "On the construction of invertible filterbank on the 2-sphere," Technical Report, http://people.csail.mit.edu/ythomas/IFB2006.pdf, 2006.

[12] "http://surfer.nmr.mgh.harvard.edu."

[13] A. M. Dale, B. Fischl, and M. I. Sereno, "Cortical surface-based analysis I: Segmentation and surface reconstruction," Neuroimage, vol. 9, pp. 179-194, 1999.

[14] B. Fischl, M. I. Sereno, and A. M. Dale, "Cortical surface-based analysis. II: Inflation, flattening, and a surface-based coordinate system," Neuroimage, vol. 9, pp. 195-207, 1999.

[15] B. Fischl, A. M. Dale, M. I. Sereno, R. B. H. Tootell, and B. R. Rosen, "A coordinate system for the cortical surface," NeuroImage, vol. 7, pp. S740, 1998.

[16] M. J. Brammer, "Multidimensional wavelet analysis of functional magnetic resonance images," Human Brain Mapping, vol. 6, pp. 378 - 382, 1998.

[17] C. Davatzikos, X. Tao, and D. Shen, "Hierarchical active shape models, using the wavelet transform," IEEE Trans. Medical Imaging, vol. 22, pp. 414-423, 2003.

[18] R. D. Nowak, "Wavelet-based rician noise removal for magnetic resonance imaging.," IEEE Transactions on Image Processing, vol. 8, pp. 1408?419, 1999.

[19] A. Natsev, "Multiresolution wavelet representations for arbitrary meshes," Duke University Report, 1997.

[20] K. Kolarov and W. Lynch, "Optimization of the SW algorithm for high dimensional compression," Proceedings of Compression and Complexity Sequences, pp. 194-203, 1998.

[21] L. Pastor and A. Rodriguez, "Surface approximation of 3D objects from irregularly sampled clouds of 3D points using spherical wavelets," Proceedings of the 10th International Conference on Image Analysis and Processing, pp. 70-75, 1999.

[22] H. Hoppe and E. Praun, "Shape compression using Spherical Geometry Images," Advances in Multiresolution for Geometric Modeling, pp. 27-46, 2003.

[23] Z. Wang, C. Leung, Y. Zhu, and T. Wong, "Data compression with spherical wavelets and wavelets for the image-based relighting," Computer Vision and Image Understanding, pp. 327-344, 2004.

[24] T. Darom, M. R. Ruggeri, D. Saupe, and N. Kiryati, "Processing of textured surfaces represented as surfel sets: representation, compression and geodesic paths," IEEE International Conference on Image Processing (ICIP), pp. I-605-8, 2005.

[25] H. Laga, H. Takahashi, and M. Nakajima, "Spherical wavelet descriptors for content-based 3D model retrieval," Proceedings of IEEE International Conference on Shape Modeling and Applications (SMI'06), pp. 15, 2006.

[26] I. R. Greenshields, "3D Shape approximants via spherical wavelet decomposition," Proceedings of the 14th IEEE Symposium on Computer-Based Medical Systems, pp. 31-35, 2001.

[27] P. Yu, F. Segonne, X. Han, and B. Fischl, "Shape analysis of neuroanatomical structures based on spherical wavelets," Presented at 11th Annual Meeting of the Organization of Human Brain Mapping (HBM), Toronto, Canada, June 2005.

[28] D. Nain, S. Haker, A. Bobick, and A. Tannenbaum, "Multiscale 3d shape analysis using spherical wavelets," presented at MICCAI, Oct 26-29 2005.

[29] D. Nain, S. Haker, A. Bobbick, and A. Tannenbaum, "Shape-driven surface segmentation using spherical wavelets," presented at MICCAI, Oct 1-6, 2006.

[30] P. Schroder and W. Sweldens, "Spherical Wavelets: Texture Processing," in Rendering Techniques, 1995, pp. 252-263.

[31] E. J. Stollnitz, T. D. DeRose, and D. H. Salesin, Wavelets for Computer Graphics: Theory and Applications. San Francisco: Morgan Kaufmann, 1996.

[32] L. Shen and M. K. Chung, "Large-scale modeling of parametric surfaces using spherical harmonics," presented at Third International Symposium on 3D Data Processing, Visualization and Transmission (IEEE 3DPVT), UNC, Chapel Hill, USA, 2006, June 14-16.

[33] P. Yu, X. Han, F. Segonne, R. L. Buckner, R. Pienaar, P. Golland, P. E. Grant, and B. Fischl, "Cortical surface shape analysis based on spherical wavelet transformation.," Oral presentation in IEEE Computer Society Workshop on Mathematical Methods in Biomedical Image Analysis (MMBIA 2006), New York City, NY, June 2006.

[34] P. Yu, B. T. T. Yeo, P. E. Grant, B. Fischl, and P. Golland, "Cortical folding development study based on over-complete spherical wavelets," Proceedings of the IEEE International Conference on Computer Vision,, 2007.

Chapter 3

Multi-scale Shape Models Based on Principal Component Analysis

In this chapter, we propose to build shape models at multiple resolutions by applying principal component analysis in the spherical wavelet domain. We demonstrate the use of this method in detecting cortical folding variations of progressively smaller spatial scales for cortical surfaces in a synthetic dataset. We then apply this method to study and visualize the localized cortical folding variations in a nondemented elderly population. Furthermore, we investigate the correlations of these observed cortical folding variations with age, gender and a set of psychological measurements. Finally, we show the use of the proposed method in studying the cortical folding development in a small dataset of newborn.

3.1 Introduction

Although the human brain has consistent anatomical structures across individuals, striking morphological variations, including differences in the volume and shape of cortical and subcortical structures, are observed in the normal population [1-5]. Such normal variations have complicated the goals of understanding the morphological abnormalities of neuroanatomical structures associated with neurological diseases. Therefore, it is of great importance to distinguish idiosyncratic shape variations from disease-related shape changes in brain structures.

Principal Component Analysis (PCA) is a useful tool for finding patterns in data of high dimension. It has been extensively used in the fields of computer vision and image recognition. Based on this technique, Cootes *et al.* [6] built 2D generative models of shape variation within a single population based on a point boundary model, which consists of a list of coordinates of points on the object boundary. For example, if $\mathbf{x}^n (n = 1, \cdots N)$ denotes a vector containing the coordinates of the points on the boundary calculated for the n^{th} subject in a group of N subjects, then any individual shape can be decomposed as:

$$\mathbf{x}^n = \bar{\mathbf{x}} + \sum_{l=1}^{k} \mathbf{e}^l \mathbf{e}^{lT} (\mathbf{x}^n - \bar{\mathbf{x}}), \tag{3.1}$$

where $\bar{\mathbf{x}}$ is the mean of $\mathbf{x}^n (n = 1, \cdots N)$, $\mathbf{e}^1, \cdots, \mathbf{e}^k$ are the eigenvectors corresponding to eigenvalues $\lambda^1, \lambda^2, \cdots, \lambda^k$ of the covariance matrix of $\mathbf{x}$, in decreasing order.

This is essentially equivalent to linearly transforming a dataset into a new coordinate system such that the variance of the projection of the dataset on the first axis (first principal component) is the greatest, and the variance of projection on the second axis is the second greatest, and so on. The fact that the variance explained by each eigenvector is equal to the corresponding eigenvalue enables us to study the most significant modes of variation in the dataset.

Usually, most of the variations can be sufficiently represented by a small number of modes, *k*, so that the sum of the first *k* variances represents a sufficiently large proportion of total variance of all the variables used to derive the covariance matrix. Thus by limiting the number of terms in equation 3.1, the statistical analysis can be greatly simplified. This method has been further extended to build shape models and successfully used to segment 2D and 3D medical images [7-9].

However, it has been argued that omitting the eigenvectors corresponding to relatively small shape variations leads to the failure of characterizing subtle, yet important shape features because coordinates of all the points on the surface are used as the shape feature inputs [10]. For the same reason, the application of PCA in the shape study of neuroanatomical structures (i.e. the cortical surface) has also been largely limited. To address this problem, Shen *et al.* [11] first proposed to build hierarchical active shape models of 2D objects (such as the corpus callosum) using 1D wavelets, which were then used for shape based image segmentation.

In this work, we apply PCA to build shape models in the spherical wavelet domain for studying regional cortical folding variations within a group of normal subjects at multiple spatial resolutions [12]. A similar method was proposed to learn a shape prior of 3D objects (such as prostate and caudate nucleus) by applying PCA to the clusters of correlated spherical wavelet coefficients [13], and to use this prior for image segmentation based on the spherical wavelets presentation [14]. In our work, we focus on the use of PCA to study and visualize the major patterns of shape variation of cortical surfaces and the correlation of these folding variations with age and neuropsychological functions at different spatial scales based on spherical wavelet transformation.

3.2 Methods

In this section, we introduce the proposed shape modeling of neuroanatomical structures based on PCA in the wavelet domain, and demonstrate the results on the cortical folding study in synthetic and real dataset. This method can be also used to study the shape of other brain structures that have spherical topology, such as hippocampus, which will be demonstrated in Chapter 6.

3.2.1 Shape Models Based on PCA in the Wavelet Domain

In this work, we propose to conduct PCA on spherical wavelet coefficients of coordinate function at different frequency levels separately. Using principal components calculated at separate frequency levels, we build shape models at different spatial resolutions since the wavelet coefficients in the lowest level provide an overall approximation and localized morphological variations are captured hierarchically by the higher-level coefficients.

We first preprocess the cortical surfaces and calculate the normalized wavelet coefficients $\{\boldsymbol{\gamma}_{j,m}\}_{j=-1,\ldots 6,\ m\in M(j)}$ for a set of N registered surfaces, as described in Chapter 2, where $\boldsymbol{\gamma}_{j,m}$ is the 3-dimensional wavelet coefficient vector corresponding to the x, y and z coordinates at level j, $j=-1,\ldots 6$ and location m, $m\in M(j)$. Each time we take only $\boldsymbol{\gamma}_j^n=\{\boldsymbol{\gamma}_{j,m}^n\}_{m\in M(j)}$, the subset of the wavelet coefficients at the j^{th} frequency level of a set of subject, and calculate the mean wavelets at this level as $\bar{\boldsymbol{\gamma}}_j=\frac{1}{N}\sum_{n=1}^{N}\boldsymbol{\gamma}_j^n$. For each shape in the dataset, we calculate its deviation from the mean as $d\boldsymbol{\gamma}_j^n=\boldsymbol{\gamma}_j^n-\bar{\boldsymbol{\gamma}}_j$, and the covariance matrix as $\mathbf{C}=\frac{1}{N}\sum_{n=1}^{N}d\boldsymbol{\gamma}_j^n(d\boldsymbol{\gamma}_j^n)^T$. We denote the number of spherical coefficients at level j as M_j, and the size of the covariance matrix is therefore $3M_j\times 3M_j$. A set of orthonormal eigenvectors $\mathbf{e}_j^1,\cdots,\mathbf{e}_j^k$ is then calculated so that

$$\lambda_j^l\mathbf{C}=\mathbf{C}\mathbf{e}_j^l,\ \ l=1,\ldots k, \tag{3.2}$$

Where the eigenvalues $\lambda_j^1,\lambda_j^2,\cdots,\lambda_j^k$ are the variances explained by corresponding eigenvectors.

To visualize the shape variations corresponding to the principal components $\mathbf{e}_j^l(l=1,\cdots k\le N-1)$ at the j^{th} frequency level, we calculate the projections of spherical wavelets of each surface onto the first k eigenvectors $\mathbf{p}_j^n=\mathbf{e}_j^T d\boldsymbol{\gamma}_j^n$ by using the matrix $\mathbf{e}_j=[\mathbf{e}_j^1,\ldots,\mathbf{e}_j^k]$. Then for each subject, we can generate a new set of new wavelet coefficients $\tilde{\boldsymbol{\gamma}}^n=\{\bar{\boldsymbol{\gamma}}_{-1},\ldots,\bar{\boldsymbol{\gamma}}_j+\mathbf{e}_j\mathbf{p}_j^n,\ldots,\bar{\boldsymbol{\gamma}}_6\}$ by adding the averaged wavelets coefficients over all the surfaces. The new surface $\tilde{S}=\mathbf{W}\tilde{\boldsymbol{\gamma}}^n$, where $\mathbf{W}$ is the inverse wavelet transformation matrix, generated by inversely transforming the new wavelet coefficients, carries only the shape information explained by the first k eigenvectors at level j.

3.2.2 Shape Pattern Recognition in Synthetic Data

To validate the usage of the proposed method in distinguishing and characterizing regional shape variations among a dataset at multiple spatial resolutions, we construct a synthetic dataset and conduct the PCA at separate frequency levels. MR brain images of five healthy female subjects, all approximately 71 years old, were selected, and the average of their cortical surfaces was used as the template for generating the synthetic dataset.

The top row in Figure 3-1 shows the five synthetic cortical surfaces, each with a bump located in the same region around the anterior tip of the temporal lobe. The deformation was created by moving each vertex in the deformation region outward along its normal direction by a specified distance, which increases from 0 mm for the first surface to 2 mm for the last surface. These five synthetic surfaces were registered and transformed into the wavelet domain using the procedures described in Chapter 2.

The PCA study of the wavelets coefficients shows that about 98% of the shape variation was accounted for by the first principal component at all the frequency levels. As described in the previous section, we construct a set of projected wavelet coefficients for each surface to visualize the shape changes captured by the first principal component at different frequency level:

$$\tilde{\boldsymbol{\gamma}}_j^n=\mathbf{e}_j^1\mathbf{e}_j^{1T}(\boldsymbol{\gamma}_j^n-\bar{\boldsymbol{\gamma}}_j), \tag{3.3}$$

where $\boldsymbol{\gamma}_j^n$ is the subset of wavelet coefficients of the n^{th} surface at j^{th} level, $\bar{\boldsymbol{\gamma}}_j$ is the averaged wavelet coefficients of all the surfaces at the j^{th} level, and $\mathbf{e}_j^1$ is the first eigenvector calculated at the

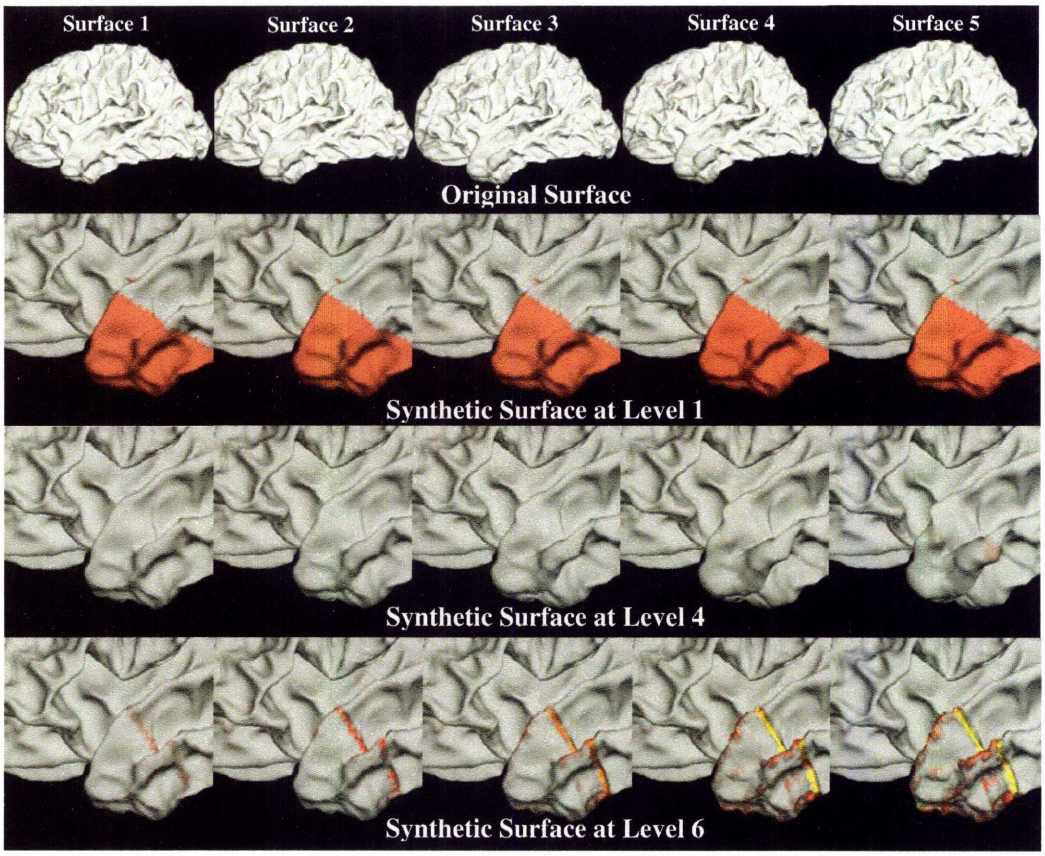

Figure 3-1: Shape variations detected with PCA in synthetic data: The original surfaces with synthetic bump on the temporal lobe are shown in first row; The second to the fourth rows are the reconstructed surfaces using projected wavelet coefficients at levels 1, 4 and 6. (Colormap indicating the magnitude and spatial scale of shape variation detected by PCA)

j^{th} level. Then the whole set of projected wavelet coefficients $\tilde{\boldsymbol{\gamma}}^n = \{\boldsymbol{\gamma}^1_{-1}, \ldots, \bar{\boldsymbol{\gamma}}_j + \tilde{\boldsymbol{\gamma}}^n_j, \ldots, \boldsymbol{\gamma}^1_6\}$ is constructed by adding the first surface's wavelet coefficients.

Figure 3-1 illustrates the surfaces generated by taking inverse wavelet transformation of these projected wavelet coefficients from low to high levels, with color indicating the magnitude and spatial coverage of each wavelet coefficient in $\tilde{\boldsymbol{\gamma}}^n_j$. It shows that the overall synthetic shape change of the temporal lobe is captured exclusively at the low frequency level (in the 2nd row of Figure 3-1). And the sharp shape change on the boundary of the bump is identified at the high frequency level (bottom row in Figure 3-1) in the highlighted region. However, we find no significant changes at the middle frequency level, indicated in the 3rd row in Figure 3-1. This observation is consistent with the fact that the synthetic deformation does not feature changes of secondary folds on the temporal lobe.

These results demonstrate that we can discover major modes of shape variation not only at different spatial resolutions, but also in different spatial regions by applying PCA in the spherical wavelet domain.

3.3 Experimental Results and Discussions

Using this method, we analyze two sets of high-resolution structural MR scans in this chapter. The first dataset is mainly used to study the major modes of cortical folding variation and aging-related folding changes of gray/white matter boundaries in a healthy older population. In the second dataset, we use the proposed method to visualize the folding development of 5 neonates at multiple spatial resolutions.

3.3.1 Shape Variation in Aged Normal Population

The first dataset was obtained from a total of 84 nondemented older participants (42 women: 67 - 95, mean age = 80, standard derivation = 7.25; 42 men: 71-94, mean age = 79, standard derivation = 7.17). These data have been reported previously in several publications associated with the Washington University Alzheimer's Disease Research Center (ADRC). None of the participants had any history of neurologic, psychiatric, or medical illness that could contribute to dementia or a serious medical condition. Two to four high-resolution MP-RAGE scans were motion corrected and averaged per participant (four volumes were averaged for all except five participants; Siemens 1.5T Vision System, resolution 1 × 1 × 1.25 mm, TR = 9.7 ms, TE = 4 ms, FA = 10° , TI = 20 ms, TD = 200 ms) to create a single high contrast-to-noise image volume. These acquisition parameters were empirically optimized to increase gray/white and gray/cerebrospinal fluid contrast. Cortical surfaces were reconstructed and registered as described in Chapter 2.

A – Visualization of surface variations

The PCA study of the wavelet coefficients in this dataset demonstrates a wide range of differences of cortical surface geometry, in both the overall shape of the cortex and the hierarchically finer local details. Most of the shape variance (98%) is represented by the first 10 to 20 eigenvectors and the variance explained by the first principal component ranges from 8% to 13% of the total variance at the lower spatial-frequency levels. Shape variances of higher spatial scales are spread out more evenly over 50 to 80 eigen-components.

The shape variation represented by the l^{th} principal component at the j^{th} frequency level is illustrated by generating two sets of new wavelet coefficients:

$$\tilde{\gamma}^l_{j_\pm} = \pm 3\sigma^l_j \mathbf{e}^l_j = \pm 3\sqrt{\lambda^l_j}\mathbf{e}^l_j, \tag{3.4}$$

where λ^l_j is the l^{th} eigenvalue of the covariance matrix of the wavelet coefficients at level j. Then we generate two new coefficient sets consisting of wavelet coefficients at all levels by adding the average wavelet coefficients of the entire dataset. At last, two synthetic surfaces $\tilde{S}^l_{j_{\pm 3\sigma}}$ are generated by inversely transforming these two sets of wavelet coefficients. By comparing these two synthetic surfaces, we can visualize the shape variations characterized by the corresponding principal components at separate frequency level.

As an example, we shows in Figure 3-2 the synthetic surfaces generated for the left hemisphere at levels -1 to 1, with the colormap indicating the l_2 norm, location and support region of each coefficient in the first eigenvector $\mathbf{e}^1_j$. Note that one cannot directly compare the color scales at different levels, since the wavelet functions are not normalized across levels in these results. This is because the normalization would lead to large differences between the wavelet coefficients across levels, masking the fine details in visualization. Because the support regions of neighbor wavelet basis functions overlap with each other, the color of each point on the cortical surface is assigned by the l_2 norm of the coefficient whose center of support is the closest. A set of arrows is used to point

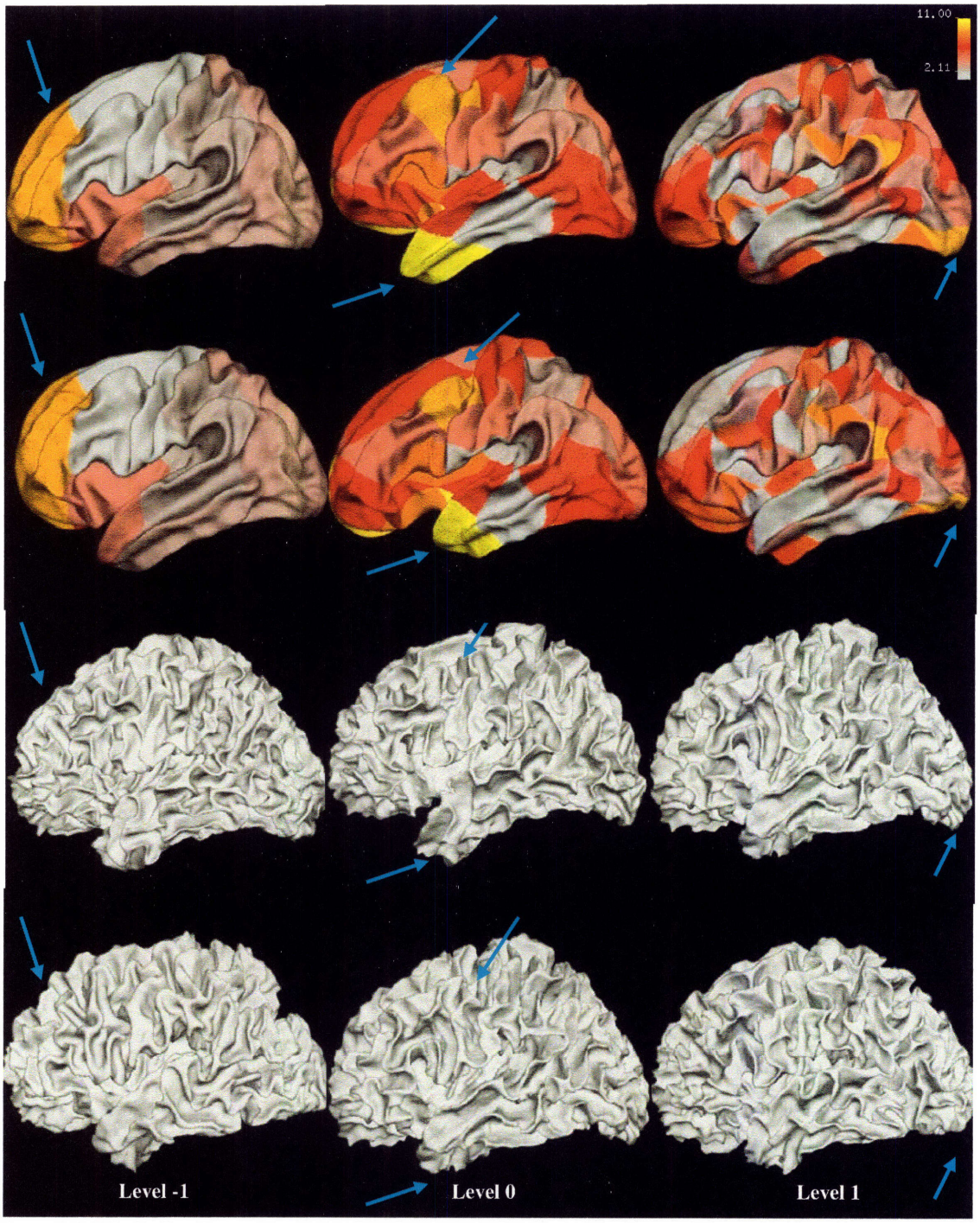

Figure 3-2: Principal surfaces at level -1 to 1 and real cortical surfaces. Top 2 rows: The synthetic surfaces representing the $\mp 3\sigma$ variations (ordered in top-down direction) of the first principal component at levels -1, 0 and 1; Colormap shows the spatial coverage and l^2 norm of each wavelet coefficients in the first principal component; The color of each point on the cortical surface is assigned by the l^2 norm of the coefficient whose center of support is the closest; At the same level, the higher the intensity is, the larger the shape variation is across the entire dataset. Note that one cannot directly compare the colors at different levels, since the wavelet functions are not normalized across levels. (This normalization would lead to a wild difference between the wavelet coefficients across levels, masking the fine details in visualization.) Bottom 2 rows: corresponding real surfaces that have the largest positive and negative projections on the first eigenvector (real $\mp 3\sigma$ surfaces). A set of arrows is used to point to the regions that vary the most across subjects at each level.

out the regions that vary the most across subjects at each level. For example, at the lowest frequency level, we observe a significant change of the overall shape of prefrontal cortex. At level 1, there is a wide range of folding variations including the bulginess of the medial frontal gyrus and the protrusion of temporal lobe. At level 2, we also observe cortical shape variations in different brain regions including the occipital lobe corresponding to Brodmann area 17.

Two real left hemisphere surfaces (hereafter referred to as real $\pm 3\sigma$ surfaces) that have the largest positive and negative projections on the first principal component are also shown in Figure 3-2 for comparison. The cortical folding differences between the $\widetilde{S}_{\pm 3\sigma}$ synthetic surfaces (first row and second row) are clearly visible in the real $\pm 3\sigma$ surfaces as well (third and four rows), which verifies the cortical folding variations detected by the PCA methods.

B – Aging-related cortical shape variations

The results of the PCA study above demonstrate a large amount of cortical folding variation in the healthy elderly population. To further our understandings, we investigate the relationship between the observed shape variations and a set of input variables including subjects' age, gender and five neuropsychological test scores that were used to assess if the subject has dementia. These scores are Mini Mental State Examination (MMSE), Wechsler Memory Scale (WMS) Long Memory, WMS Digit Span, WMS Associates Recall Easy, and WMS Associates Recall Hard.

The relationship between shape variations (response variable) at the j^{th} level and these input variables are assessed in the female and male groups using multiple linear regression:

$$\begin{aligned} &\mathbf{y} = \mathbf{X}\boldsymbol{\beta} + \boldsymbol{\varepsilon}, \\ &\mathbf{y} = \left[p_j^{k1}, \ldots, p_j^{kN_f}, p_j^{k1}, \ldots, p_j^{kN_m}\right]^T, \\ &\mathbf{X} = \begin{bmatrix} \mathbf{1}, \mathbf{X}^f & \mathbf{0} \\ 0 & \mathbf{1}, \mathbf{X}^m \end{bmatrix}, \\ &\boldsymbol{\beta} = \begin{bmatrix} \boldsymbol{\beta}_j^f \\ \boldsymbol{\beta}_j^m \end{bmatrix}, \end{aligned} \tag{3.5}$$

where $p_j^{kn} = \mathbf{e}_j^{kT} d\boldsymbol{\gamma}_j^n, n = 1, \ldots, N_f$ are projections of the female subjects on the k^{th} principal component $\mathbf{e}_j^k$, and $p_j^{kn} = \mathbf{e}_j^{kT} d\boldsymbol{\gamma}_j^n, n = 1, \ldots, N_m$ are the projections of the male subjects, input variables $\mathbf{X}^f$ is the matrix containing the set of 6 features for N_f subjects in female group, and $\mathbf{X}^m$ is for N_m subjects in the male group. The parameters $\boldsymbol{\beta}_j = [\beta_j^0, \beta_j^1, \ldots, \beta_j^6]^T$, corresponding to the intercept and 6 input variables, are estimated for female and male groups separately to allow different slopes and intercept. These parameters are estimated as the least square solutions of the equation (3.5). We use F-statistic to test the significance of each parameter, and the differences between female and male groups of corresponding parameters [15].

As an example, we study the linear relationship between the shape variation characterized by the first eigenvector and the 6 input variables for both left and right hemispheres. Using multiple linear regression, we find the cortical folding variation in female group is not related with the neuropsychological scores. The shape variance in male group, on the contrary, is significantly correlated with several neuropsychological scores, mainly on the right side and at the high frequency levels (levels 4-6). Specifically, only WMS Digit Span is found be significant for the left hemisphere in the male group. On the other hand, four scores including WMS Long Memory, WMS Digit Span, WMS Associates Recall Easy, and WMS Associates Recall Hard are found to be significant for the

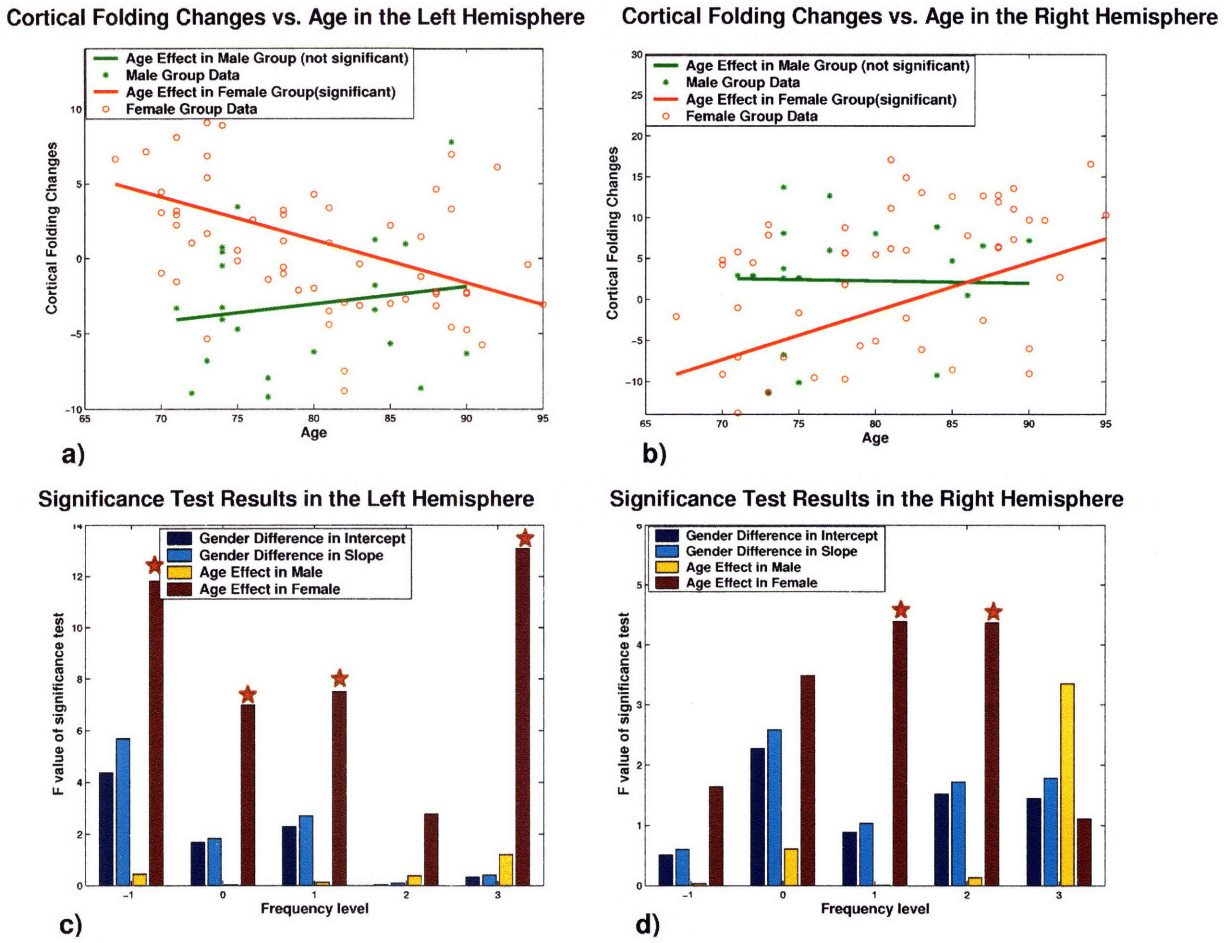

Figure 3-3: The aging effect on the cortical shape variation in the male and female groups. a) The estimated regression line of the projections of wavelet coefficients on the 1st principal component with age in male (green) and female (red) groups in the left hemisphere. b) The regression line in the right hemisphere. c) F value of the significance test for age and gender effect in the left hemisphere (red star indicates a corresponding p value smaller than 0.05). d) F value of the significance test for age and gender effect in the right hemisphere (red star indicates a corresponding p value smaller than significance = 0.05).

right hemisphere in the male group. Visual inspection in the real dataset shows that the related shape variations are of small spatial scales. These results provide interesting research directions for further understanding the structure-function relationships and the gender difference of the human cortex.

Interestingly, the effect of age on the cortical folding variations is found in female group at the low frequency levels, and significantly stronger on the left side. These results are opposite to the observed effect of neuropsychological scores in terms of gender, hemisphere, and frequency levels. To demonstrate these results, we plot the estimated regression lines of shape variation with age for male and female group in Figure 3-3 a) and b). We also show the significance test results for both left and right hemispheres in Figure 3-3 c) and d), where the red star indicates that the corresponding p value is smaller than a pre-selected significance threshold = 0.05.

From these results, we observe that the cortical folding variations (gray/white matter boundary)

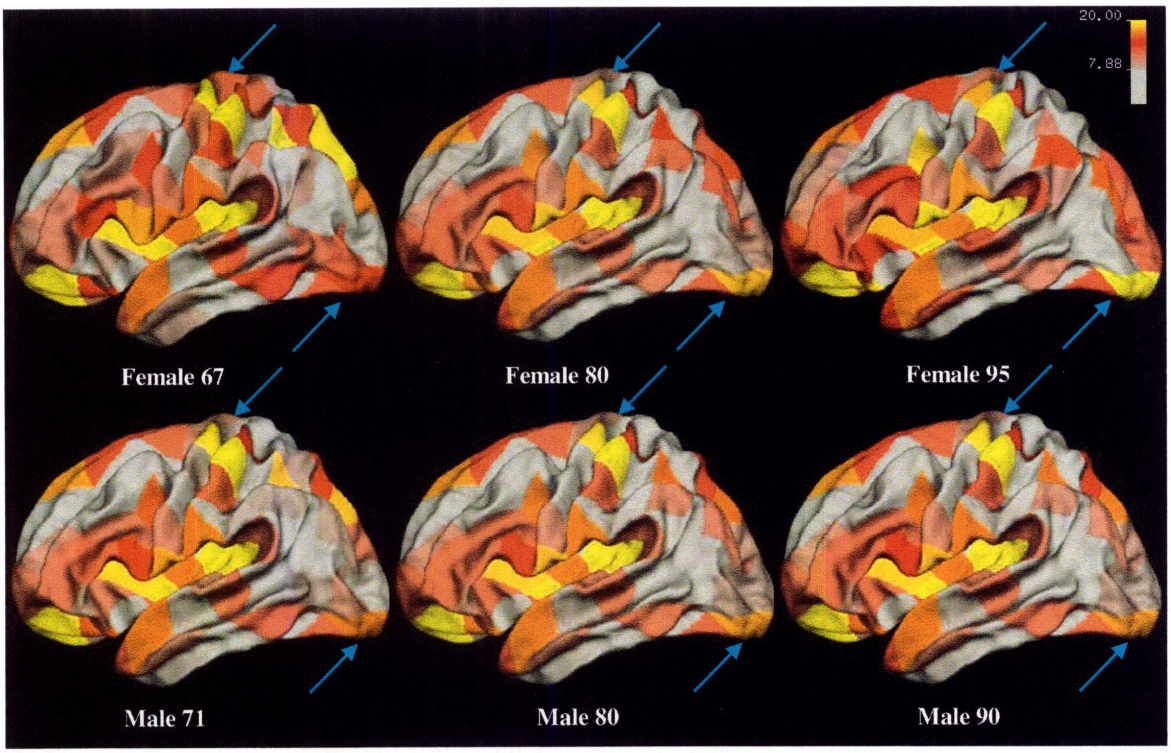

Figure 3-4: Reconstructed surfaces for female (top row) and male (bottom row) subjects of different ages using projected wavelet coefficients on the set of principal components that represent 98% of the total variance at level 1. Colormap encodes the l^2 norm, location and support region of the projected coefficients of each subject. An arrow is pointed to a region of decreasing intensities with age on the precentral sulcus in the female group; another arrow is pointed to a region of increasing intensities with age on the occipital lobe in the female group; Visual inspection identifies the narrowing of central sulcus and elongation of occipital lobe; Neither these intensity changes nor shape changes are salient in the male group.

on the left hemisphere are strongly dominated by healthy aging in the female group. We can visually inspect the changes of cortical surface with age in the space spanned by the first a few principal components $\mathbf{e}_j = [\mathbf{e}_j^1, \ldots, \mathbf{e}_j^k]$ at each frequency level j. For example, we reconstruct the projected surface of the n^{th} subject at the j^{th} level by inversely transforming a new set of wavelet coefficients containing the projected wavelet coefficients on the set of eigen-components that represent 98% of the total variation at the j^{th} level, and the mean wavelet coefficients at other levels.

As an example, Figure 3-4 shows the projected cortical surfaces in three age ranges of female and male subjects at level 1. The colormap encodes the l_2 norm, location and support region of the projected coefficients of each subject on the set of eigenvectors representing 98% of the total variance. An arrow is pointed to a region of decreasing intensities with age on the precentral sulcus, indicating a decreased folding of this area. Another arrow is pointed to a region of increasing intensities with age on the occipital lobe, indicating an increased folding in this area. Visual inspection of the whole population confirms the corresponding shape variations in the left hemisphere are the narrowing of the central sulcus and the elongation of the occipital lobe, which may characterize and correlate with white matter atrophy. As indicated by multiple regression study, these changes are not salient in male groups as the color intensities in these two regions do not vary much as shown in the second row of Figure 3-4.

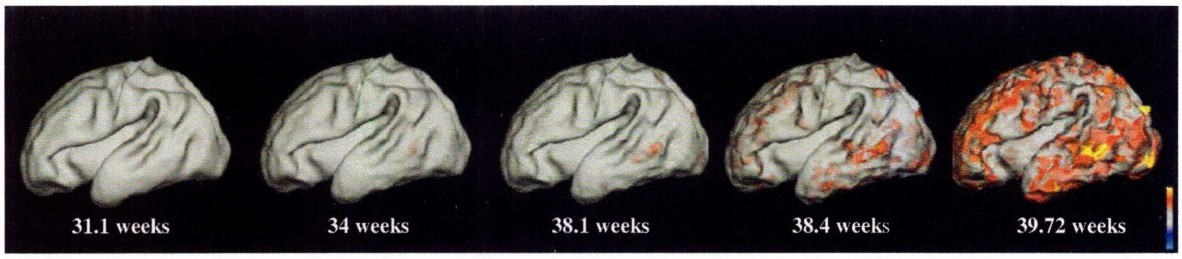

Figure 3-5: Reconstructed gray/white matter surfaces of neonates ordered with cGA using projected wavelet coefficients on the first principal component of wavelet coefficients at level 4.

3.3.2 Shape Variation in Neonates

The second dataset was from five normal neonates with corrected gestational ages (cGA) of 31.1, 34, 38.1, 38.4, and 39.72 weeks. T1 weighted 3D SPGR images were collected on a 1.5T scanner, with TR/TE = 30/8, flip angle = 25 to 30 degrees, matrix = 256×192, FOV = 220×165 mm or 200×150 mm and slice thickness 1.2 to 1.4 mm. Resultant DICOMS were manually segmented into white matter and cortical regions. Wavelet transformation and PCA are then applied to the reconstructed gray/white matter boundary to visualize the shape changes of cortical surface in neurodevelopment.

Using the wavelet transformation technique, the major cortical surface variations related to neurodevelopment in a small population of nenoates are identified to be in the middle spatial-frequency domain. PCA is used to study the specific modes of shape variations correlated with corrected gestational age.

PCA Results show that more than 98% of the shape variations are represented by the first three principal components at every frequency level. Projected surfaces are reconstructed to study the shape variations represented by each of the first three principal components at each frequency level separately, using equation 3.3. This time, the set of coefficients of the youngest subject (31.1 weeks gestational age) is used to fill in the other levels to build the whole set of projected coefficients $\tilde{\boldsymbol{\gamma}}^n = \left\{\boldsymbol{\gamma}^1_{-1},\ldots,\bar{\boldsymbol{\gamma}}_j + \mathbf{e}_j \times \bar{p}^n_j,\ldots,\boldsymbol{\gamma}^1_6\right\}$ at each level. As shown in Figure 3-5, the reconstructed surfaces (using wavelet coefficients projected on the first principal component) with age demonstrate the increasing folding of the gray/white matter boundary of the left hemisphere at level 4.

In this section, we presented the results of the proposed PCA based shape analysis in an aged normal population and a smaller newborn dataset. Although only results at a few lower frequency levels in the left hemisphere are shown in this section, the visualization method can be used to examine the most distinguished pattern of shape variations of both white/gray and gray/CSF surfaces for both hemisphere at all levels. However, caution should be used in interpreting these results because the shape changes are not entirely uncorrelated within neighbor regions, as discussed in Chapter 2.

3.4 Contributions

In this chapter, we introduced a new method to study shape variations of neuroanatomical structures using PCA and spherical wavelet transformation. Spherical wavelet transformations are demonstrated to accurately and efficiently detect the locations and spatial scales of shape variations. The use of principal component analysis on wavelet coefficients provides a novel way to detect and

visualize regional and multi-scale shape variation in a set of subjects.

In summary, the contributions of our work presented in this chapter are the following:

1) To our knowledge, this approach is the first one that has been proposed to study the major patterns of cortical folding variations at multiple spatial scales in localized cortical regions.

2) We developed tools for visualizing regional shape variations in a dataset at different spatial scales by reconstructing surfaces using wavelet coefficients projected onto a set of major principal components.

3) We also investigated the relationship of cortical folding variations with other variables such as age, gender and a set of neuropsychological test scores using multiple linear regression.

Application of this method in the cortical shape study shows promising results regarding the specific locations and spatial scales of cortical folding changes related to nondemented aging and neurodevelopment. This proposed method has also been successfully used to build shape models for guiding the segmentation of subcortical structures, such as the hippocampus, as described in Chapter 6.

A preliminary version of this work was presented at the *IEEE Computer Society Workshop on Mathematical Methods in Biomedical Image Analysis* in conjunction with *IEEE Computer Society Conference on Computer Vision and Pattern Recognition*[16]. A journal version of this work was published in *IEEE Transactions on Medical Imaging* [12].

Bibliography

[1] P. Bailey and G. von Bonin, *The isocortex of man*: Urbana: Univeristy of Illinois, 1951.

[2] Stensaas S.S., Eddington D.K., and W. H. Dobelle, "The topography and variability of the primary visual cortex in man.," *J Neurosurg*, vol. 40, pp. 747-755, 1974.

[3] H. Steinmetz, G. Furst, and H. J. Freund, "Variation of perisylvian and calcarine anatomic landmarks within stereotaxic proportional coordinates," *American Journal of Neuroradiology*, vol. 11, pp. 1123-1130, 1990.

[4] J. Rademacher, J. V. S. Caviness, H. Steinmetz, and A. M. Galaburda, "Topographical variation of the human primary cortices: Implications for neuroimaging, brain mapping, and neurobiology," *Cerebral Cortex*, vol. 3, pp. 313-329, 1993.

[5] G. Rajkowska and P. S. Goldman-Rakic, "Cytoarchitectonic definition of prefrontal areas in the normal human cortex: II. Variability in locations of areas 9 and 46," *Cerebral Cortex*, vol. 5, pp. 327-337, 1995.

[6] T. F. Cootes, C. J. Taylor, D. H. Cooper, and J. Graham, "Training Models of Shape from Sets of Examples," *Proc. British Machine Vision Conference, Springer-Verlag*, pp. 9-18, 1992.

[7] T. Cootes, C. Taylor, D. Cooper, and J. Graham, "Active shape models - their training and application," *Computer Vision and Image Understanding*, vol. 61, pp. 38-59, 1995.

[8] G. Szekely, A. Kelemen, C. Brechbuhler, and G. Gerig, "Segmentation of 2D and 3D objects from MRI volume data using constrained elastic deformations of flexible Fourier contour and surface models," *Medical Image Analysis*, vol. 1, pp. 19-34, 1996.

[9] M. E. Leventon, W. E. L. Grimson, and O. Faugeras, "Statistical Shape Influence in Geodesic Active Contours," *Proc. CVPR'2000*, pp. 316-323, 2000.

[10] D. Shen and C. Davatzikos, "An Adaptive-Focus Deformable Model Using Statistical and Geometric Information," *IEEE Transactions on Pattern Analysis and Machine Intelligence*, vol. 22, pp. 906-913, 2000.

[11] C. Davatzikos, X. Tao, and D. Shen, "Hierarchical active shape models, using the wavelet transform," *IEEE Trans. Medical Imaging*, vol. 22, pp. 414-423, 2003.

[12] P. Yu, P. E. Grant, Y. Qi, X. Han, F. Segonne, R. Pienaar, E. Busa, J. Pacheco, N. Makris, R. L. Buckner, P. Golland, and B. Fischl, "Cortical surface shape analysis based on spherical wavelets,," *IEEE Transaction on Medical Imaging*, vol. 26, pp. 582-598, 2007.

[13] D. Nain, S. Haker, A. Bobick, and A. Tannenbaum, "Multiscale 3d shape analysis using spherical wavelets," presented at MICCAI, Oct 26-29 2005.

[14] D. Nain, S. Haker, A. Bobbick, and A. Tannenbaum, "Shape-driven surface segmentation using spherical wavelets," presented at MICCAI, Oct 1-6, 2006.

[15] G. A. F. Seber and A. J. Lee, *Linear Regression Analysis*: Wiley-Interscience.

[16] P. Yu, X. Han, F. Segonne, R. L. Buckner, R. Pienaar, P. Golland, P. E. Grant, and B. Fischl, "Cortical surface shape analysis based on spherical wavelet transformation.," *Oral presentation in IEEE Computer Society Workshop on Mathematical Methods in Biomedical Image Analysis (MMBIA 2006), New York City, NY*, June 2006.

Chapter 4

Shape-based Classification

In this chapter, we study cortical folding differences between two groups of subjects based on the shape features extracted with spherical wavelet transformation in a classification framework. We employ a Bayesian classification method to train a classifier and select features by minimizing an estimate of prediction error. We develop tools to visualize the cortical folding differences corresponding to these selected features at multiple spatial scales and different locations. Applications of this shape-based classification approach to patient/control comparison studies bring out interesting results and achieve promising classification accuracy. This shape-based classification framework can be used to deepen our understanding of neurological diseases, and be used for early diagnosis and treatment assessment.

4.1 Motivation

There are two important and challenging problems in medical image analysis: 1) Extracting information about the morphological characteristics of neuroanatomical structures; 2) Detecting the group differences between normal people and diseased patients. Volume-based and image-based analyses have been widely used to conduct statistical study of the morphological changes of a variety of neuroanatomical structures, such as the cortex, the hippocampus, and the caudate. The study of differences between controls and patients with Schizophrenia, Alzheimer's disease, and epilepsy, has brought out novel neurological findings, and achieved promising group classification results[1-4]. With the recent advances in computer vision and medical imaging techniques, it is greatly desired to automatically and accurately localize the shape abnormalities of a brain structure of interest associated with a particular pathological condition. This type of shape analysis can not only provide new knowledge of the underlying biological mechanism associated with neurological diseases, but also be used for computer-aided diagnosis.

Shape-based classification consists of two major components: shape representation for extracting comparable shape features and pattern classification for learning a classifier based on those features. Different frameworks have been developed to extract shape features, detect the between-group

differences, and conduct classification for studying sub-cortical structures such as the hippocampus and the corpus callosum. One of the earliest shape studies of the hippocampus, by Csernanasky *et al.*, was based on shape features extracted from the volume deformation field [5]. By using Principle Component Analysis (PCA) and Linear Discriminant Analysis (LDA), they achieved 80% classification accuracy in discerning schizophrenic patients. Golland *et al.* and Timoner *et al.* conducted amygdala-hippocampus complex studies using distance transformation maps and displacement fields as shape descriptors [6-8]. By using Support Vector Machines (SVMs), a powerful and widely used classification method, they achieved 77% and 87% accuracies respectively in discriminating schizophrenic patients. Shen *et al.* classified the hippocampus in schizophrenia based on a boundary representation normalized across the subjects by using spherical harmonics transformation (SPHARM), and achieved approximately 70% accuracy using Fisher discriminant classifier [9]. This accuracy is further improved to 90% using SVMs [10]. Most recently, Li *et al.* used a surface mesh to represent the shape of the hippocampus, and studied the classification performance by subsampling the surface mesh at different resolutions [11]. On average, they achieved an above 80% classification accuracy using SVMs in classifying patients with Mild Cognition Impairment (MCI).

Due to the highly convoluted surface of the human cortex, statistical shape studies of the cortical surfaces have remained at the stage of detecting the localized cortical folding differences with group average comparison. It remains a challenge to develop an automated procedure for conducting discriminative analysis of the localized cortical folding abnormalities associated with pathological conditions in a classification framework. To tackle this problem, we develop a framework to use the shape features extracted by bi-orthogonal spherical wavelet transformation for conducting classification and detecting the shape differences of cortical surfaces between two groups of subjects [12]. In the following, we introduce the entire framework including preprocessing, feature selection, classification and a method for visualizing the localized and multi-scale shape differences corresponding to the selected shape features. We also demonstrate the application of this framework on both synthetic and real data.

4.2 Methods

In this shape-based classification framework, we use the normalized wavelet coefficients of coordinates of registered cortical surfaces as input shape features $\mathbf{x}^n = \left\{\gamma^n_{j,m}\right\}_{j=-1,..6,\ m\in M(j)}$ for each subject n, $n=1,...N$ in our training dataset. We use group labels $\mathbf{t} = \left\{t^n\right\}_{n=1}^N$, $t=\pm 1$ to indicate which class each subject belongs to. We conduct feature selection and classification based on the training data to obtain a classifier $\hat{\mathbf{w}}$, which can be used to classify new subjects following a decision rule such as

$$t^{new} = sign(\hat{\mathbf{w}}^T \mathbf{x}^{new}), \tag{4.1}$$

where $sign(y) = 1$ if $y >= 0$ and $sign(y) = -1$ if $y < 0$.

It is statistically challenging to classify cortical surfaces based on shape differences because of the large amount of shape features vs. the small amount of training data. As introduced in Chapter 2, we use about 491,526 wavelet coefficients to represent the convoluted cortical surfaces. However, the typical size of MRI datasets available in our group comparison study is less than 100. Given the large amount of input shape features and much smaller amount of training data, it is crucial to select shape features that best separate the groups and avoid overfitting to noise.

To solve these problems, we first utilize the compression property of wavelet representation to effectively reduce the dimension of input shape feature set. Secondly, we adopt a new Bayesian approach, predictive Automatic Relevance Determination (pred-ARD) [13], to jointly select shape features that are relevant to the discrimination and to train classifiers. For comparison, we also use one of the most powerful classification methods, support vector machines (SVMs), to classify the cortical surfaces, coupled with feature selection methods such as Hotelling's T^2 test [14].

In the following, we first introduce shape dimension reduction in the wavelet domain. We then describe the classification of cortical surfaces using pred-ARD and SVMs based on the bi-orthogonal wavelet transformation.

4.2.1 Feature Dimension Reduction in the Wavelet Domain

A – Spherical wavelet coefficients truncation

As described in Chapter 2, we use 163,842 wavelet coefficient vectors (with x, y and z components in each vector) to represent the cortical surface, where there are 12 vertices at level 0, 42 at level 1, 162 at level 2, and etc. As shown in Chapter 3, most of the pronounced cortical surface variations are represented at the lower frequency levels, while the highest frequency level (level 6) mostly consists of high-frequency noise. Therefore, we discard the wavelet coefficients at the highest two frequency levels in this classification framework.

To further reduce the dimension of the wavelet coefficients, we eliminate the coefficients that contribute the least to the wavelet power at each frequency level separately based on the training set. We first calculate the deviation $\mathbf{d}\boldsymbol{\gamma}^n_{j,m} = \left\| \boldsymbol{\gamma}^n_{j,m} - \bar{\boldsymbol{\gamma}}_{j,m} \right\|, m = 1,\ldots M(j)$ of each individual from the mean wavelet coefficient across all subjects in the training set $\bar{\boldsymbol{\gamma}}_{j,m} = \frac{1}{N}\sum_{n=1}^{N} \boldsymbol{\gamma}^n_{j,m}$, $\boldsymbol{\gamma}^n_{j,m} = \left\{ \gamma^{x^n}_{j,m}, \gamma^{y^n}_{j,m}, \gamma^{z^n}_{j,m} \right\}$, $m = 1,\ldots M(j)$ at the j^{th} level. We then calculate the contribution of each coefficient m at level j to the variation across population as $\mathbf{d}\boldsymbol{\gamma}_{j,m} = \frac{1}{N}\sum_{n=1}^{N} \mathbf{d}\boldsymbol{\gamma}^n_{j,m}$, $m = 1,\ldots M(j)$. To remove the wavelet coefficients that are least varied in the population, we rank the contribution of each coefficient $m = 1,\ldots M(j)$ at level j from the highest to the lowest and eliminate the coefficients whose cumulative contribution to the total variation $\mathbf{d}\boldsymbol{\gamma}_j = \frac{1}{M(j)}\sum_{m=1}^{M} \mathbf{d}\boldsymbol{\gamma}_{j,m}$ is less then 5%. As a result, we remove on average 15% of the total wavelet coefficients at frequency levels -1 to 5 for our datasets.

B – Feature selection by Hotelling's T^2 test

After eliminating the shape feature as introduced above, we still have about 40,000 wavelet coefficient vectors as input to the classification. In the group comparison study, we employ Hotelling's T^2 test to further reduce the dimension of shape features. The purpose is to pick out the spherical wavelet coefficient vectors that best separate the groups.

Hotelling's T^2 test is a multivariate analog to student's t test and can be used to test the equivalence of the means of two independent groups. The null hypothesis is that the mean column vector $\bar{\boldsymbol{\gamma}}^1_{j,m} = \frac{1}{N_1}\sum_{n=1}^{N_1} \boldsymbol{\gamma}^n_{j,m}$ of a coefficient calculated for group 1 with N_1 samples is equal to the mean vector

$\bar{\gamma}^2_{j,m} = \frac{1}{N_2}\sum_{n=1}^{N_2}\gamma^n_{j,m}$ of the same coefficients calculated for group 2 with a sample size N_2. Before we calduate the T^2 statistic, we first use Box-M test to compare the covariance matrices of these two groups. If the variability is similar, then we compute the T^2 statistic as

$$T^2 = \frac{N_1 \cdot N_2}{N_1 + N_2}(\bar{\gamma}^1_{j,m} - \bar{\gamma}^2_{j,m})^T (\hat{\Sigma}_W^{-1})(\bar{\gamma}^1_{j,m} - \bar{\gamma}^2_{j,m}), \tag{4.2}$$

where $\hat{\Sigma}_W = \frac{W_1 + W_2}{N_1 + N_2 - 1}$, and W_1 and W_2 are deviation SSCP (sums of squares and cross products) for two groups. If the variability is significantly different, then T^2 statistic is calculated as

$$T^2 = (\bar{\gamma}^1_{j,m} - \bar{\gamma}^2_{j,m})^T (\frac{S_1}{N_1} + \frac{S_2}{N_2})^{-1} (\bar{\gamma}^1_{j,m} - \bar{\gamma}^2_{j,m}), \tag{4.3}$$

where S_1 and S_2 are covariance matrices of the two groups. Then we compute an F-statistic as

$$F_{D,N_1+N_2-D-1} = \frac{N_1 + N_2 - (D+1)}{(N_1 + N_2 - 1)\cdot D} \cdot T^2, \tag{4.4}$$

where the lesser degree of freedom $df_1 = D = 3$ is the length of the coefficient vector and the greater degree of freedom is $df_2 = N_1 + N_2 - D - 1$. If the value of this statistic is greater than the tabulated F-distribution for a chosen significance level α, then we reject the hypothesis that the mean vectors of this coefficient in two populations are equal. In this work, we calculate the T^2 statistic for each wavelet coefficient vector based on the training set, and eliminate the coefficient vector with p value larger than the chosen significance level.

4.2.2 Classification Based on Predictive Automatic Relevance Determination

Pred-ARD is a hierarchical Bayesian approach that determines the relevance of input features based on their prediction performance. It extends the classical Bayesian feature selection method, Automatic Relevance Determination (ARD) [15, 16]. Both ARD and predictive ARD model the prior distribution of the parameters in the classifier $\mathbf{w}$ to explicitly represent the relevance of different input features. It is usually accomplished by assigning hyperparameters $\boldsymbol{\alpha}$ to determine the range of variation for the parameters relating to a particular input, as shown in Figure 4-1. Particularly, ARD method models the width of a zero-mean Gaussian prior on those parameters such as:

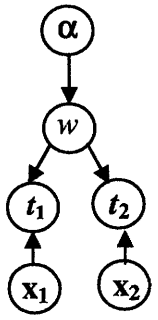

Figure 4-1: Hiearchical graphical model with hyperparameters

$$p(\mathbf{w} \mid \boldsymbol{\alpha}) = \prod_i N(w_i \mid 0, \alpha_i^{-1}). \tag{4.5}$$

In ARD, the hyperparameters are estimated to maximize the model evidence (marginal likelihood):

$$p(\mathbf{t} \mid \mathbf{X}, \alpha) = \int p(\mathbf{t} \mid \mathbf{X}, \mathbf{w}) p(\mathbf{w} \mid \alpha) d\mathbf{w}, \tag{4.6}$$

where $\mathbf{X} = \{\mathbf{x}^n\}_{n=1}^N$, and $\mathbf{t} = \{t^n\}_{n=1}^N$, $t = \pm 1$.

Pred-ARD method, proposed by Qi *et al.* [13] , assigns hyperparameters α in the same fashion, but estimates them to optimize the predictive performance

$$p(t_{new} \mid \mathbf{x}_{new}, \boldsymbol{\alpha}) = \int p(t_{new} \mid \mathbf{x}_{new}, \mathbf{w}) p(\mathbf{w} \mid \boldsymbol{\alpha}) d\mathbf{w}. \tag{4.7}$$

As a result, many elements of $\boldsymbol{\alpha}$ go to infinity, which naturally prunes irrelevant features in the data. Furthermore, Qi *et al.* [13] use Expectation Propagation (EP), a more accurate approximation method, for pred-ARD model estimation, and use the leave-one-out generalization error obtained directly from EP as estimates of predictive performance.

Using pred-ARD, we can not only select relevant features, but also learn the posterior distribution of classifier $p(\mathbf{w} \mid \mathbf{D}, \boldsymbol{\alpha})$ from training set $\mathbf{D} = \{(\mathbf{x}^1, t^1), \ldots, (\mathbf{x}^N, t^N)\}$. The posterior covariance matrix reveals correlations between selected features. Using these results, we can estimate the posterior predictive distribution of t^{new} for a new data point x^{new} as:

$$p(t^{new} \mid \mathbf{x}^{new}, \mathbf{t}) = \int p(t^{new} \mid \mathbf{x}^{new}, \mathbf{w}) p(\mathbf{w} \mid \mathbf{t}) d\mathbf{w} . \tag{4.8}$$

In two-class classification problem, the decision rule is:

$$t^{new} = \arg\max p(t^{new} \mid \mathbf{x}^{new}, \mathbf{t}) . \tag{4.9}$$

Furthermore, we can use the estimated predictive distribution to calculate probabilistic score of prediction confidence.

By using the pred-ARD method, we can effectively avoid the overfitting problem widely encountered in high-dimensional biological data classification problem. Pred-ARD avoids overfitting by modeling the uncertainty in the classifier by a probabilistic distribution, instead of using a point estimate. It further improves the generalization ability by maximizing the predictive performance, instead of the marginal likelihood used in ARD method. In addition, pred-ARD uses a sequential update for the hyperparameters, and therefore greatly speeds up the feature selection and the learning process.

In our work, we compare the performance of pred-ARD with SVMs on classifying cortical surfaces using on shape features extracted with bi-orthogonal spherical wavelet transformation.

4.2.3 Classification Based on Support Vector Machines

Support Vector Machines (SVMs) method was originally introduced by Vapnik in 1979, and has received extensive attention for its application in pattern recognition [17]. It can be applied to classification problems with high-dimensional data and small sample size.

Classification based on training SVMs involves finding a separating hyperplane that forms the largest margin between two classes of data while minimizing the classification error. Similar to pred-ARD, we denote the input feature of a set of N training data as $\mathbf{X} = \{\mathbf{x}^n\}_{n=1}^N$, and class label as $\mathbf{t} = \{t^n\}_{n=1}^N$, $t = \pm 1$. We define a hyperplane in the feature space using weight parameter vector $\mathbf{w}$, and offset parameter b. If the data is separable, the separating hyperplane ensures [18]

$$t^n (\mathbf{w}^t \mathbf{x}^n + b) \geq 1, \quad n = 1, \ldots, N . \tag{4.10}$$

Thus the goal is to find the weight vector that maximizes margin d with the constraint $\|\mathbf{w}\| \cdot d = 1$

$$\frac{t^n (\mathbf{w}^t \mathbf{x}^n + b)}{\|\mathbf{w}\|} \geq d, \quad n = 1, \ldots, N . \tag{4.11}$$

The weight vector $\mathbf{w}$ and offset d can be estimated by using Lagrange multipliers. The solution $\mathbf{w} = \sum_n \beta^n t^n \mathbf{x}^n$ $(\beta^n \geq 0)$ is a linear combination of the input data points for which equation 4.11 represents an equality. These data points are the closest to the separating plane and the most difficult patterns to classify. They are called *support vectors* since they define the boundary plane between classes. Thus the classifier is:

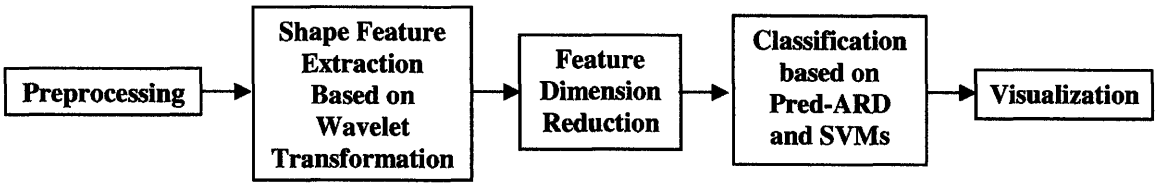

Figure 4-2: The automated procedure for conducting shape-based classification.

$$t^{new} = sign(\sum_{i=1}^{N_s} \beta^i t^i \langle \mathbf{x}^i, \mathbf{x}^{new} \rangle + b), \tag{4.12}$$

where N_s is the number of support vectors. This fundamental method has been extended to allow for different kernels and used for non-separable dataset by allowing misclassifications. We refer the reader to [17] for more details.

4.3 Experimental Setup and Dataset

In this work, we developed a framework to discriminate between two groups, usually one patient group and one control group, by using shape features of the cortical surfaces reconstructed from their MR images. Combined with the preprocessing tools available in the Fressurfer software package [19], the entire procedure, as shown in Figure 4-2, can be used to automatically process and conduct classification on large-scale MRI dataset, and visualize the shape differences of cortical surface between two groups of subjects.

A – Preprocessing

The cortical surfaces, including gray/white matter surfaces (hereinafter referred as white matter surfaces) and CSF/gray matter surfaces (hereinafter referred as pial surfaces) of these two groups are registered and normalized as described in Chapter 2, and spherical wavelet transformation is applied to the normalized coordinate functions (ref. Chapter 2). As a result, we acquire four sets of wavelet coefficients for each subject, including the wavelet coefficients for the white surfaces and pial surfaces of right and left hemispheres. We reduce the dimension of each set of wavelet coefficients based on training set using the criterion introduced in section 4.2.1. We then calculate the F-statistic for each wavelet coefficient vector in each of the reduced set based on Hotelling's T^2 test. We select a set of coefficient vectors from each surface feature set by thresholding the corresponding p value of the F-statistic, and conduct classification using both pred-ARD and SVMs.

As we introduced before, pred-ARD trains a Bayesian classifier and selects features by minimizing an estimate of prediction error. However, since we still have approximately 40,000 wavelet vectors (about 120,000 input features) left after reducing wavelet coefficients as introduced in 4.2.1, it takes a few days to finish one training task on a dataset with dozens of subjects. To shorten the computation time, we further reduce the input feature dimension by selecting coefficient vectors whose p value is smaller than a pre-selected threshold as inputs into pred-ARD based classification.

Similarly, we reduce the input feature dimension for classification based on SVMs by thresholding the p value calculated from the Hotelling's T^2 test of each wavelet coefficient vector. In this work, we allow soft margin separation and employ linear, Gaussian radial basis function and polynomial kernels. By using linear kernel and setting the weighting parameter of the classification error term to 1, we obtain the best cross validation results in our experiments.

B – Dataset

To test the shape-based classification procedure, we first generate a synthetic shape difference in half of the 84 normal brain scans used for normal shape variation study in Chapter 3. We then apply the classification procedure to three different real dataset to compare pred-ARD to SVMs coupled with Hotelling T^2 test.

The first dataset consists of 11 children (4 female, right-handed, average age 11.83) and 12 young adults (7 female, right-handed, average age 22.17) recruited as normal controls for a functional MRI study on dyslexia. All subjects were right-handed, with no history of speech, language, or reading disorders. Each subject underwent a T1-weighted MRI (Siemens MP-RAGE) of the entire brain at 1.3 mm $\times$ 1.0 mm $\times$ 1.0 mm resolution with MRI parameters of TR = 6.6 ms, TE = 2.9 ms, TI = 300 ms, flip angle = 8 degrees, and two averages per scan.

The second data is acquired at the Washington University Alzheimer's Disease Research Center for 23 normal male subjects with an average age of 78.5 ± 5.7, and 37 male subjects with mild dementia (CDR score =0.5), and an average age of 78.5 ± 5.8. Clinical Dementia Rating (CDR) is a numeric scale used to quantify the severity of symptoms of dementia. Structural Magnetic Resonance Imaging (MRI) was performed on a Siemens 1.5 T Vision System (Erlangen, Germany). Between 2 and 4 high-resolution (1mm$\times$1mm$\times$1.25 mm) T1-weighted MP-RAGE scans were acquired per participant (TR = 9.7 ms, TE = 4 ms, flip angle = 10, TI = 20 ms, TD = 200 ms). Scans were motion corrected and averaged, yielding a single image volume with high contrast-to-noise ratio, enabling quantitative characterization. All MRI scans were conducted within 6 months of neuropsychological testing and experiments.

The third dataset consists of 52 normal male subjects (ages 34.5 ± 11.6) and 72 chronic schizophrenic male patients (ages 36.4 ± 10.5). The normal subjects were screened to exclude those with a personal history of mental illness, neurological disorder and a family history of a psychotic disorder. T1 weighted images of these subjects were acquired in a 3 Tesla Siemens System using a spoiled grass sequence with the following parameters: 1.5 mm coronal slices, 20 degree flip angle, 12 msec TR, 5 ms TE, 3 NEX, 16$\times$16 cm FOV and a 256$\times$256 matrix. Phase and magnitude field maps were acquired and used for image distortion correction.

C – Visualization and cross validation

By using Pred-ARD method, we select a set of features that are most relevant to the discrimination of one group from another. To visualize these selected features, we gradually add the differences of the mean values of selected coefficients between group 1 and group 2 to the mean wavelet coefficients of Group 1, and inversely transform the resulting new sets of coefficients to generate synthetic surfaces. By deforming the generated synthetic surfaces from group 1 to group 2, we can visualize these localized shape differences at multiple spatial scales corresponding to the selected features.

Lastly, we calculate the average leave-one-out classification accuracy to quantitatively compare the generalization error based on pred-ARD and SVMs. Each time, we reduce the feature dimension

in the wavelet domain, and then conduct the Hotelling's T^2 test using N-1 subjects as training set. Using the reduced wavelet coefficients of the training set, we estimate a classifier based on pred-ARD or SVMs method, and classify the left-out subject using the resulting classifier. Finally, the leave-one-out classification accuracy is calculated as the percentage of subjects correctly classified by selecting features and training a classifier using the remaining subjects.

4.4 Results and Discussions

4.4.1 Shape Discrimination of Synthetic Data

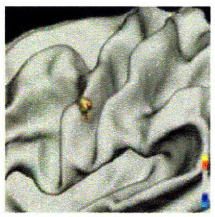

Figure 4-3: Statistical map of selected coefficients shown on average deformed surface

The shape-based classification framework is tested on 84 normal brain scans, with half of them having a synthetic 4mm by 2mm bump around a point selected on the bank of central sulcus. Hotelling's T^2 test shows that only coefficients located around the synthetic deformation have a calculated p value lower than 0.0002 (Figure 4-3). Using these coefficients, the synthetic deformation can be visualized with accurate location and spatial extension. With the same threshold, the leave-one-out classification accuracy based on SVMs is 95.24%. This accuracy decreases to 85.71% with a threshold of 0.01, which we believe is due to an increased false detection rate caused by a lack of multiple comparisons correction (the large number of features, and therefore the large number of statistical tests involved, increases the chance of incorrect detection).

4.4.2 Shape Discrimination of Patients with Mild Dementia

In this experiment, we conduct a study on the differentiation between normal male controls and male patients with mild dementia (CDR=0.5) using pred-ARD classification method. Since the patients are individuals with Dementia of the Alzheimer Type (DAT) at very mild-to-mild stages, detecting cortical shape changes in these patients is challenging. However, once we are able to extract reliable shape features for differentiating the patients, we might be able to detect the Alzheimer's disease at an early stage when intervention may be most effective.

In this study, we first compare classification accuracy by using different combination of hemispheres (left and right), surfaces (white and pial), and thresholds used for filtering the input shape features based on Hotelling's T^2 test. As a result, we find there are no significant shape changes in the pial surfaces of the DAT patients compared with the controls. This is probably due to the imperfections in the reconstructed pial surfaces. White surface of the right hemisphere has stronger discriminative power than that of the left hemisphere. The combination of both left and right hemispheres generates the best leave-one-out classification accuracy. We also find that selecting wavelet coefficients with a p value less than 0.02 gives the best discriminative results. By using this threshold, the input feature is sized down to around 1500 on each side. Among them, about 150 features (10%) are selected by pred-ARD to be the most relevant features to our discriminative task.

To visualize the result, we can generate movie deforming the average surface of controls to the average surface of DAT patients using differences found in these selected features, as detailed in Section 4.3. We illustrate these results in this thesis by showing the synthetic surfaces generated for DAT group at several frequency levels in Figure 4-4. Significant shape differences are observed at both low and high spatial-frequency levels in this study. Specifically, on the left hemisphere, the shape changes are most salient at the low frequency level in the frontal lobe. At higher frequency

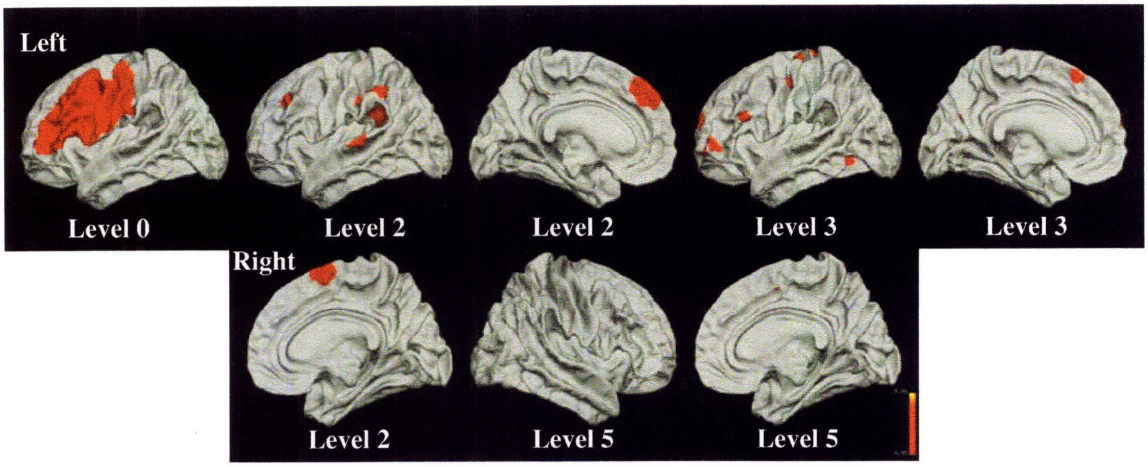

Figure 4-4: The regions that are most discriminative between controls and patients with mild Dementia highlighted on the average partient cortical surface. The regions correspond to the spherical wavelet coefficients that are selected by pred-ARD method. The colormap encodes the p value of these selected wavelet coefficients in the support region of the corresponding bi-orthogonal spherical wavelet basis function.

levels, there are dispersed variations scattered across the brain on both hemispheres (Figure 4-4). To validate that these detected regions are indeed affected by DAT, we compare these shape changes with the normal shape variations we discovered in the elderly population in Chapter 3. As a result, we find there are overlapped regions of changes at some frequency levels, as demonstrated in Figure 3-4 and 4-4 at level 0, for example. However, further visualization shows that the pattern of shape variations detected are different in these two studies. This result verifies that the shape changes detected in the DAT dataset is not due to idiosyncratic shape variations.

Lastly, we conduct leave-one-out cross validation using coefficients selected with threshold=0.02. As a result, we obtain a classification accuracy of 75%, with a sensitivity of 83.78% and a specificity of 60.87%. This result proves that our classification method has promising generalization ability, and can be potentially used for early diagnosis of Alzheimer's disease.

4.4.3 Comparison of Pred-ARD and SVMs

At last, we compared the performance of pred-ARD and SVMs in discriminating cortical surfaces using spherical wavelets on several datasets. Since the SVMs-based classification method we used in this work does not include feature selection, we filter the input wavelet coefficient vectors using different threshold based on p value calculated for each coefficient vector using Hotelling's T^2 test.

After comparing classification accuracies of SVMs with different combination of hemispheres, surfaces, and thresholds, which are used for filtering the input shape features based on Hotelling's T^2 test, we find consistent results that white matter surface generates better classification results than the pial surface with other parameters being equivalent. In contrast to the stronger discriminative power found for the right hemisphere in pred-ARD, we always achieve better classification results using left hemisphere in these 3 datasets we studied based on SVMs method. Lastly, we find smaller threshold in selecting the input features gives better leave-one-out classification accuracy.

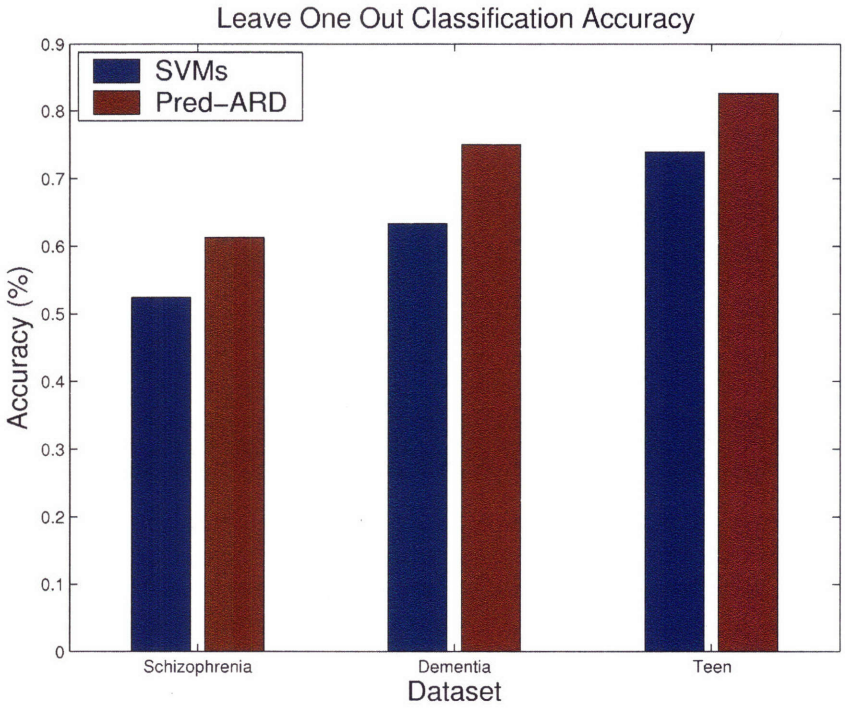

Figure 4-5: Comparison of leave-one-out classification accuracy by using pred-ARD and SVMs in three different studies. Both left and right hemispheres are used for pre-ARD, and the input shape features are pre-selected using Hotelling's T^2 test. Only left hemisphere is used for SVMs, and the input shape features are selected with Hotelling's T^2 test using a smaller threshold.

Figure 4-5 demonstrates the best classification results generated with pred-ARD and SVMs for these three studies. Both left and right hemisphere are used for pred-ARD based classification with input features pruned in the wavelet domain and then pre-selected based on Hotelling's T^2 test. The thresholds are chosen for each dataset based on cross-validation results. Left hemisphere is used for SVM based classification with a smaller threshold. In all three cases, pred-ARD out-performs SVMs in leave-one-out classification accuracy. However, the cross-validation result in the schizophrenia study showed that neither method can successfully separate the patients from normal controls.

These results demonstrate the advantages of pred-ARD method over the SVMs method coupled with Hotelling's T^2 test in shape feature selection. As a wrapper method, pred-ARD couples the task of feature selection with classification. On the contrary, since SVMs-based classification method does not include feature selection, features selected using Hotelling's T^2 test (or any other filter methods) are independent of the classification task. Secondly, pred-ARD provides a score, based on the estimated leave-one-out prediction error, for the joint selection of feature subsets, while the Hotelling's T^2 test picks out each feature individually without considering the influence of other features.

4.5 Contributions

In this chapter, we studied shape differences between two groups of subjects in a classification framework based on the shape features extracted from bi-orthogonal spherical wavelet

transformation. In summary, the contributions of our work presented in this chapter are the following:

1) To the best of our knowledge, this approach is the first one that has been proposed to detect localized and multi-scale cortical shape differences between two groups in a classification framework.

2) We employed a Bayesian classification method that is particularly suitable for large dimensional biological dataset, as is the case for our data in which we have hundreds of thousands of potential features, and only dozens of subjects.

3) We investigated the cortical shape differences at different spatial scales in several group comparison studies, including mild dementia, schizophrenia and teenage/adult studies. We developed tools to visualize the most discriminative shape differences between two groups at multiple spatial resolutions.

Application of this shape-based classification approach to MD/control dataset has achieved promising classification accuracy, and showed interesting results regarding the specific location and spatial scales of cortical shape variations related to neurological diseases. The developed framework can be used to detect shape variations of other brain structures as well. The detected shape differences can potentially improve our understanding of neurological diseases, and be used for early diagnosis and treatment assessment.

A preliminary version of part of this work was presented in the *International Conference on Pattern Recognition* [12].

Bibliography

[1] R. M. Bilder, H. Wu, B. Bogerts, Manzar Ashtaric, D. Robinson, M. Woerner, J. A. Lieberman, and G. Degreef, "Cerebral volume asymmetries in schizophrenia and mood disorders: a quantitative magnetic resonance imaging study," *International Journal of Psychophysiology*, vol. 34, pp. 197-205, 1999.

[2] P. A. Freeborough and N. C. Fox, "MR image texture analysis applied to the diagnosis and tracking ofAlzheimerapos;s disease," *IEEE Transactions on Medical Imaging*, vol. 17, pp. 475 - 478, 1998.

[3] Y. Liu, L. Teverovskiy, O. Carmichael, R. Kikinis, M. Shenton, C.S. Carter, V.A. Stenger, S. Davis, H. Aizenstein, J. Becker, O. Lopez, and C. Meltzer, "Discriminative MR image feature analysis for automatic schizophrenia and Alzheimer's Disease classification," *Proceedings of the 7th International Conference on MedicalImage Computing and Computer Aided Intervention (MICCAI '04),*, pp. 393 - 401, 2004.

[4] K. S.-Z. Jafari-Khouzani, H.; Elisevich, K.:, "Hippocampus volume and texture analysis for temporal lobe epilepsy," *Proceeding of IEEE International Conference on Electro/information Technology*, pp. 394 - 397, 2006.

[5] Csernansky J. G. and e. al., "Hippocampal morphometry in schizophrenia by high dimensional brain mapping," *Proc. Nat. Acad. of Science*, vol. 95, pp. 11406-11411, 1998.

[6] P. Golland, W. E. L. Grimson, M. E. Shenton, and R. Kikinis, "Small Sample Size: Learning for Shape Analysis of Anatomical Structures," *Proc. MICCAI'2000, LNCS*, vol. 1935, pp. 72-82, 2000.

[7] P. Golland, B. Fischl, M. Spiridon, N. Kanwisher, R. L. Buckner, M. E. Shenton, R. Kikinis, A. M. Dale, and W. E. L. Grimson, "Discriminative analysis for image-based studies," *MICCAI*, vol. 1, pp. 508-515, 2002.

[8] S. J. Timoner, P. Golland, W. E. L. Grimson, R. Kikinis, and W. M. Wells, "Performance issues in shape classification," *Proceeding of MICCA*, pp. 355-362, 2002.

[9] L. Shen, J. Ford, F. Makedon, and A. Saykin, "hippocampal shape analysis surface-based representation and classification," *SPIE Medical Imaging*, 2003.

[10] L. Shen, J. Ford, F. Makedon, and A. J. Saykin, "A surface-based approach for classification of 3D neuroanatomic structures," *Intell. Data Anal.*, vol. 8, pp. 519-542, 2004.

[11] S. Li, F. Shi, F. Pu, X. Li, T. Jiang, S. Xie, and Y. Wang, "Hippocampal shape analysis of Alzheimer disease based on machine learning methods," *American Journal of Neuroradiology*, vol. 28, pp. 1339-1345, 2007.

[12] P. Yu, X. Han, F. Segonne, A. K. Liu, R. A. Poldrack, P. Golland, and B. Fischl, "Shape-based discrimination and classification of cortical surface.," *Oral Presentation in International Conference on Pattern Recognition 2006, Hong Kong, P.R.China*, Aug. 2006.

[13] Y. Qi, T. P. Minka, R. W. Picard, and Z. Ghahramani, "Predictive automatic relevance determination by expectation propagation," *Proceedings of Twenty-first International Conference on Machine Learning*, 2004.

[14] D. F. Morrison, *Multivariate Statistical Methods*: McGraw-Hill, 1990.

[15] D. J. MacKay, "Bayesian interpolation," *Neural Computation*, vol. 4, pp. 415-417, 1992.

[16] R. M. Neal, *Bayesian learning for neural networks*. New York: Springer, 1996.

[17] V. Vapnik, *Estimation of Dependences Based on Empirical Data*. Nauka, Moscow, 1979.

[18] C. J. Burges, C., "A Tutorial on Support Vector Machines for Pattern Recognition," *Data mining and Knowledge Discovery*, vol. 2, pp. 121-1677, 1998.

[19] "http://surfer.nmr.mgh.harvard.edu."

Chapter 5

Cortical Folding Development Models

In this chapter, we develop a nonlinear temporal model of the cortical folding development in the late gestation based on a MRI dataset of newborn. We employ a regularization framework to improve the generalization performance due to the limited amount of training data available in this study. We employ a quasi-Newton method based on BFGS approximation to estimate this regularized folding development model. We estimate the nonlinear models in the spherical wavelet domain to study the folding development of cortical folds of different spatial scales. These models provide quantitative and innovative information regarding temporal order and regional differentiation of cortical folding development. These normal development models can be used as biomarkers for the early diagnosis of neurological deficits in newborns.

5.1 Motivation

The human cortex is highly convoluted, in contrast to the smooth cortex found in other animals such as mice and rats. In human beings, cortical development begins prenatally, and the majority of neurons are generated before birth. The development of cortical folding starts at about 9 weeks in gestation, changes dramatically until birth, but continues into late adolescence [1, 2].

The mechanism involved in the regulated formation of folding pattern remains unclear. It is hypothesized that folding pattern formation is caused by neuron differentiation, migration and the growth of neutrite. Another theory suggests that differential growth of the outer layers relative to inner layers of the cortex results in cortical buckling [3]. A third theory proposed that the mechanical tension generated during the "long-distance" connections of different regions of the brain leads to the formation of folding [4]. Regional and hemispheric differences of folding development have been reported in the previous study. There is also the notion that large scale cortical folds develop earlier, and the secondary and tertiary folds develop later [1]. However, because of the lack of *in vivo* data, the cortical folding development process has not been quantitatively and thoroughly studied in the previous work.

It is of great medical importance to study the folding formation process. This study can not only provide knowledge about structure-function relationship, but only deepen our understanding of neurological diseases originated from the abnormal structural and /or functional connectivity in neurodevelopment, such as Schizophrenia and Autism. In this work, we have been able to study a

Magnetic Resonance Imaging (MRI) dataset of premature newborns that were scanned right after they were born. Because these healthy newborns have different gestational ages, we can use this dataset to study, for the first time, the normal cortical folding development process *in vivo*.

Like many growth phenomena in nature, the folding of the human cortex starts slowly, and accelerates before slowing down to approach a limit. Therefore, we propose to model the folding development of the gray/white boundary at different spatial scales using a growth model [5]. Unlike Principal Component Analysis (PCA) introduced in Chapter 3, which is a linear data model, the growth model is a nonlinear temporal one that captures both the fast growth and saturation phases of cortical folding development in late gestation. Furthermore, we propose to build the folding development models in the spherical wavelet domain in order to study the temporal orders and regional differences in folding development.

In this chapter we introduce the details of this nonlinear cortical folding development model, the regularization scheme employed to improve the predictive performance, and the model estimation methods. We also present the use of this model in detecting the spatial scales and regional differences of the cortical folding development of the gray/white matter boundary in this dataset of newborn.

5.2 Dataset and Methods

5.2.1 Dataset and Preprocessing

In this study, we use a set of eleven MRI scans acquired on eight normal neonates with corrected gestational ages (cGA) of 30.57, 31.1, 34, 37.71, 38.1, 38.4, 39.72, and 40.43 weeks, and 3 children who were approximately 2, 3 and 7 years old at the time of scanning. T1 weighted 3D SPGR images were collected on a 1.5T scanner, with TR/TE = 30/8, flip angle = 25-30°, matrix = 256×192, FOV = 220×165 mm or 200×150 mm and slice thickness 1.2 to 1.4 mm.

The images of newborns were manually segmented into white matter and cortical regions due to inverted gray/white contrast and low contrast of the gray/white matter boundary. Based on the manual segmentation, the cortical surfaces are reconstructed using Freesurfer tools as described in Chapter 2. The children dataset was preprocessed using the automated tools. The reconstructed cortical surfaces of these 11 subjects were registered and normalized as described in Chapter 2. Wavelet transformation and the developed nonlinear models are then applied to the normalized white matter surfaces (gray/white matter boundary) to study the folding development of cortical surface. To be compared with neonates, children's ages were converted to 167, 235, and 451 weeks by assuming a 40 week gestation period.

5.2.2 Nonlinear Cortical Folding Development Model

To model the cortical folding development of cortical surfaces in this dataset from late gestation to early infancy, we fit a growth model, more exactly, the Gompertz function [6], to the spherical wavelet coefficients. Given a limited amount of training data currently available for this study, which includes 8 newborns and 3 children, we employ a regularization framework to avoid overfitting and improve prediction performance on new data points. We use an efficient method to estimate this regularized Gompertz model based on BFGS approximation [7] and estimate the confidence intervals of estimated parameters using Laplacian Approximation.

A – Regularized Gompertz model and estimation

Specifically, if $w(t_i)$ is one of the spherical wavelet features extracted from a subject at age t_i, we use the Gompertz curve [6] to model the change of this feature at different ages as follows:

$$w(t) = g_1 \exp(-\exp(-g_2(t_i - g_3))) + \varepsilon(t_i),, \tag{5.1}$$

where g_1 is the maximum value at mature, g_2 is the growth rate that quantifies the speed of the folding development, g_3 is at the inflexion point and indicates the age of the fastest folding development, and $\varepsilon(t_i)$ represents additive noise with mean zero.

Due to the limited number of subjects available in this study, we apply a regularization framework for parameter estimation to avoid overfitting. In such a framework, we minimize a cost function over variables g_1, g_2 and g_3:

$$Q(g_1,g_2,g_3) = \sum_{i=1}^{N}(g_1 \exp(-\exp(-g_2(t_i - g_3))) - w(t_i))^2 + c\sum_{j=1}^{3} g_j^2, \tag{5.2}$$

where the first term on the right hand side of equation 5.2 models the empirical error of model fitting, and the second term is a scaled l_2-norm regularizer with the scaling factor c controlling the trade-off between the empirical error and the degree of regularization. Having the weighted sum of the squared parameters in the cost function, in addition to the empirical mean square error, constrains the model space and avoids overfitting to data noise. This method is a special form of regularization, which is known as weight decay in statistical learning theory [8].

To minimize the cost function Q, we first compute its gradient, which has the closed form:

$$\frac{dQ}{dg_1} = 2\sum_{i=1}^{N}(g_1 \exp(-\exp(-g_2(t_i - g_3))) - w(t_i))\exp(-\exp(-g_2(t_i - g_3))) + 2cg_1 \tag{5.3}$$

$$\frac{dQ}{dg_2} = 2\sum_{i=1}^{N}(g_1 \exp(-\exp(-g_2(t_i - g_3))) - w(t_i))\exp(-g_2(t_i - g_3))g_1 \exp(-\exp(-g_2(t_i - g_3)))(t_i - g_3) + 2cg_2$$

$$\frac{dQ}{dg_3} = -2\sum_{i=1}^{N}(g_1 \exp(-\exp(-g_2(t_i - g_3))) - w(t_i))\exp(-g_2(t_i - g_3))g_1 \exp(-\exp(-g_2(t_i - g_3)))(g_2) + 2cg_3$$

Since a simple gradient method suffers from slow convergence, we adopt a quasi-Newton method based on the Broyden-Fletcher-Goldfarb-Shannon (BFGS) approximation [7] of the Hessian matrix. The BFGS method enables us to efficiently minimize Q over the parameters $\{g_i\}_{i=1,\ldots 3}$. We tune the regularization parameter c based on the leave-one-out cross-validation. Specifically, we compute the mean square error of our predictions on the held-out data point using the model parameters optimized from the rest of the training data. From a collection of pre-specified values, we select the parameter c that minimizes the leave-one-out error.

B – Confidence interval

Furthermore, we estimate the Bayesian confidence intervals of our estimated parameters $\mathbf{g} = \{g_i\}_{i=1,\ldots 3}$. Note that using the regularized cost function (equation 5.2) is equivalent to using a Bayesian model; if we scale equation 5.2 by the observation noise variance (assuming it is known), then the log likelihood function $\log p(\mathbf{w} \mid \mathbf{g}, \mathbf{t})$, $\mathbf{w} = \{w_i\}_{i=1,\ldots N}, \mathbf{g} = \{g_i\}_{i=1,\ldots 3}, \mathbf{t} = \{t_i\}_{i=1,\ldots N}$ in the Bayesian model corresponds to the first term on the right hand side of equation 5.2 up to a normalization constant, and the Gaussian prior distribution $p(\mathbf{g})$ corresponds to the second term on

the right hand side of equation 5.2 up to a normalization constant. Therefore, minimizing equation 5.2 amounts to finding the maximal value of the posterior distribution $p(\mathbf{g} \mid \mathbf{w}, \mathbf{t})$.

Although we can efficiently compute the parameters $\hat{\mathbf{g}}$ that maximize the posterior distribution, it is computationally intractable to calculate the exact distribution $p(\mathbf{g} \mid \mathbf{w}, \mathbf{t})$ because the likelihood function is non-Gaussian in $\mathbf{g}$. Therefore, we use Laplace's approximation [9] to approximate the exact posterior distribution as a Gaussian:

$$p(\mathbf{g} \mid \mathbf{w}, \mathbf{t}) \approx p(\hat{\mathbf{g}} \mid \mathbf{w}, \mathbf{t}) \exp(\frac{1}{2}(\mathbf{g} - \hat{\mathbf{g}})^T \mathbf{H} (\mathbf{g} - \hat{\mathbf{g}})) \tag{5.4}$$

where $\mathbf{H}$ is the Hessian matrix:

$$\mathbf{H} = \frac{d^2 \log(p(\mathbf{g} \mid \mathbf{w}, \mathbf{t}))}{d\mathbf{g} d\mathbf{g}^T}\Big|_{\mathbf{g}=\hat{\mathbf{g}}} = -\frac{1}{2\sigma_w^2} \frac{d^2 Q(\mathbf{g}))}{d\mathbf{g} d\mathbf{g}^T}\Big|_{\mathbf{g}=\hat{\mathbf{g}}} \tag{5.5}$$

Once we have computed the Hessian matrix, the variance matrix of the posterior distribution $p(\mathbf{g} \mid \mathbf{w}, \mathbf{t})$ can be approximated as $-\mathbf{H}^{-1}$. Thus the 90% Bayesian confidence intervals of the estimated parameters are obtained by $\{\hat{g}_i \pm 1.64\sigma_i\}_{i=1,..3}$, where $\{\sigma_i\}_{i=1,..3}$ are the diagonal components of the approximate variance matrix.

C – Goodness of fit

The regularized folding development model is applied to study the development of cortical folding in newborns based on spherical wavelets. To measure the goodness-of-fit of the model, we calculate the R^2 statistic, the ratio of the sum of squares explained by the model and the total sum of squares around the mean:

$$R^2 = 1 - \frac{\sum_{i=1}^{N} (w(t_i) - \hat{w}(t_i))^2}{\sum_{i=1}^{N} (w(t_i) - \frac{1}{N}\sum_{i=1}^{N} w(t_i))^2}. \tag{5.6}$$

D – Comparison with linear model

To validate that the proposed nonlinear model is suitable to characterizing the dynamic development of folding, we compare it with the linear regression model:

$$\begin{aligned} w &= x\boldsymbol{\beta} + \varepsilon = at + b + \varepsilon, \\ x &= [t,1]^T, \varepsilon = N(0,\sigma^2), \end{aligned} \tag{5.7}$$

where $N(0,\sigma^2)$ denotes a normal distribution with mean 0 and variance σ^2. The parameter vector can be estimated as:

$$\hat{\boldsymbol{\beta}} = (\mathbf{x}^T\mathbf{x} + vI)\mathbf{x}^T\mathbf{w}, \tag{5.8}$$

where $\mathbf{w} = \{w_i\}_{i=1}^N, \mathbf{x} = \{x_i\}_{i=1}^N$, and parameter v is the weight of the regularization term, similar to the constant used in equation 5.2. We assign a large value to v to avoid overfitting.

To compare our nonlinear folding development model (denoted as M_g) with the linear model (M_l), we compute the marginal data likelihood using both models, where $D = \{(w(t_i), t_i)\}_{i=1}^{11}$:

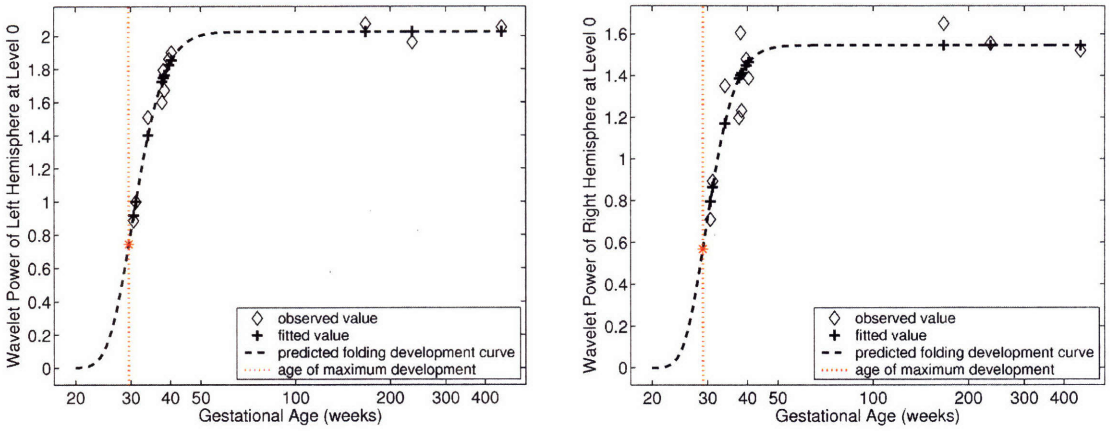

a) b)

Figure 5-1: a) The predicted curve at level 0 in the left hemispheres. b) The predicted curve at level 0 in the right hemispheres (A logarithmic scale (base 10) is used for the horizontal axis from 0 to 450 weeks to include all the 11 data points used in the model fitting; vertical axis is the wavelet power normalized with regard to the wavelet basis function.)

$$M_g: \qquad P(D \mid M_g) = \int p(\mathbf{w}, \mathbf{t} \mid \mathbf{g}) p(\mathbf{g}) d\mathbf{g} \,, \tag{5.9}$$

$$M_l: \qquad P(D \mid M_l) = \int p(\mathbf{w}, \mathbf{t} \mid \boldsymbol{\beta}) p(\boldsymbol{\beta}) d\boldsymbol{\beta} \,, \tag{5.10}$$

and select the model with larger marginal likelihood.

The marginal likelihood of nonlinear model is calculated with Laplace's approximation as [9]

$$P(D \mid M_g) = \int p(\mathbf{w}, \mathbf{t} \mid \mathbf{g}) p(\mathbf{g}) d\mathbf{g} \approx p(\mathbf{w} \mid \hat{\mathbf{g}}, \mathbf{t}) p(\hat{\mathbf{g}}) (2\pi)^{rows(\mathbf{H})/2} \left| -\mathbf{H} \right|^{-1/2}, \tag{5.11}$$

where the Hessian matrix is calculated with equation 5.5. For the linear model, we assume the parameter $\boldsymbol{\beta}$ has a conjugate prior distribution as an inverse Wishart distribution $W^{-1}(S_0, n)$, where S_0 is set to nI, and $n = 2$, as detailed in [10]. Then the marginal likelihood can be calculated by a matrix-t distribution [10, 11]:

$$P(D \mid M_l) \sim T(\hat{\mathbf{w}}, S_0, I - \mathbf{x}^T S_{\mathbf{xx}}^{-1} \mathbf{x}, N) \,, \tag{5.12}$$

where $\hat{\mathbf{w}} = \mathbf{x}\hat{\boldsymbol{\beta}}$, $S_{\mathbf{xx}} = \mathbf{x}^T \mathbf{x}$, and $N = 2 + 11$, the sum of the number of parameters and the number of data points.

In the next section, we estimate the proposed folding development models using bi-orthogonal spherical wavelet coefficients. We report the estimated parameters, 90% confidence interval, and R^2 statistics of the proposed nonlinear folding development model at different frequency levels. We also show the estimated folding development curves at different frequency levels overlaid on the original data. These results demonstrate the effectiveness of the proposed model for describing cortical folding development.

5.3 Results and Discussions

5.3.1 Global Folding Development of the Cortical Surface

In this section we describe the results of using the nonlinear cortical folding development model to

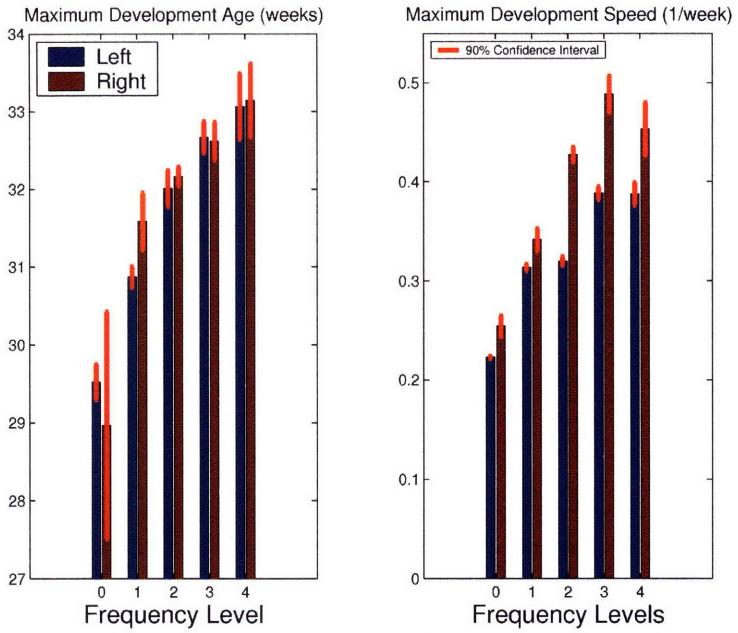

Figure 5-2: Estimated age of maximum folding development (on the left) increases with frequency levels in both left and right hemispheres, maximum development speed increases as well (shown on the right). Red line indicates 90% confidence interval.

Table 2.1

Model estimation results using the wavelet power at different frequency levels for both left and right hemispheres

	Level	g_1	Development Speed (1/week)	Maximum Development Age (week)	R^2
Left	0	2.03 ± 0.20	0.22 ± 9.3e-4	29.52 ± 0.221	0.82
	1	2.27e-1 ± 1.59e-2	0.31 ± 3.1e-3	30.87 ± 0.128	0.81
	2	2.78e-2 ± 1.90e-3	0.32 ± 4.2e-3	32.01 ± 0.229	0.78
	3	1.87e-3 ± 3.20e-5	0.39 ± 6.2e-3	32.67 ± 0.201	0.81
	4	8.70e-5 ± 1.00e-6	0.39 ± 1.1e-2	33.06 ± 0.417	0.75
Right	0	1.55 ± 0.72	0.25 ± 1.0e-2	28.97 ± 1.453	0.57
	1	2.33e-1 ± 5.91e-2	0.34 ± 1.1e-2	31.59 ± 0.364	0.70
	2	2.67e-2 ± 1.10e-3	0.43 ± 7.0e-3	32.16 ± 0.119	0.83
	3	1.83e-3 ± 3.70e-5	0.49 ± 1.8e-2	32.62 ± 0.239	0.78
	4	8.60e-5 ± 1.00e-6	0.45 ± 2.7e-2	33.14 ± 0.467	0.73

detect and characterize the global development of the folds at multiple spatial scales in the neonate and child population.

Specifically, we fit the proposed folding development models (see equation 5.1) to the mean squares of all the wavelet coefficients $\sum_{m=1}^{M(j)} \left|\boldsymbol{\gamma}_{j,m}\right|^2, j \in M(j)$ at each frequency level j. By using the

l^2-norm $|\gamma_{j,m}|$ of wavelet coefficient vectors, we model the change of wavelet power with age, and quantitatively study the development of cortical folding at different spatial scales. In particular, the estimated models using wavelet power at lower levels quantify the development of primary folds since the lower level wavelet coefficients encode the shape variations of the low resolution approximations of cortical surface, and the models at higher levels demonstrate the development of secondary and tertiary folds as they quantify shape variations at smaller spatial scales.

For the purpose of comparing these models across levels, wavelet powers are normalized so that the L^2-norm of wavelet basis function is unity at all levels. As a result, the estimated parameters g_1 (the amount of folding), g_2 (maximum speed of folding development), and g_3 (age of maximum folding development) can be used to quantitatively compare the folding developments across levels.

The results of this study are shown in Figures 5-1 to 5-4 and Table 5.1. Table 5.1 shows that the R^2 values are larger than 0.7 at most of the frequency levels in both hemispheres, indicating good model fitting results. As an example, the estimated Gompertz curves overlaid on the original data at level 0 in both hemispheres are shown in Figure 5-1, with the vertical red line indicating the estimated age of maximum folding development (a logarithmic scale (base 10) is used for the horizontal axis). We summarize the findings with the estimated parameters in the following.

A – Comparison of the hemispheric differences of folding development

First of all, Table 5.1 shows the estimated parameter g_1, whose value at different level encodes the amount of wavelet power at the corresponding spatial scale. A similar value of g_1 within the 90% confidence interval in the left and right hemisphere shows that the amount of folds is equivalent on both sides. Furthermore, the comparison of left and right hemispheres in Figure 5-2 shows that although the age of fastest development is the same, the maximum speed of folding development is higher in the right hemisphere at levels 0 to 4, suggesting that cortical folds develop simultaneously but faster on the right side.

B – Comparison of the folding development age and speed

Furthermore, both Table 5.1 and Figure 5-2 show that the estimated speed of folding development increases from low to high frequency levels (levels 0-3) on both left and right sides, and the estimated age of maximum folding development increases monotonously with frequency level from approximately 29 to 33 weeks. The calculated 90% confidence intervals show that the estimated fastest development ages and speeds are significantly different across frequency levels. These results indicate that the lower frequency folding such as the primary folds develop earlier and slower than the higher frequency folding such as the secondary and tertiary folds.

To demonstrate these results, part of the estimated Gompertz curves including only the 8 newborns at different levels are plotted together in Figure 5-3 and 5-4, where the red vertical lines indicate the maximum development ages estimated for folds of large and smaller scales. Although the data of 3 older children were not shown in Figures 5-3 and 5-4, all 11 data points are used in the actual model fitting. A logarithmic scale (base 10) is used for the vertical axis for better visualization.

At last, we apply the linear models to the wavelet power as described in Section 5.2, which uses a slope and intercept to model the folding development. We find that the proposed nonlinear model has larger marginal likelihood than the linear model in both left and right hemispheres and all frequency levels. This result suggests that the cortical folding development process is not linear and the Gompertz curve is the proper model to use.

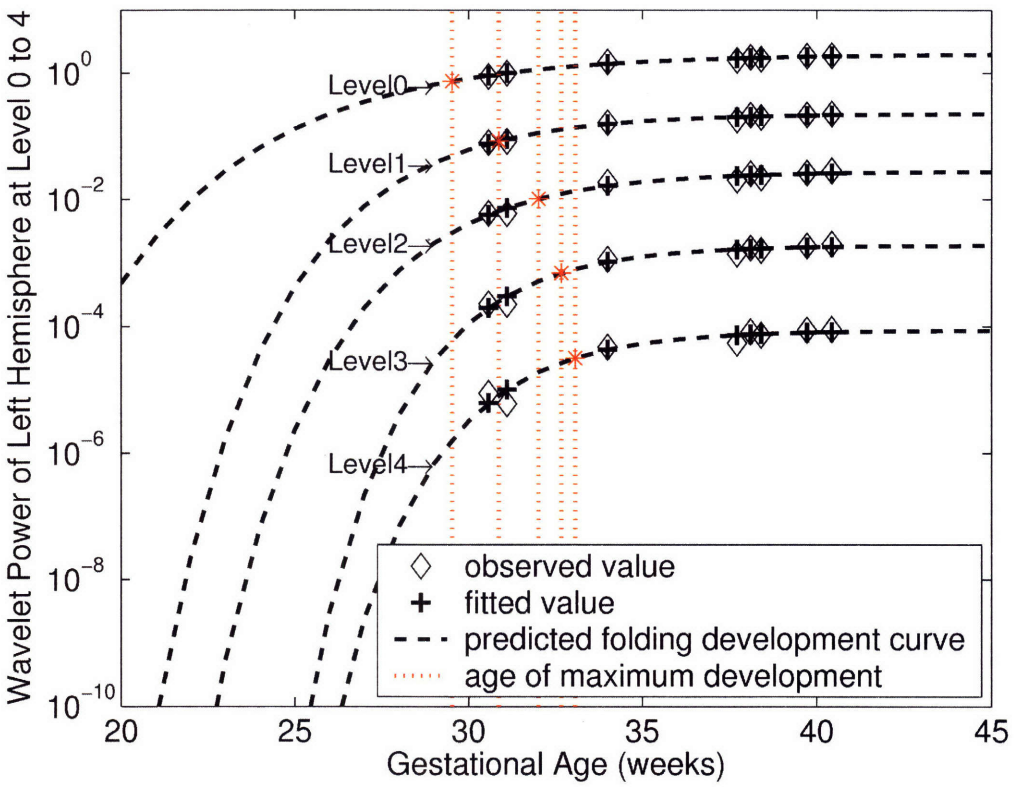

Figure 5-3: The predictive curve at frequency levels 0 to 4 in the left hemisphere (horizontal axis is the gestational age from 20 to 45 weeks; vertical axis is the wavelet power with a logarithmic (base 10) scale).

5.3.2 Regional Folding Development of the Cortical Surface

The cortical folding development model was then estimated for each one of the wavelet coefficients across 11 subjects. Unlike the study of wavelet power, this approach allows us to discover not only when, but also where the folding of the cortical surface occurs at different spatial scales. Although each of the x, y and z components of a wavelet coefficient was estimated with the model, only the estimated parameters $\{g_i\}_{i=1,\cdots 3}$ of the component with the largest R^2 value are used to demonstrate the development of folding in the support region of this wavelet basis function.

In Figure 5-5, we plot the estimated maximum folding development speed and age of the set of wavelet coefficients with $R^2 > 0.5$ on the white matter surface of the youngest newborn. The colormp encodes the estimated parameters, and the location and support regions of the corresponding wavelet basis functions. From these figures, regional differences in folding development are evident as different ages and speeds are estimated for different cortical regions. Furthermore, the linear relationship between development age and speed is persevered for cortical folds of the same spatial scales. The comparison of the age and speed colormaps of the same region at the same level shows that the earlier a region develops (darker blue in the maximum development age colormap), the slower the development speed is (more red and less yellow in the speed

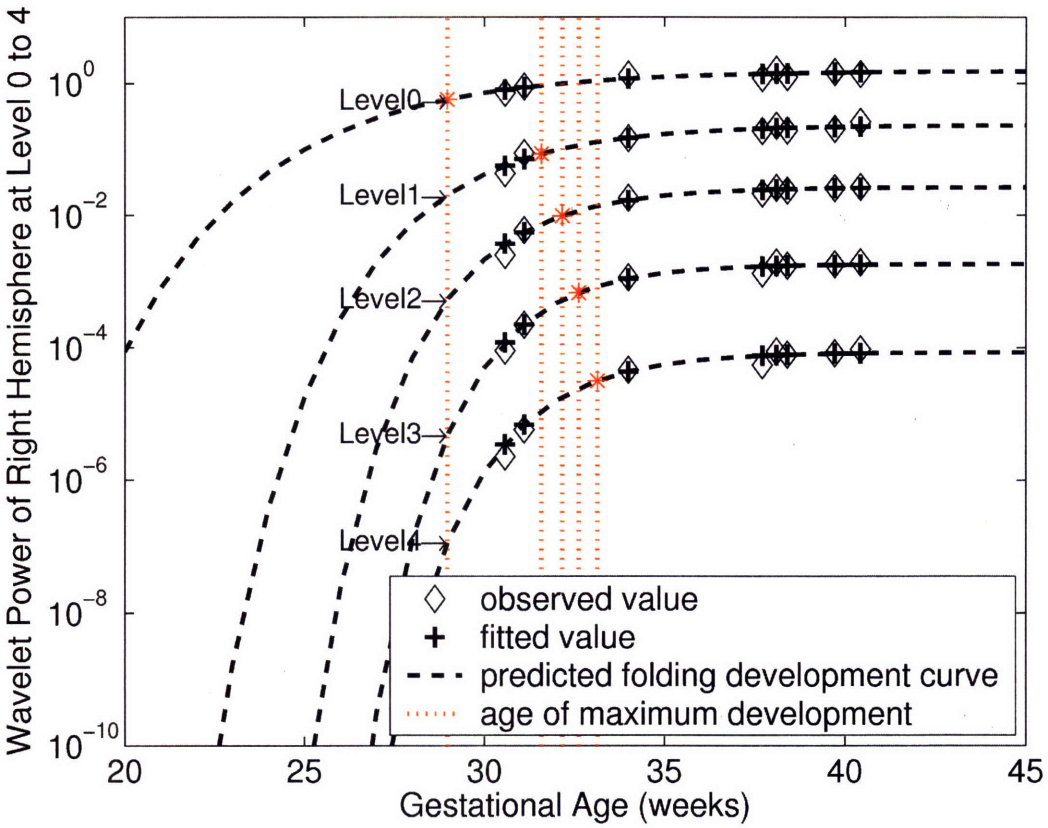

Figure 5-4: The predictive curve at frequency levels 0 to 4 in the right hemisphere (horizontal axis is the gestational age from 20 to 45 weeks; vertical axis is the wavelet power with logarithmic (base 10) scale).

colormap).

Lastly, we can map out where and how fast the folding occurs on the white matter surface at different gestational ages. For this purpose, we first cluster wavelet coefficients into three age intervals, (0, 33), [33, 38) and $[38, \infty)$ weeks, by using the estimated maximum development ages. Then the estimated maximum development speed of the wavelet coefficients in each age interval is plotted as colormap in the support regions of the corresponding wavelet basis functions on a representative brain (newborns with gestational age of 30, 34 and 40 weeks are used as representatives for the three age intervals respectively), as shown in Figure 5-6. The colormap on each surface encodes the estimated speed of the regions that develop the fastest within the specific age interval. Visual inspection shows that most regions that develop at younger gestational ages are of larger scales, and regions that develop at older gestational ages are of smaller scales. This observation further demonstrates the earlier development of larger primary folds followed by the development of secondary and tertiary folds at successively smaller scales.

5.3.3 Discussions

Modeling the cortical folding in the wavelet domain allows us to evaluate the primary folds and smaller scale folds separately in the brain development. Study of the wavelet power shows that

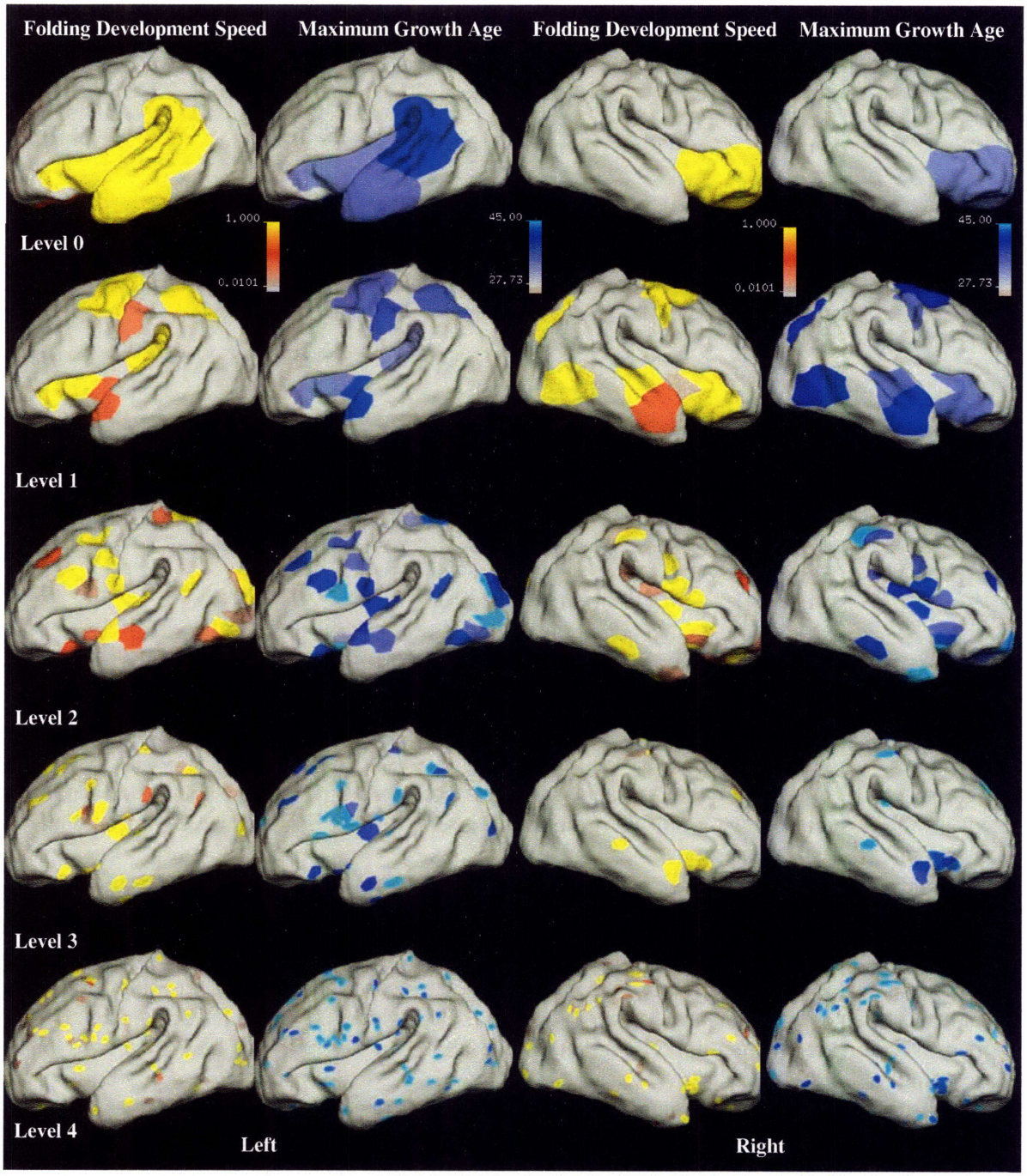

Figure 5-5: The predicted folding development speed and maximum development ages in the left and right hemispheres using individual wavelets at levels 0 to 4. Colormap encodes the magnitude of the estimated maximum development speed (1/week) or age of maximum development (weeks) of wavelet coefficients in the support regions of their corresponding wavelet basis functions. For points in the overlapped regions of two or more wavelet basis functions, the estimated age and speed of the closest wavelet function is assigned. Column 1: Predicted folding development speed in the left hemisphere from levels 0 to 4 (top-down); Column 2: Predicted age of maximum folding development in the left hemisphere from levels 0 to 4 (top-down); Column 3: Folding development speed in the right hemisphere from levels 0 to 4; Column 4: Age of maximum folding development in the right hemisphere from levels 0 to 4.

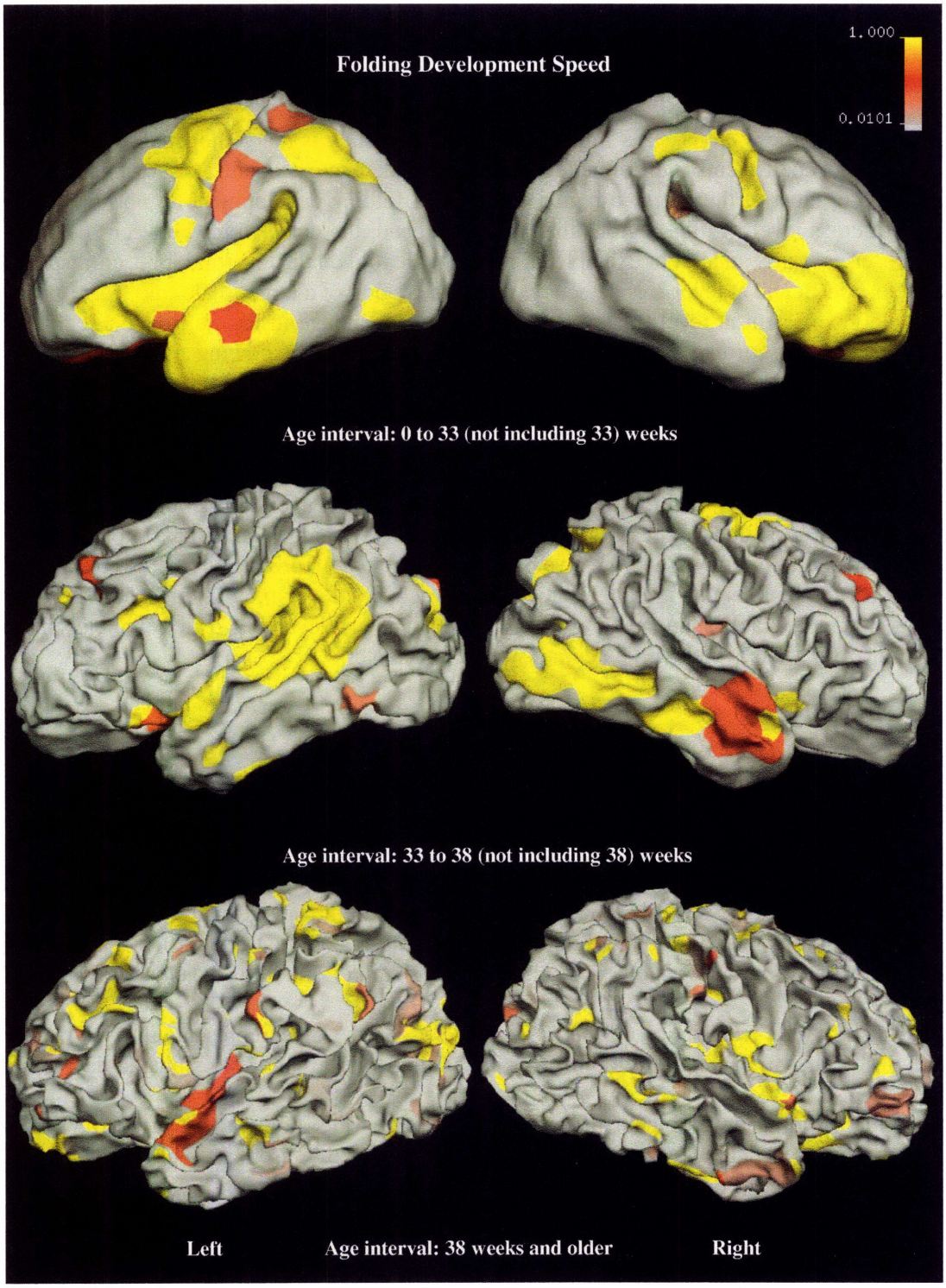

Figure 5-6: Estimated folding development speed of the regions that develop the fastest during gestational age from 0 to 33 weeks (first row), from 33 to 38 weeks (second row), and from 38 weeks to older (third row). Colormap encodes the magnitude of the estimated development speed (1/week) in the support regions of their corresponding wavelet basis functions. For points in the overlapped regions of two or more wavelet basis functions, the estimated speed of the highest level or closest wavelet function is assigned.

larger cortical folds develop at younger gestational ages with slower speeds. Moreover, the individual wavelet coefficient study quantifies the regional differences in folding development, and further demonstrates the positive correlation between estimated maximum development age and speed at the same level.

However, since the wavelet basis functions used in this study is not orthogonal, the correlation between wavelet coefficients at different levels should be taken into account. As shown in Figure 5-5 and Figure 5-6, most of the detected regions of cortical folding development do not overlap with each other across levels. In the regions that are overlapped, the correlations between overlapping wavelet bases are fairly small. For example, a smaller scale fold on the temporal lobe, corresponding to a wavelet coefficient at level 2, is detected to be in the region of a larger scale fold, corresponding to a wavelet coefficient at level 0, as seen in the upper left image in Figure 5-6. The correlation coefficient of the two corresponding wavelet basis functions is 0.031, showing a weak correlation of the folding development detected in these two regions. Therefore, the bi-orthogonality property of the wavelet bases has minor effects on our study of cortical folding development by using wavelet coefficients at different levels separately.

Another limitation is the observation that many regions on the white matter surface do not fit well to the Gompertz model. To address this issue, we have explored several directions. First of all, we have been trying to include more MR scans into this study, which is anticipated to increase the statistical power of this study. Secondly, we have made tentative improvement on the current model to account for the regions that are not identified to be actively developing in this study. Lastly, we have extracted more stable shape features by employing a newly developed over-complete spherical wavelet transformation, which will be demonstrated in Chapter 7.

5.4 Contributions

The study of cortical surface folding development in late gestation demonstrated the power of wavelets in analyzing the underlying function locally in both the space and the frequency domain. In summary, the contributions of our work presented in this chapter are the following:

1) To our knowledge, this temporal model is the first one that has been proposed to quantitatively study the nonlinear folding development of cortical surfaces in the late gestation.

2) By applying this model in the wavelet domain, we discovered that the cortical folds of larger scales develop early, but with a slower speed, while the smaller scale folds develop later and with a faster speed.

3) Because of the localization property of wavelet-based shape representation, we revealed regional differences in folding development by generating cortical maps of estimated development age and speed.

The cortical folding development models built in the wavelet domain provide novel findings regarding normal cortical development and may be potentially used as biomarkers for early diagnosis of neurological deficits in newborns.

This work was published at the *IEEE Transactions on Medical Imaging* [3].

Bibliography

[1] J. G. Chi, E. C. Dooling, and F. H. Gilles, "Gyral development of the human brain," *Annals of Neurology*, vol. 1, 1977.

[2] D. A. Lewis, "Development of the Prefrontal Cortex during Adolescence: Insights into Vulnerable Neural Circuits in Schizophrenia," *Neuropsychopharmacology*, vol. 16, pp. 385-398, 1997.

[3] V. S. J. Caviness, "Mechanical model of brain convolutional development," *Science*, vol. 189, pp. 18-21, 1975.

[4] D. C. V. Essen, "A tension-based theory of morphogenesis and compact wiring in the central nervous system," *Nature*, vol. 385, pp. 313--318, 1997.

[5] P. Yu, P. E. Grant, Y. Qi, X. Han, F. Segonne, R. Pienaar, E. Busa, J. Pacheco, N. Makris, R. L. Buckner, P. Golland, and B. Fischl, "Cortical surface shape analysis based on spherical wavelets,," *IEEE Transaction on Medical Imaging*, vol. 26, pp. 582-598, 2007.

[6] E. P. Virene, "Reliability Growth and Its Upper Limit," *Proceedings of 1968 Annual Symposium on Reliability,*, pp. 265-270, 1968.

[7] C. G. Broyden, "An alternative derivation of simplex method," *Journal of the Institute of Mathematics and Its Applications*, vol. 6, pp. 76-90, 1970.

[8] C. M. Bishop, *Neural networks for pattern recognition*: Oxford university press, 1995.

[9] T. P. Minka, "Using lower bounds to approximate integrals," *CMU Tech Report*, July, 2001.

[10] T. P. Minka, "Bayesian linear regression," *Unpublished manuscript, available from http://www.media.mit.edu/~tpminka*, 1999.

[11] G. A. F. Seber and A. J. Lee, *Linear Regression Analysis*: Wiley-Interscience.

Chapter 6

Shape-guided Subcortical Structure Segmentation

In this chapter, we propose to improve the segmentation of subcortical structures, such as the hippocampus, by incorporating prior shape information extracted with spherical wavelet transformation. We develop a surface deformation method that includes a region-based image term and a boundary-based image term with wavelet-based and generic shape constraints. We obtain the wavelet-based shape constraints from a training set at different frequency levels in the wavelet domain, and encourage the surface to deform inside of the space spanned by the training set. The generic shape constraints allow the surface to deform outside of that space while maintaining the smoothness of the surface. We apply the wavelet-based and generic shape constraints alternately to minimize the image-based energy terms in a multi-scale fashion. The use of the proposed method has demonstrated promising results in improving the segmentation accuracy of the hippocampus in a magnetic resonance imaging dataset.

6.1 Motivation

The hippocampus is one of the most important subcortical neuroanatomical structures, critical to understanding Alzheimer's Disease (AD) as well as the basic memory systems of the human brain. Morphological changes of the hippocampus can be observed in various neurodegenerative disorders, psychiatric disorders and healthy aging [1-7]. The study of these changes *in vivo* can improve our understanding of neuropathology and facilitate early diagnosis when clinical intervention is more likely to be effective.

An accurate segmentation of the hippocampus from Magnetic Resonance Imaging (MRI) data is essential for characterizing the nature and exact location of shape changes. For this purpose, many automated or semi-automated segmentation methods have been developed to replace the time-consuming manual labeling and improve reproducibility. The whole-brain segmentation tool implemented as part of Freesurfer [8, 9], the publicly available software package, is one of most successful and widely used tools for automated labeling of neuroanatomical structures in the human

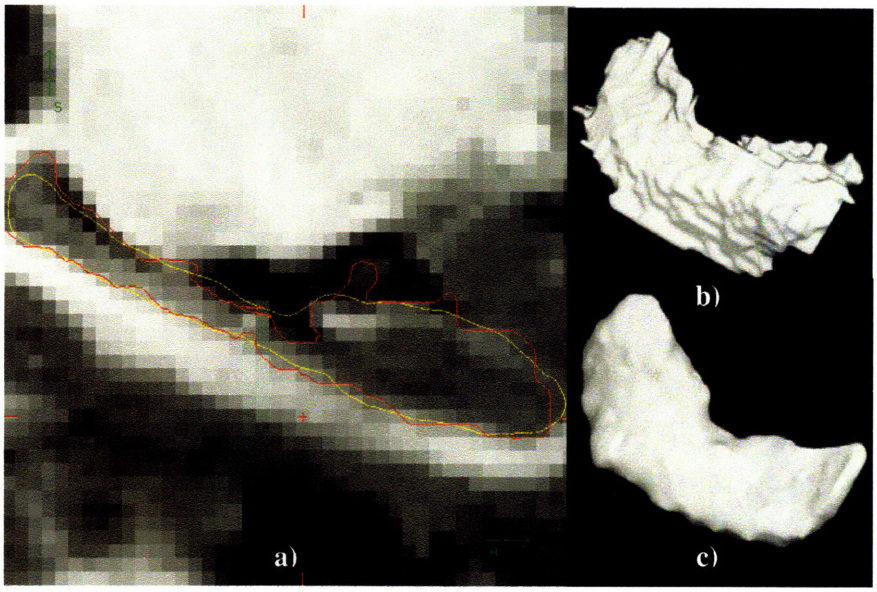

Figure 6-1: a) The manual segmentation (yellow line) and Freesurfer segmentation (red line). b) 3D surface rendering of the Freesurfer segmentation of the hippocampus. c) Manually segmented hippocampus.

brain. It automatically assigns one of 37 labels to each voxel of a volume, including left and right hippocampus, based on probabilistic information obtained from a set of manually labeled training brain volumes. A Bayesian approach, specifically, a maximum a posteriori (MAP) estimation, is used for this segmentation, which considers not only the local intensity distribution of each class, but also the effects of surrounding labels on the probability of having a label at a given location. This technique has been widely used for volumetric study of sub-cortical structures, and has showed to be comparable in accuracy to manual labeling.

Using this tool, we have been able to build reliable shape models of hippocampus. However, we observe one-dimensional protrusions on the reconstructed hippocampus surfaces, particularly in atrophic patients, as shown in Figure 6-1. These spurious protrusions occur in regions where partial volume effects of white matter and the adjacent ventricle can result in a string of voxels with intensities very similar to the hippocampal mean. Since the segmentation method developed in Freesurfer does not incorporate prior knowledge about the smoothness of the boundaries of these structures, these voxels are mistakenly classified as hippocampus purely based on location and intensity information. Differential measures of the curvature in these areas only reveal outliers at the extreme end of the strand, making them difficult to eliminate without sacrificing anatomical accuracy in other regions that may truly have high curvature (e.g. the subiculum).

A natural solution for this problem is to guide the deformation of the segmented hippocampus surface by using statistical shape priors obtained from a training set. This kind of shape model has been extensively studied in medical imaging segmentation. One of the first statistical shape models was proposed by Cootes *et al.* [10] in 1995, where a probability prior is learned from a training set of shapes by estimating a joint probability distribution over a set of boundary points based on Principal Component Analysis (PCA). This prior is then used in a parametric active contour segmentation algorithm called Active Shape Models (ASM) by projecting the evolving shape onto the shape space spanned by the training set and limiting the evolving shape to lie within variances observed in the training set. This method has been extended and successfully used to segment 2D or 3D medical

images [11-15]. However, this type of method tends to neglect the local variation of shapes by using a global shape representation.

To address this problem, Davatzikos *et al.* [16] have proposed a hierarchical active shape model framework for 2D contours by using PCA in the 1D wavelet domain. Nail *et al.* further extend this method into 3D shape segmentation of brain structures, such as hippocampus and caudate nucleus in MRI, by using spherical wavelet transformation [17, 18]. The purpose of building shape models in the wavelet domain is to guide the surface deformation at the coarse and progressively finer spatial resolutions in order to preserve delicate surface features. To further increase the dimension of subspace that the shape can deform in, Davatzikos *et al.*[16] and Nain *et al.* [18] modeled independent groups of the wavelet coefficients clustered with similarity measurements, and Li *et al.* [19] modeled each single wavelet coefficient.

The statistical shape model provides an efficient and effective way to deform the shape using shape information obtained from manually a segmented training set. This method prevents the surface from converging to suboptimal solutions. However, it could restrict the surface in the subspace spanned by the training set, which might be problematic when the training set is small.

In this work, we proposed a method to deform the hippocampus surface using wavelet-based and generic shape constraints in order to improve the segmentation of the hippocampus resulting from the automated Freesurfer tools [20]. We use shape constraints in the wavelet domain based on the observation that most of the protrusions are on a smaller spatial scale. The addition of generic shape constraints allows the shape to deform outside of the space spanned by the training set. In the following sections, we introduce the proposed method in detail and validate its usage to improve the accuracy of segmentation generated with automated Freesurfer tool in a MRI dataset.

6.2 Methods

In this section, we first introduce the preprocessing steps for reconstructing and registering hippocampus surfaces in a spherical coordinate system using Freesurfer tools. The proposed shape deformation framework is then discussed in detail.

6.2.1 Preprocessing

Given a set of MR images with the hippocampus labeled, we use Freesurfer tools to reconstruct the hippocampus surface and register the surfaces in the spherical coordinate system. Although these tools were developed primarily for processing cortical surfaces, as described in Chapter 2, they can be used for subcortical structures of spherical topology, such as hippocampus, with minor parameter changes.

Similar to the procedure introduced in Chapter 2, we first build a surface tessellation for each labeled hippocampus volume after topological defect correction. We then refine the resulting surface to produce a smoother representation due to the fact that the tessellation is jagged at the single-voxel scale. Next, these refined surfaces are inflated and projected radially to a sphere. The metric distortion introduced by the projection process is removed by the minimization of area and local distance distortion [21]. Different from the spherical projection method used for cortical surface, we use a non-linear area preservation term to penalize small triangles due to the fact that the hippocampus is a banana-shape object [22]. With this spherical representation, the hippocampus surfaces of different subjects are then registered in the spherical coordinate system by minimizing an

energy functional, which is a combination of a topology preserving term, a curvature alignment term and a metric distortion minimization term.

The registered hippocampus surfaces are sampled onto an icosahedron at subdivision level 5, which has 10242 points. The coordinates (x, y, z) are normalized to bring each subject into the same coordinate system in the original surface space by using correspondence obtained in the spherical coordinate system. At last, a set of spherical wavelet coefficients from levels -1 to 4 are obtained for each training shape by transforming the normalized coordinate functions.

Given an segmented volume with the hippocampus labeled using Freesurfer tool, we build the surface tessellation and map it onto the sphere using the above described methods, but without the surface refinement process. The surface is then registered to the template built with the training set. Lastly, the registered surface is sampled onto an icosahedron at subdivision level 5. The spherical registration and sampling process give an index to index correspondence between the new surface and the training set.

6.2.2 Segmentation Guided with Shape Models in the Wavelet Domain

The segmentation is accomplished by minimizing energy function so that the deformed surface finds the boundaries of the object in the image and encloses all the voxels that belong to the object, with shape constraints learned from the training set. There are two parts in the energy function: one is a region-based image energy term to maximize the log ratio of the probability that all the voxels enclosed belong to the object; the other one is a boundary-based image energy term to guide the surface to find the edges. First, the surface is deformed to minimize the energy function with shape constraints learned from the training set in the wavelet domain. To allow the surface deform outside the space spanned by the training set, we then replace these model-based shape constraints with generic shape constraints and deform the surface to minimize the energy function again.

A – Image energy term

We first define a region-based image energy term to drive the evolution of the parametric deformable surface $\tilde{S}$ [18]:

$$E_R(\tilde{S}) = \sum_{\tilde{\mathbf{x}} \in \tilde{R}} L(\tilde{\mathbf{x}}) \Delta \tilde{\mathbf{x}} = \sum_{\tilde{\mathbf{x}} \in \tilde{R}} -\log\left(\frac{P(C \mid I, \tilde{\mathbf{x}})}{1 - P(C \mid I, \tilde{\mathbf{x}})}\right) \Delta \tilde{\mathbf{x}}, \tag{6.1}$$

where $\tilde{R}$ is the region inside the evolving surface $\tilde{S}$, $P(C \mid I, \tilde{\mathbf{x}})$ is the posterior probability that a point at position $\tilde{\mathbf{x}} = (x, y, z)$ with intensity I belongs to the object to be segmented. The energy is minimized when the surface evolves to enclose all the voxels that are interior to the object. This label probability is estimated from a set of manually segmented MRI volumes and stored in a probability atlas, which has been used for the automated segmentation and tested on thousands of MR images [8].

We then define a boundary-based image term in order to drive the surface to deform towards the edges of the object:

$$E_B = -\frac{1}{2V} \sum_{i=1}^{V} G(\tilde{\mathbf{x}}_i)^2, \tag{6.2}$$

where V is the total number of vertices on the surface, $G(\tilde{\mathbf{x}}_i)$ is the l^2 norm of the image intensity gradient ($\nabla I(\tilde{\mathbf{x}}_i)$) at the i^{th} surface point.

B – Wavelet-based shape model

In this work, we build shape models using spherical wavelet coefficients of N training surfaces at different frequency levels, separately. This shape model is built with Principal Component Analysis (PCA), similar to the method described in Chapter 3.

At each frequency level, we take only a subset of the coefficients $\boldsymbol{\gamma}_j^n = \{\gamma_{j,m}^n\}_{m \in M(j)}$ from the whole normalized wavelet coefficient set $\{\gamma_{j,m}\}_{j=-1,\ldots 4,\ m \in M(j)}$ of the training surfaces, and calculate the mean coefficients $\bar{\boldsymbol{\gamma}}_j = \frac{1}{N}\sum_{n=1}^{N} \boldsymbol{\gamma}_j^n$, principal components $\mathbf{e}_j^l (l = 1, \cdots, N-1)$, and the corresponding eigenvalue $\lambda_j^1, \lambda_j^2, \cdots, \lambda_j^{N-1}$ at the j^{th} frequency level.

We then represent an evolving surface $\tilde{S}$ using its wavelet coefficients in a matrix form as $\tilde{S} = \mathbf{T}^{-1}\mathbf{F}\mathbf{W}\boldsymbol{\gamma}^{\tilde{S}}$, where $\boldsymbol{\gamma}^{\tilde{S}} = \{\boldsymbol{\gamma}_{-1}^{\tilde{S}}, \ldots, \boldsymbol{\gamma}_4^{\tilde{S}}\}$ denotes the wavelet coefficients of the evolving surface, $\mathbf{W}$ denotes the inverse wavelet transformation, $\mathbf{F}$ denotes the matrix used to transform vector $\mathbf{W}\boldsymbol{\gamma}^{\tilde{S}}$ to a 4×10242 coordinates matrix, and $\mathbf{T}^{-1}$ is the inverse of the affine transformation matrix $\mathbf{T}$, which best aligns the evolving surface with the training set. Before deforming the surface every time, the affine transformation matrix $\mathbf{T}$ is updated to optimize the mean squared error between the current evolving surface and the training set.

Using the eigenvector matrix $\mathbf{e}_j = [\mathbf{e}_j^1, \ldots, \mathbf{e}_j^{N-1}]$ and mean wavelet coefficients $\bar{\boldsymbol{\gamma}}_j$ calculated from the training set at the j^{th} level, we can approximate the evolving surface $\tilde{S}$ as:

$$\tilde{S} = \mathbf{T}^{-1}\mathbf{F}\mathbf{W}\left(\begin{bmatrix} \boldsymbol{\gamma}_{-1}^{\tilde{S}} \\ \vdots \\ \bar{\boldsymbol{\gamma}}_j \\ \vdots \end{bmatrix} + \begin{bmatrix} 0 \\ \vdots \\ \mathbf{e}_j \\ 0 \end{bmatrix}\boldsymbol{\alpha}\right), \tag{6.3}$$

where the surface's wavelet coefficients at level j is the summation of the mean wavelet coefficients calculated from the training set, and a linear combination of eigenvectors weighted by shape parameters $\boldsymbol{\alpha} = [\alpha_1, \ldots \alpha_{N-1}]^T$. Notice that the wavelet coefficients at other frequency levels are maintained when we model the shapes at the j^{th} frequency level.

By using this shape model, we constrain the surfaces by keeping only the first N-1 eigenvectors, which is equivalent to limiting the shape parameters corresponding to the rest of eigenvectors to 0. We also limit the first N-1 shape parameters to be within ± 3 standard deviations of the projections of the training set.

C – Generic shape models

We replace the wavelet-based shape models with two spring-like smoothness terms to allow the surface to deform outside of the space spanned by the training set, but still keeping its smoothness. The normal spring term $E_n(\tilde{\mathbf{x}})$ imposes a smoothness constraint on the surface and the tangential term $E_t(\tilde{\mathbf{x}})$ acts to encourage a uniform spacing of vertices [23]:

$$E_n(\tilde{\mathbf{x}}) = \frac{1}{2V}\sum_{i=1}^{V}\Big(\sum_{n \in N_1(i)}(\tilde{n}_i \cdot (\tilde{\mathbf{x}}_i - \tilde{\mathbf{x}}_n))^2\Big), \tag{6.4}$$

$$E_t(\tilde{\mathbf{x}}) = \frac{1}{2V}\sum_{i=1}^{V}\Big(\sum_{n\in N_1(i)}((\tilde{e}_0(i)\cdot(\tilde{\mathbf{x}}_i-\tilde{\mathbf{x}}_n))^2+(\tilde{e}_1(i)\cdot(\tilde{\mathbf{x}}_i-\tilde{\mathbf{x}}_n))^2)\Big), \tag{6.5}$$

where $\tilde{\mathbf{x}}$ denotes the coordinates of surface point, $N_1(i)$ denotes the set of nearest neighbors of the i^{th} vertex, $\tilde{n}_i$ is the unit normal vector to the surface at the i^{th} vertex, and $[\tilde{e}_0(i),\tilde{e}_1(i)]$ is an orthonormal basis for the tangent plane at the i^{th} vertex. The overall generic shape model is $E_S = \lambda_n E_n + \lambda_t E_t$, where λ_n and λ_t specify the relative strength of the normal and tangential spring terms.

D – Surface deformation

Given a surface reconstructed based on Freesurfer segmentation, we deform it to minimize the overall image energy terms $E = \lambda_R E_R + \lambda_B E_B$ alternately with shape constraints from the wavelet-based shape model and generic shape model. The weights λ_R and λ_B specify the relative strength of the region-based and the boundary-based terms.

To use the wavelet-based shape model, we start with an initial surface, register it with the training set, and transform it in the wavelet domain. At each frequency level j, we model the surface using the mean wavelet coefficients and a linear combination of the eigenvectors calculated from the training data (equation 6.3). Then we deform the surface to minimize the overall image energy function by gradient descent.

To minimize the region-based image energy term, we use the shape gradient and chain-rule to express the summation in a region as a summation on the surface [24, 25], and derive the gradient of the energy term with respect to each shape parameter $\alpha_k \in \boldsymbol{\alpha}$ as:

$$\frac{dE_R}{d\alpha_k} = \sum_{i=1}^{V}\left\langle(\mathbf{T}_m^{-1}\mathbf{F}_m\mathbf{W}\begin{bmatrix}0 & \cdots & \mathbf{e}_j^{kT} & \cdots & 0\end{bmatrix}^T)_i, L(\tilde{\mathbf{x}}_i)\tilde{n}_i\right\rangle, \tag{6.6}$$

where V is the total number of vertices on the surface, $\tilde{n}_i$ is the outward unit normal vector of the i^{th} surface point, and the subscript i in the matrix product $\mathbf{T}_m^{-1}\mathbf{F}_m\mathbf{W}\begin{bmatrix}0 & \cdots & \mathbf{e}_j^{kT} & \cdots & 0\end{bmatrix}^T$ indicates that only the component corresponding to the surface point i is considered. Here $\mathbf{T}_m^{-1}$ is a 3×3 matrix generated by removing the last row and last column of $\mathbf{T}^{-1}$. Also, $\mathbf{F}_m$ transforms the wavelet coefficient vector to a 3×10242 matrix with only coordinates x, y and z.

Similarly, we derive the gradient of the boundary-based image energy term with respect to each shape parameter $\alpha_k \in \boldsymbol{\alpha}$ as:

$$\frac{dE_B}{d\alpha_k} = \sum_{i=1}^{V}\left\langle(\mathbf{T}_m^{-1}\mathbf{F}_m\mathbf{W}\begin{bmatrix}0 & \cdots & \mathbf{e}_j^{kT} & \cdots & 0\end{bmatrix}^T)_i, -\langle\nabla G(\tilde{\mathbf{x}}_i),\tilde{n}_i\rangle\tilde{n}_i\right\rangle, \tag{6.7}$$

where $\nabla G(\tilde{\mathbf{x}}_i)$ denotes the gradient of magnitude of intensity gradient at the i^{th} surface point.

Using these gradients, we update shape parameters at frequency level j:

$$\alpha_k(t+1) = \alpha_k(t) - \lambda_s^R\frac{dE_R}{d\alpha_k} - \lambda_s^B\frac{dE_B}{d\alpha_k}, \tag{6.8}$$

$$\tilde{S}(t+1) = \mathbf{T}^{-1}\mathbf{W}\left(\begin{bmatrix} \boldsymbol{\gamma}_{-1}^{\tilde{S}(t)} \\ \vdots \\ \overline{\boldsymbol{\gamma}}_j \\ \vdots \end{bmatrix} + \begin{bmatrix} 0 \\ \vdots \\ \mathbf{e}_j \\ 0 \end{bmatrix}\boldsymbol{\alpha}(t+1)\right), \tag{6.9}$$

where λ_s^R and λ_s^B are step sizes with respect to the region-based and boundary-based energy terms, and t indicates each iteration. The shape parameters are initiated using the projections of the initial surface onto the eigenvectors. To constrain the surface, the updated shape parameters are limited to be within ± 3 standard deviation observed in the training set.

After the surface is updated according to the wavelet-based shape model, we then deform the surface using the generic shape models. This time we minimize the image-based energy functional by moving the vertex in the negative direction of the derivative of the energy terms with respect to the vertex

$$\Delta\tilde{\mathbf{x}}_i = -(\lambda_R \frac{\partial E_R}{\partial \tilde{\mathbf{x}}_i} + \lambda_B \frac{\partial E_B}{\partial \tilde{\mathbf{x}}_i} + \lambda_n \frac{\partial E_n}{\partial \tilde{\mathbf{x}}_i} + \lambda_t \frac{\partial E_t}{\partial \tilde{\mathbf{x}}_i}), \tag{6.10}$$

$$-\frac{\partial E_R}{\partial \tilde{\mathbf{x}}_i} = -L(\tilde{\mathbf{x}}_i)\tilde{n}_i = \log(\frac{P(C \mid I, \tilde{\mathbf{x}}_i)}{1 - P(C \mid I, \tilde{\mathbf{x}}_i)})\tilde{n}_i, \tag{6.11}$$

$$-\frac{\partial E_B}{\partial \tilde{\mathbf{x}}_i} = \langle \nabla G(\tilde{\mathbf{x}}_i), \tilde{n}_i \rangle \tilde{n}_i, \tag{6.12}$$

$$-\frac{\partial E_n}{\partial \tilde{\mathbf{x}}_i} = \sum_{n \in N_1(i)} \langle \tilde{n}_i, \tilde{\mathbf{x}}_n - \tilde{\mathbf{x}}_i \rangle \tilde{n}_i, \tag{6.13}$$

$$-\frac{\partial E_t}{\partial \tilde{\mathbf{x}}_i} = \sum_{n \in N_1(i)} (\langle \tilde{e}_0(i), \tilde{\mathbf{x}}_i - \tilde{\mathbf{x}}_n \rangle \tilde{e}_0(i) + \langle \tilde{e}_1(i), \tilde{\mathbf{x}}_i - \tilde{\mathbf{x}}_n \rangle \tilde{e}_1(i)), \tag{6.14}$$

where $\nabla G(\tilde{\mathbf{x}}_i)$ denotes the gradient of magnitude of intensity gradient at the i^{th} surface point, $N_1(i)$ denotes the set of nearest neighbors of the i^{th} vertex, $\tilde{n}_i$ is the unit normal vector to the surface at the i^{th} vertex, and $[\tilde{e}_0(i), \tilde{e}_1(i)]$ is an orthonormal basis for the tangent plane at the i^{th} vertex [23]. Moreover, the movement of each vertex is checked and cropped to prevent a large movement and possible surface self-intersection before being applied.

We deform the surface in a multi-scale fashion at low and gradually higher frequency levels with increasing step size (equation 6.8). We also gradually decrease the width of the Gaussian smoothing kernel from low to high frequency levels. At each frequency level, the surface is first deformed using wavelet-based shape constraints (equations 6.8 and 6.9), and then with the generic shape constraints (equation 6.10). Before updating the surface based on shape models in the wavelet domain, we renormalize the evolving surface to find the best alignment with the training set. At each frequency level, this process is iterated until the overall image energy function $E = \lambda_R E_R + \lambda_B E_B$ converges.

6.3 Experimental Design and Results

We test the proposed shape-driven deformation method in a dataset of 41 MR images, segmented with Freesurfer tool. Manual segmentation is also available for this dataset, which is used to validate the ability of our method to improve the segmentation based purely on image information. We

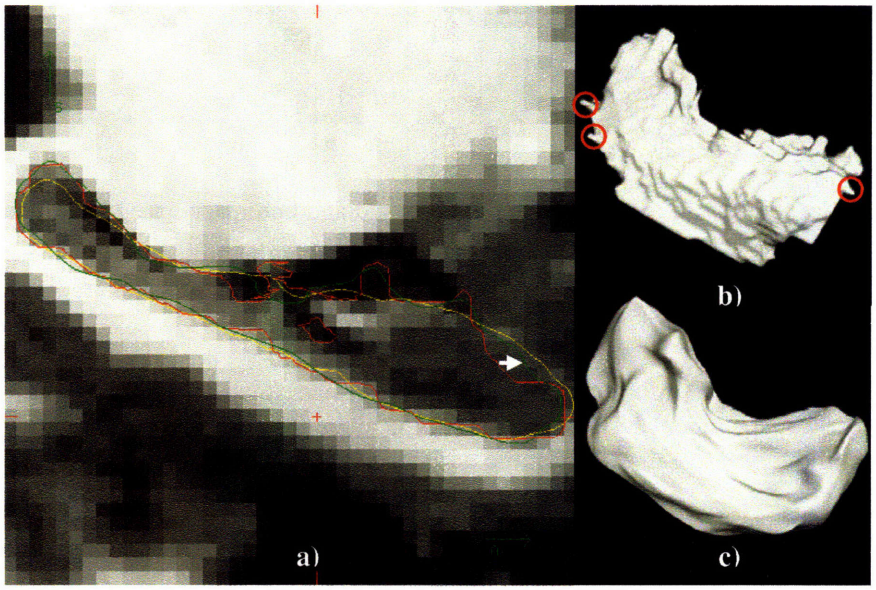

Figure 6-2: a) A sagittal slice of structure MRI image with overlaied surfaces: Manually segmented surface (yellow line), Freesurfer segmentation (red line), and new surface generated with the shape-guided segmentation method (green line). An arrow points to a region that is correctly segmented using shape-guided segmentation method. b) 3D surface rendering of the Freesurfer segmentation of the hippocampus: Red circle indicates artificial protrusion generated because of the imperfections in MR image. c) New surface generated with the shape-guided segmentation method.

conduct a cross-validation to deform one subject based on our new method using the wavelet-based shape model built with the other 40 subjects. We compare the new segmentation with the manual segmentation for the left-out subject each time. The process is iterated through the whole dataset. We visually inspect the surface generated from the new segmentation overlaid on the manually segmented surface, and quantitatively compare the resulting new segmentation with the manual segmentation. Although this experiment is only conducted for the hippocampus on the left side, our method can be potentially applied to any subcortical structures with 2D closed surfaces on both sizes.

A – Visual validation

Visual inspection shows that the resulting surface using our deformation method is not only smoother, but also located closer to the edges of the hippocampus. As an example, Figure 6-2 b) and c) compare the hippocampus surfaces before and after the surface deformation. The protrusions on the surface generated from segmentation based purely on image information, highlighted by the red circles in Figure 6-2 b), are eliminated after the surface deformation. In Figure 6-2 a) we show a sagittal slice of the original structure MR image overlaid with the hippocampus surfaces enclosing the manual segmentation (yellow contour), Freesurfer segmentation (red contour), and our new segmentation (green contour). As pointed out by the white arrow, the new surface is deformed to the boundary of the hippocampus and matches better with the surface generated using manual segmentation.

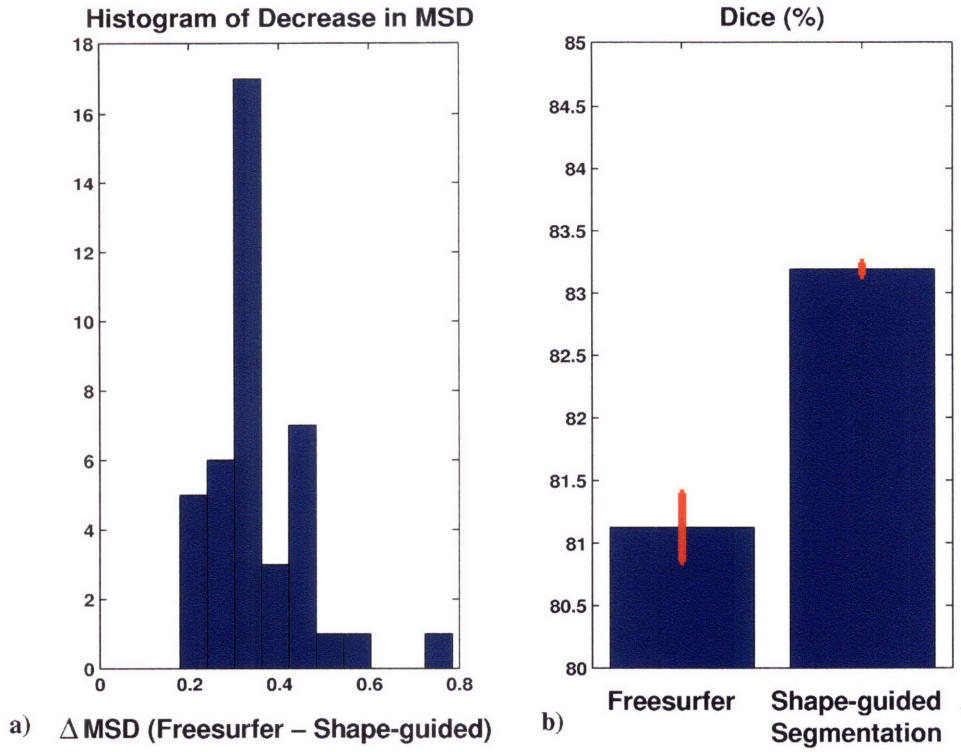

Figure 6-3: a) Histogram of the decrease in MSD measured for 41 surfaces using the shape-guided segmentation method; The x axis is the difference between MSD of the surface segmented with Freesurfer tool and MSD of new surface. A significant decrease in MSD is observed for all the subjects. b) Comparison of the average Dice coefficients measured for Freesurfer segmentation and the shape-guided segmentation method. Paired t-test shows a significant increase in Dice coefficients.

B – Quantitative validation

We use the manual segmentation as standard to quantitatively compare the new segmentation, which is obtained from the surface deformation, with the segmentation generated by Freesurfer. We first calculate the mean square distance (MSD) of the new surface to the surface generated from the manual segmentation. Since the new surface is registered to the manually labeled hippocampus surface, we can calculate MSD as the mean square error of points on the new surface to the corresponding points on the manually segmented surface. We then calculate the MSD between the surface generated from Freesurfer segmentation and surface generated from manual segmentation. Comparison shows that the new surface reduces the MSD by $7.79 \pm 0.0891\%$, averaged across the 41 surfaces. This decrease is significant with $p < 0.0001$ using the paired t-test. Figure 6-3 a) shows the histogram of the decrease in MSD measurement of all the subjects by using the shape-guided segmentation method.

We also calculate the Dice coefficient $Dice = 2(A \cap B)/(A + B)$ [26] to quantify the overlap between two segmentations. As a result, we find the Dice coefficient between new segmentation and manual segmentation is $83.19 \pm 0.018\%$ across the entire dataset, as shown in Figure 6-3 b). Paired t-test again shows this result is a significant increase from the Dice coefficient = $81.12 \pm 0.092\%$ between the Freesurfer and manual segmentations.

6.4 Contributions

In this chapter, we introduce our first attempt to improve the segmentation of subcortical structures, e.g. the hippocampus, based on image models guided with a combination of wavelet-based and generic shape constraints. The proposed method has been demonstrated to improve the segmentation using the automated Freesurfer tools in an MRI dataset.

In summary, the contributions of our work presented in this chapter are the following:

1) We proposed to use a combination of wavelet-based and generic shape constraints. The shape constraints built with spherical wavelet transformation guide the surface to deform based on the training shapes from a coarse to gradually finer resolutions. We then proposed to replace these wavelet-based shape constraints with generic shape constraints to allow the surface to deform outside of the space spanned by the training set.

2) We employed a region based image model to utilize the posterior probability of having a label considering both the intensity and global spatial location, and a boundary based image model to guide the surface to deform to the boundary of object. The label probability is extracted from a probabilistic atlas generated from carefully segmented MR images and successfully used to segment thousands of MR images.

Applications of this method to segmenting hippocampus show promising results with visual inspection and quantitative comparison with manual segmentation. This method will be further improved to fully utilize the localization property of the wavelet transformation and tested on a larger dataset.

Bibliography

[1] J. W. Haller, G. E. Christensen, S. Joshi, J. W. Newcomer, M. I. Miller, J. C. Csernansky, and M. W. Vannier, "Hippocampal mr imaging morphometry by means of general pattern matching," Radiology, vol. 199, pp. 787-791, 1996.

[2] J. G. Csernansky, S. Joshi, L. Wang, J. W. Haller, M. Gado, J. P. Miller, U. Grenander, and M. Miller, "Hippocampal morphometry in schizophrenia by high dimensional brain mapping," Proc. Nat. Acad. of Science, vol. 95, pp. 11406-11411, 1998.

[3] R. C. Petersen, C. R. J. Jack, Y. C. Xu, S. C. Waring, P. C. O'Brien, G. E. Smith, R. J. Ivnik, E. G. Tangalos, B. F. Boeve, and E. Kokmen, "Memory and MRI-based hippocampal volumes in aging and AD," Neurology, vol. 54, pp. 581-587, 2000.

[4] L. Wang, S. C. Joshi, M. I. Miller, and J. G. Csernansky, "Statistical analysis of hippocampal asymmetry in schizophrenia.," NeuroImage, vol. 14, pp. 531-545, 2001.

[5] M. E. Shenton, G. Gerig, R. W. McCarley, G. Szekely, and R. Kikinis, "Amygdala-hippocampal shape differences in schizophrenia: the application of 3D shape models to volumetric MR data," Psychiatry Research: Neuroimaging, vol. 115, pp. 15-35, 2002.

[6] G. Gerig, K. Muller, E. Kistner, Y. Chi, M. Chakos, M. Styner, and J. Lieberman, "Age and treatment related local hippocampal changes in schizophrenia explained by a novel shape analysis method," Proceedings of Image Computing and Computer-Assisted Intervention MICCAI 2003, pp. 651-660, 2003.

[7] M. Styner, J. Lieberman, D. Pantazis, and G. Gerig, "Boundary and Medial Shape Analysis of the Hippocampus in Schizophrenia," Med Image Anal, vol. 8, pp. 197-203, 2004.

[8] B. Fischl, D. H. Salat, E. Busa, M. Albert, M. Dieterich, C. Haselgrove, A. van der Kouwe, R. Killiany, D. Kennedy, S. Klaveness, A. Montillo, N. Makris, B. Rosen, and A. M. Dale, "Whole brain segmentation: Automated labeling of neuroanatomical structures in the human brain," Neuron, vol. 33, pp. 341-355, 2002.

[9] B. Fischl, D. Salat, A. van der Kouwe, N. Makris, F. Segonne, B. Quinn, and D. AM., "Sequence-Independent Segmentation of Magnetic Resonance Images," Neuroimage, vol. I23, pp. S69-S84, 2004.

[10] T. F. Cootes, C. J. Taylor, D. H. Cooper, and J. Graham, "Training Models of Shape from Sets of Examples," Proc. British Machine Vision Conference, Springer-Verlag, pp. 9-18, 1992.

[11] T. Cootes, C. Taylor, D. Cooper, and J. Graham, "Active shape models - their training and application," Computer Vision and Image Understanding, vol. 61, pp. 38-59, 1995.

[12] G. Szekely, A. Kelemen, C. Brechbuhler, and G. Gerig, "Segmentation of 2D and 3D objects from MRI volume data using constrained elastic deformations of flexible Fourier contour and surface models," Medical Image Analysis, vol. 1, pp. 19-34, 1996.

[13] A. Kelemen, G. Szekely, and Gerig G., "Three-dimensional Model-Based Segmentation," Proc. IEEE Intl. Workshop on Model Based 3D Image Analysis, Bombay, India, pp. 87-96, 1998.

[14] Y. Wang and L. H. Staib, "Boundary finding with correspondence using statistical shape models," Proc. IEEE Conf. Computer Vision and Pattern Recognition, pp. 338-345, 1998.

[15] M. E. Leventon, W. E. L. Grimson, and O. Faugeras, "Statistical Shape Influence in Geodesic Active Contours," Proc. CVPR'2000, pp. 316-323, 2000.

[16] C. Davatzikos, X. Tao, and D. Shen, "Hierarchical active shape models, using the wavelet transform," IEEE Trans. Medical Imaging, vol. 22, pp. 414-423, 2003.

[17] D. Nain, S. Haker, A. Bobbick, and A. Tannenbaum, "Shape-driven surface segmentation using spherical wavelets," presented at MICCAI, Oct 1-6, 2006.

[18] D. Nain, S. Haker, A. Bobick, and A. Tannenbaum, "Multiscale 3-d shape representation and segmentation using spherical wavelets," IEEE Transaction on Medical Imaging, vol. 26, pp. 598-618, 2007.

[19] Y. Li, T.-S. Tan, I. Volkau, and W. L. Nowinski, "Model-guided segmentation of 3D neuroradiological image using statistical surface wavelet model," In Proceeding of Computer Vision and Pattern Recognition, 2007.

[20] "http://surfer.nmr.mgh.harvard.edu."
[21] B. Fischl, M. I. Sereno, and A. M. Dale, "Cortical surface-based analysis. II: Inflation, flattening, and a surface-based coordinate system," Neuroimage, vol. 9, pp. 195-207, 1999.
[22] L. Zhu and T. Jiang, "Parameterization of 3D brain structures for statistical shape analysis.," In Proc. of SPIE Medical Imaging, vol. 5370, pp. 1254-1262, 2004.
[23] A. M. Dale, B. Fischl, and M. I. Sereno, "Cortical surface-based analysis I: Segmentation and surface reconstruction," Neuroimage, vol. 9, pp. 179-194, 1999.
[24] R. Goldenberg, R. Kimmel, E. Rivlin, and M. Rudzsky, "Cortex segmentation: A fast variational geometric approach," IEEE Trans. on Medical Imaging, vol. 21, pp. 1544-1551, 2002.
[25] A. Tsai, A. Yezzi, W. Wells, C. Tempany, D. Tucker, A. Fan, W. E. Grimson, and A. Willsky, "A shape-based approach to the segmentation of medical imagery using level sets," IEEE Trans on Medical Imaging, vol. 22, pp. 137-154, 2003.
[26] L. R. Dice, "Measures of the amount of ecologic association between species," Ecology, vol. 26, pp. 297-302, 1945.

Chapter 7

Cortical Shape Study Based on Over-complete Spherical Wavelets

In this chapter, we adopt a newly developed over-complete spherical wavelet transformation for representing the cortical surface. Bi-orthogonal spherical wavelets have been shown to be powerful tools in the shape analysis and segmentation of the 2D closed surfaces of neuroanatomical structures. Unfortunately, they suffer from aliasing problem and are therefore not invariant under rotation of the underlying surface parameterization. In this chapter, we demonstrate the theoretical advantage of over-complete wavelets over bi-orthogonal wavelets and illustrate their utility on both synthetic and real data. In particular, we show that over-complete spherical wavelets allow us to build more stable cortical folding development models, and detect a wider array of regions of folding development in a dataset of newborn.

7.1 Motivation

In this thesis, we have developed a method to extract shape feature of 2D closed surfaces of neuroanatomical structures using the bi-orthogonal spherical wavelet transformation. Using wavelet-based shape representation, we have conducted multi-scale and localized shape study of the cortical surfaces. In our and other's work, shape representation based on bi-orthogonal spherical wavelets has also been successfully used to guide the segmentation of sub-cortical brain structures based on Magnetic Resonance Imaging (MRI) [1, 2].

The bi-orthogonal spherical wavelets we used, as introduced in Chapter 2, adopts a non-parametric approach to computing a wavelet decomposition of arbitrary meshes by the lifting scheme. This wavelet construction method [3] generalizes the standard 2-scale relation of the Euclidean wavelets, and enables multi-scale representation of the original mesh (image) with excellent compression performance and efficiency.

7.1.1 Limitation of Shape Representation Based on Bi-orthogonal Spherical Wavelets

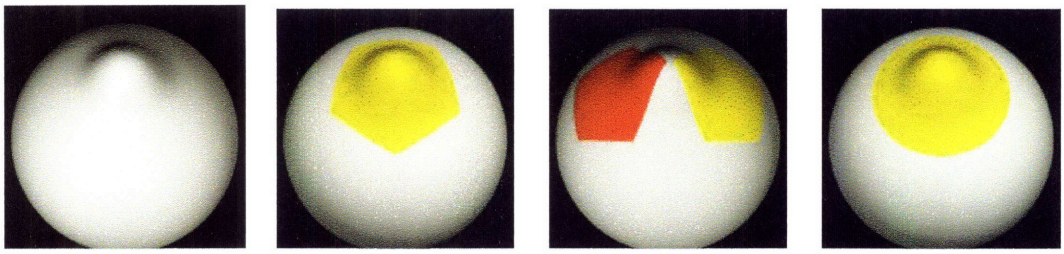

Figure 7-1: The comparison of bi-orthogonal and over-complete spherical wavelets in detecting local shape variation. a) Synthetic surface with a bump. b) The bi-orthogonal wavelet coefficient that has the largest magnitude when the bump is centered at a point on the low frequency surface mesh. c) The bi-orthogonal wavelet coefficients with large magnitude when the surface parameterization is rotated. d) The over-complete wavelet coefficients are not invariant to the rotation of underlying surface parameterization.

Unfortunately, the bi-orthogonal spherical wavelet transform is not rotational invariant under rotations of the surface parameterization. Since we are considering 2D closed surfaces with spherical topology, a natural parameterization is a 1-1 mapping to the sphere. The rotation of surface parameterization refers to the rotation of the underlying spherical coordinate system.

Figure 7-1 shows a toy example that illustrates the sensitivity of bi-orthogonal wavelets to the rotation of surface parameterization. We first generate a bump centered at the north pole on a sphere, as shown in Figure 7-1 a). We then apply the bi-orthogonal wavelet transform to both the original surface and the reparameterized surface where the spherical coordinate is rotated by an arbitrary angle. Figure 7-1 b) and 7-1 c) show the bi-orthogonal wavelet coefficients at the lowest frequency level (coarsest spatial scale) that have significant magnitude before and after the rotation of surface parameterization. With the original parameterization, we can accurately detect the location of the bump since only the wavelet coefficient at the center of the bump has large magnitude, illustrated by a single bright spot in Figure 7-1 b). However, with the rotation of parameterization, two wavelet coefficients have significant magnitude, as shown by the two bright spots in Figure 7-1 c).

The bi-orthogonal wavelet transform is not invariant under rotation of the underlying parameterization because it sub-samples the signal progressively when decomposing it at the lower frequency (coarser) levels, as introduced in Chapter 2. This sub-sampling causes aliasing at all the single frequency levels although all the levels, when combined, add up to an invertible transform. As demonstrated in the toy example (Figure 7-1 c)), when the shape deformation is centered around a point on the coarse scale surface mesh, then the location of the bump is perfectly detected. However, when the underlying surface parameterization is rotated so that the bump does not align with the points on the coarse scale mesh anymore, we lose the ability to accurate locate the surface deformation, as shown in Figure 7-1 c). This is problematic since being able to analyze the wavelet coefficients at each individual frequency level is one of the advantages of wavelet transform. Consequently, shape analysis results can vary significantly with the rotation of surface parameterization and one loses the ability to accurately localize geometric characteristics of interest.

7.1.2 Over-complete Spherical Wavelets

The aliasing of individual levels of orthogonal and bi-orthogonal wavelets is a well-known problem in the Euclidean domain. Over-complete wavelets, such as the steerable pyramid proposed by

Simoncelli *et al.* [4], are useful for solving the aliasing problem. Recently, the corresponding steerable pyramid in the spherical domain was proposed by Antoine *et al.* [5] and discretized by Bogdanova *et al.* [6] for axis-symmetric wavelets. Unlike the steerable pyramid, their method of construction is grounded in group or representation theory.

In this chapter, we propose to use the over-complete wavelets introduced by Yeo *et al.* [7]. Their over-complete wavelets are based on filter bank theory, directly extending the ideas of Simoncelli to the sphere. In this work we only consider invertible axis-symmetric wavelets which are not necessarily self-invertible. We note that axis-symmetric spherical wavelets are symmetrical about the north pole.

With the over-complete wavelet transformation, we can always accurately detect the single bump, as shown in Figure 7-1 d), regardless of the rotation of the underlying surface parameterization. The over-complete wavelet transformation achieves such invariance by sufficiently sampling at each level of the wavelet transform.

In this chapter, we introduce the construction of over-complete spherical wavelets, theoretically prove the invariance property of the over-complete wavelet transform, and compare it with the bi-orthogonal spherical wavelets. In section 7.3, we describe the use of both wavelets in building cortical folding development models in the dataset of newborn analyzed in Chapter 5. We show the advantage of the over-complete wavelets in providing more accurate and sensitive results for this cortical folding development study.

7.2 Shape Representation Based on Over-complete Spherical Wavelets

For closed 2D surface that has a spherical topology, various methods have been developed to impose a spherical coordinate system on the surface [8, 9]. In the underlying spherical coordinate system, we can use $\{x(\theta_i,\phi_i), y(\theta_i,\phi_i), z(\theta_i,\phi_i)\}$ to denote the set of mesh vertices indexed by i. Many parametric mesh representations have been proposed, including spherical harmonics [8], polynomials [10] and bi-orthogonal spherical wavelets [1, 2], to transform or decompose the individual coordinate functions $x(\theta_i,\phi_i)$, $y(\theta_i,\phi_i)$ and $z(\theta_i,\phi_i)$ separately.

In this chapter, we use the over-complete wavelet transform to decompose the coordinate function defined on the surface and use the resulting wavelet coefficients for shape analysis. Without loss of generality, we introduce the over-complete spherical wavelet transform for a generic scalar spherical function $f(\theta,\phi)$ in the following subsection.

7.2.1 Over-complete Spherical Wavelets

The construction of the over-complete spherical wavelet function is based on the general continuous filter bank theory [7]. Continuous spherical function $f(\theta,\phi)$ is projected onto the space of N spherical analysis filters $\{\tilde{h}_n(\theta,\phi)\}_{n=1}^{N}$ by performing a spherical convolution between $f(\theta,\phi)$ and each analysis filter $\tilde{h}_n(\theta,\phi)$.

In the case of axis-symmetric spherical filters, the convolution outputs are also spherical images $\{g_n(\theta,\phi)\}_{n=1}^{N}$. We can then perform an inverse spherical convolution between each convolution output $g_n(\theta,\phi)$ and corresponding spherical synthesis filter $h_n(\theta,\phi)$, and obtain a

reconstructed image $\hat{f}(\theta,\phi)$ by summing the outputs of the inverse spherical convolution. The system of forward and inverse spherical convolutions, using analysis and synthesis filters respectively, is invertible if $\hat{f}$ is equal to f.

We define the system of spherical filters to be an over-complete forward and inverse wavelet transform if it is invertible and the analysis filters $\{\tilde{h}_n(\theta,\phi)\}_{n=1}^{N}$ are dilated versions of a mother wavelet.

For this work in particular, we choose the Laplacian-of-Gaussian on the plane as our mother wavelet. We then perform the usual dilation on the plane to generate the differently dilated daughter wavelets. At last, we stereographically project the set of wavelets onto the sphere to obtain the corresponding wavelet analysis filters. This process of dilation via the plane is known as stereographic dilation and is utilized because dilation on a sphere is necessarily non-linear [5-7].

Noting that the spherical harmonics are a set of orthonormal basis for functions on $L^2(S^2)$ and denoting by $h_{l,m}$ the spherical harmonic coefficient of degree l and order m of a spherical function h, we define the synthesis filters to be [7]:

$$h_n^{l,m} = \begin{cases} \dfrac{1}{H_{\tilde{h}}(l)} \tilde{h}_n^{l,m} & for \quad H_{\tilde{h}}(l) > 0 \\ 0 & otherwise \end{cases}, \tag{7.1}$$

where

$$H_{\tilde{h}}(l) = \frac{8\pi^2}{2l+1} \sum_{n=1}^{N} \sum_{m'=-l}^{l} \left| \tilde{h}_n^{l,m'} \right|^2. \tag{7.2}$$

Therefore, by using equations 7.1 and 7.2 to construct the synthesis filters, we ensure that our over-complete wavelets are invertible, as proved by Yeo *et al.* in [7].

Since our wavelet analysis filters are axis-symmetric, the forward and inverse continuous wavelet transform can be performed in the spherical harmonic domain as [7, 11]:

$$g_n^{l,m} = \sqrt{\frac{4\pi}{2l+1}} \tilde{h}_n^{l,0*} f^{l,m}, \tag{7.3}$$

where the original function f, the reconstructed function $\hat{f}$ and the wavelet coefficient g can be represented by their spherical harmonic coefficients of degree l and order m as $f^{l,m}$, $\hat{f}^{l,m}$ and $g^{l,m}$ respectively.

Since the wavelet transform is conducted in the spherical harmonic domain, in practice, we first re-interpolate the surface mesh onto a latitude-longitude grid, and then use the publicly available program S2kit [12] to perform the fast discrete spherical harmonic transform [11]. Because the latitude-longitude grid is denser near the poles than at the equator, we ensure sufficient samples at the equator to avoid aliasing.

Since the purpose of wavelet decomposition is to analyze the underlying function locally in both space and frequency, we use S2kit to transform the acquired wavelet coefficients $g_n^{l,m}$ at each level n back to the latitude-longitude grid $\{g_n(\theta_j,\phi_j)\}$. We note that the inverse spherical harmonic transform is invertible via the sampling theorem of Driscoll and Healy [11] and thus we do not lose any information by working in the spatial domain. Therefore, we can equivalently think of $\{g_n(\theta_j,\phi_j)\}$ as over-complete discrete wavelet transform.

In some cases, it might be more efficient to analyze the wavelet coefficients on a more uniform grid. In our work, we re-interpolate the wavelet coefficients samples on the latitude-longitude grid onto a subdivided icosahedron grid of high enough resolution. In our experiments, the

re-interpolating process has little effects on the analysis as long as the samples are sufficiently dense relative to the size of the geometric features of interest.

7.2.2 Rotation Invariance and Aliasing

A – Rotating the surface

For the purpose of shape analysis, we apply the wavelet transformation to the individual coordinate functions $x(\theta_i,\phi_i)$, $y(\theta_i,\phi_i)$ and $z(\theta_i,\phi_i)$ separately. Since both the bi-orthogonal and the over-complete spherical wavelet transforms are linear, we can show that

$$\begin{aligned}&\Phi(R([x(\theta_i,\phi_i);y(\theta_i,\phi_i);z(\theta_i,\phi_i)]))\\&=R(\Phi([x(\theta_i,\phi_i);y(\theta_i,\phi_i);z(\theta_i,\phi_i)]))\end{aligned} \tag{7.4}$$

where Φ denotes the wavelet transform and $R(\cdot)$ denotes a rotation operator that rotates a point in 3D. Applying $R(\cdot)$ to $\{x,y,z\}$ therefore rotates the surface in 3D.

Equation 7.4 implies that rotating a surface before the wavelet transformation is the same as applying a rotation after the wavelet transformation. Hence, both the bi-orthogonal and over-complete wavelet transforms are invariant under the rotation of 2D closed surfaces.

B – Rotating the surface parameterization

In contrast, the bi-orthogonal wavelet transform is not invariant under rotations of the surface parameterization, as demonstrated in the beginning of this chapter. This is because at each subsequent lower frequency level (coarser resolution), the input to the bi-orthogonal wavelet transform is implicitly a smooth sub-sampled version of the original function, as introduced in Chapter 2. However, despite the smoothing, the number of samples is insufficient to prevent aliasing. Therefore, when the surface parameterization is rotated, the sub-sampled spherical function and thus the wavelet coefficients can change substantially. As a result, the bi-orthogonal wavelet coefficients are not invariant under rotations of the surface parameterization, and the shape analysis results based on the bi-orthogonal wavelet transform depend on the arbitrary choice of the parameterization frame (origins and axes).

Because the bi-orthogonal spherical wavelet transform is computed implicitly rather than defined via sampling of the continuous convolution between a spherical function and the wavelet kernels, it is not trivial to artificially increase the number of samples at each level. Conversely, the over-complete spherical wavelets are invariant under the surface parameterization since each level of the wavelet transform is sufficiently sampled.

Specifically, for the over-complete wavelet transform, we compute the wavelet coefficients g_n at level n by convolving the spherical function f with level n analysis filter $\tilde{h}_n$. Since the analysis filter is axis-symmetric, we can compute the convolution in the spherical harmonic domain as shown in equation 7.3 [13]:

Let Df be the rotation of the parameterization of a spherical image f by D. It can be shown that

$$(Df)^{l,m}=\sum_{|m'|\le l} D_l^{mm'} f^{l,m'}, \tag{7.5}$$

where $D_l^{mm'}$ denotes the Wigner-D function associated with the rotation D [13]. Combining equations 7.3 and 7.5, we obtain:

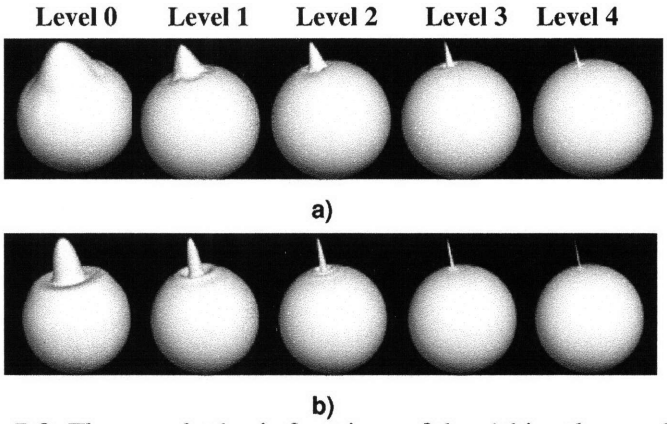

Figure 7-2: The wavelet basis functions of the a) bi-orthogonal and b) over-complete spherical wavelets at frequency levels 0-4.

$$\begin{aligned}\sqrt{\frac{4\pi}{2l+1}}\tilde{h}_n^{l,0*}(Df)^{l,m} &= \sqrt{\frac{4\pi}{2l+1}}\tilde{h}_n^{l,0*}\sum_{|m'|<l} D_l^{mm'} f^{l,m'} \\ &= \sum_{|m'|<l} D_l^{mm'}\sqrt{\frac{4\pi}{2l+1}}\tilde{h}_n^{l,0*} f^{l,m'}. \\ &= \sum_{|m'|<l} D_l^{mm'} g^{l,m'} = (Dg_n)^{lm}\end{aligned} \tag{7.6}$$

Therefore, the over-complete wavelet transform is invariant under rotations of the underlying coordinate system. Although we sample the resulting wavelet coefficients as described in Section 7.2.1, the sampling theorem of Driscoll and Healy [11] ensures the process is lossless. Therefore the over-complete discrete wavelet transform is also rotationally invariant up to the spacing of the sampling grid. In practice, we over-sample to locate regions of interest to within the accuracy of the original surface parameterization.

7.2.3 Cortical Surface Shape Representation based on Over-complete Spherical Wavelets

For the bi-orthogonal wavelets used in this work, we employ the butterfly subdivision scheme and a lifting algorithm to ensure that the constructed wavelet function has one vanishing moment [3], as described in Chapter 2. Before applying the forward wavelet transform, we first sample the registered white matter surface to an icosahedron at subdivision level 7 because it has a total number of 163,842 vertices and is thus sufficiently dense to represent the white matter surface reconstructed from ~1 mm isotropic MRI, which typically has about 120,000 vertices. Following the widely used convention, we index the resulting wavelet basis functions from level -1 to 6, and plot part of them in Figure 7-2 a).

For the over-complete wavelets, the smallest scale analysis filter is chosen to be the Laplacian of a Gaussian function with width 0.002 radian on the latitude-longitude grid. The wavelets at coarser levels are constructed by dilating the smallest scale wavelet subsequently by a factor of 2 each time. We index our over-complete wavelets from level -2 to 5 in order to match the spatial scales of the

bi-orthogonal wavelets at the same levels, as shown in Figure 7-2 b). Before conducting the over-complete wavelet transform in the spherical harmonic domain, we first sample the white matter surfaces onto a latitude-longitude grid of 10^6 points and then transform them to the spherical harmonic domain using S2kit [12].

To illustrate the advantage of over-complete wavelets over the bi-orthogonal wavelets in shape analysis, we compare the results of cortical folding development study using both wavelets in the following sections.

7.3 Folding Development Study Based on Over-complete Wavelets

7.3.1 Experimental Setup

The same dataset studied in Chapter 5 is used to build cortical folding development models based on the over-complete wavelets. This dataset consists eight normal neonates with different corrected gestational ages (cGA) from 30.57 to 40.43 weeks, and 3 children who were 2, 3 and 7 years old. The white/gray matter surfaces (white matter surfaces) are reconstructed, mapped onto a sphere, and registered in the spherical coordinate system as described in Chapter 5.

In order to compare the bi-orthogonal and the over-complete wavelets in the cortical shape analysis, we generate a second set of white matter surfaces where the underlying spherical coordinate system is rotated by 30 degree around the x- and y- axes respectively. Finally, we apply these two wavelet transformations to the white matter surfaces with both the original and the rotated parameterizations to study the influence of this rotation on the results of folding development study.

7.3.2 Cortical Folding Development Model

In this section, we briefly reintroduce the cortical folding development models we developed in the wavelet domain [1]. As described in Chapter 5, if $w(t_i)$ is one of the spherical wavelet features extracted from a subject of age t_i, we use a Gompertz curve to model the evolution of this feature with age as follows:

$$w(t_i) = g_1 e^{-e^{(-g_2(t_i-g_3))}} + \varepsilon(t_i), i = 1,\ldots,11 \tag{7.7}$$

where g_1 is the maximum value at maturation, g_2 is the growth rate that quantifies the speed of the folding development, g_3 is the inflexion point that indicates the age of the fastest folding development, and $\varepsilon(t_i)$ represents additive zero-mean noise.

Due to the limited number of subjects available in this study, we apply a regularization framework for estimating parameter g_1, g_2 and g_3 to avoid overfitting. We adopt a quasi-Newton method based on the Broyden-Fletcher-Goldfarb-Shannon (BFGS) approximation to estimate parameters $\{g_i\}_{i=1,..3}$. We calculate the R^2 statistic, the ratio of the sum of squares explained by the model and the total sum of squares around the mean to measure the goodness-of-fit of this model. We apply this regularized Gompertz model to study cortical folding development at different spatial resolutions in newborns based on the two types of spherical wavelets.

7.3.3 Overall Folding Development Study

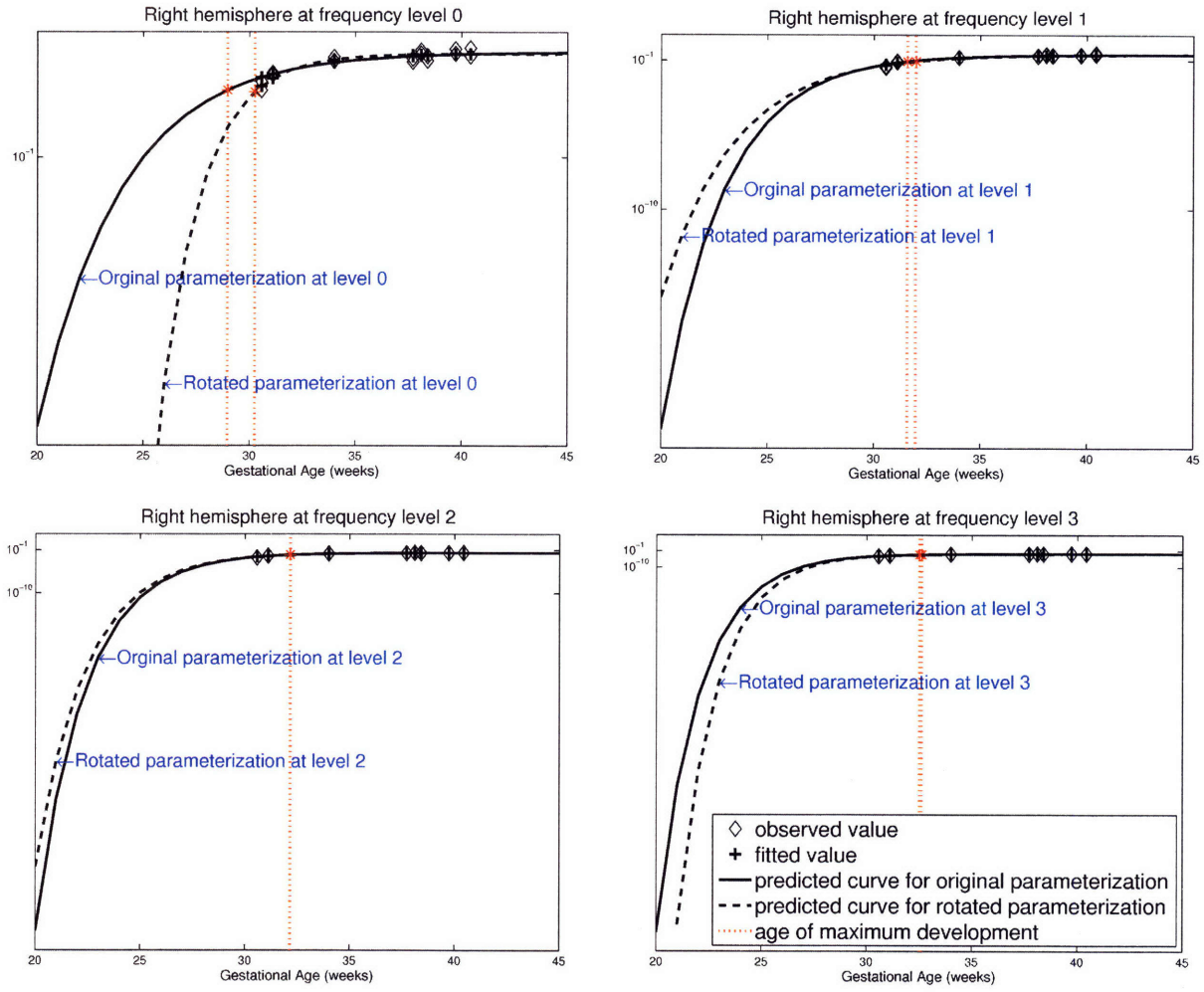

Figure 7-3: Comparison of the predicted cortical folding development curves using surfaces with rotated parameterizations based on bi-orthogonal spherical wavelets. The curves are estimated using wavelet power at frequency levels 0 to 3 of the right hemisphere. Horizontal axis is the gestational age up to 45 weeks and vertical axis is the wavelet power with a logarithmic (base 10) scale.

We first fit the folding development model to the wavelet power, which is the sum of squares of the l^2-norm of each wavelet coefficient, i.e., the sum of squares of its x, y and z components, at each frequency level. We study the wavelet power to quantify changes of the overall cortical folding with time at different spatial scales.

As a result, we find that the wavelet power based on both bi-orthogonal and over-complete wavelets fit very well with the regularized Gompertz model at all levels. For both the original and rotated surface parameterizations, the estimated maximum folding development age increases monotonically with frequency level, and the estimated development speed increases with frequency at some of levels as well. These results indicated that the larger scale cortical folds develop earlier, but with a slower speed, which is consistent with our previous observation in Chapter 5.

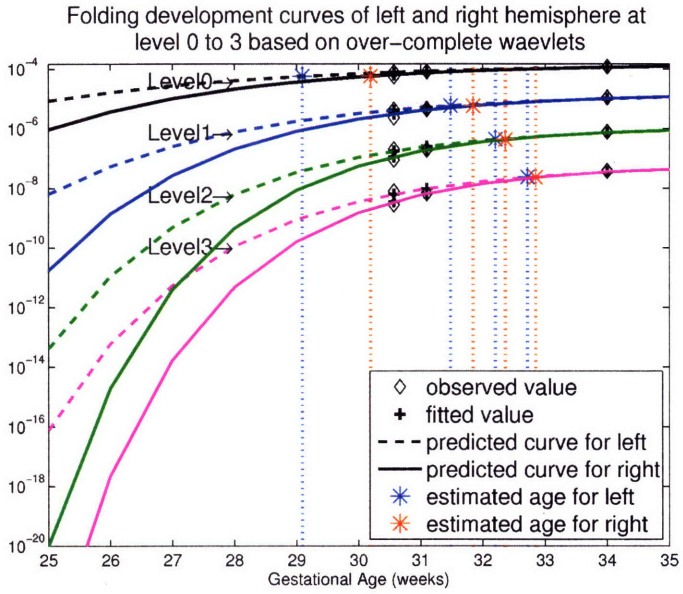

Figure 7-4: Predicted cortical folding development curves using wavelets power based on over-complete spherical wavelets for the left and right hemispheres at frequency levels 0 to 3 (the horizontal axis is the gestational age up to 35 weeks; the vertical axis is the wavelet power with a logarithmic (base 10) scale). The curves are invariant to the rotation of surface parameterization.

A – Rotation changes model parameters estimated with bi-orthogonal wavelets

However, the estimated parameters based on the bi-orthogonal wavelets vary with the rotation of the surface parameterization. As an example, Figure 7-3 shows that estimated Gompertz curves change significantly with the rotation. We can also see that this effect is more pronounced at the lower frequency levels since the surface is more severely sub-sampled at coarser resolutions. Here we present the results for the right hemisphere. We also observe the same effect for the left hemisphere.

Since the over-complete wavelet transform is invariant under rotations of the surface parameterization, the resulting wavelet coefficients are only minimally altered by sampling on the latitude-longitude grid. The estimated folding development curves using over-complete wavelets remain unchanged under the rotation. Since the estimated development curves are virtually identical for the rotated representation, we choose to omit them for presentation.

B – Over-complete wavelets reveals the hemispheric developmental asymmetry

Furthermore, when we apply the bi-orthogonal wavelets to the white matter surfaces with rotated parameterization, we observe that the estimated maximum development age of the left hemisphere is younger than the right hemisphere at some frequency levels. However, this phenomenon is not preserved with the rotation of the surface parameterization using the bio-orthogonal wavelets.

On the other hand, using the over-complete wavelets, we can clearly appreciate at all frequency levels that the left hemisphere leads the development of the right hemisphere, as shown in Figure 7-4. Although this finding has not been previously reported, it could potentially provide more

insights into the study of cortical folding development.

These results show that the rotation-variant property of the bi-orthogonal wavelets presentation can lead to unstable shape analysis results of the cortical surfaces, and conceal important neurological findings.

7.3.4 Regional Difference of Folding Development

Next, we fit the sum of squares of the x, y and z components of every single wavelet coefficient across 11 subjects to the cortical folding development model. With this approach, we can discover not only when, but also where the folding of the white matter surface occurs at different spatial scales. Note that in Chapter 5, we modeled each of the x, y and z components separately, and selected the one with the largest R^2 value to demonstrate the result. By using the sum of squares in this chapter, we robustly detect developing regions by sacrificing the sensitivity.

Since the bi-orthogonal wavelets are directly constructed on the level 7 subdivided icosahedron mesh, we can take the wavelet coefficient that has a good fit to the folding development model ($R^2 > 0.5$) as the center of folding development region. However, since the over-complete wavelet transform is on the latitude-longitude grid, their wavelet coefficients are re-interpolated to a level 7 subdivided icosahedron. At each frequency level, we segment connected regions of the coefficients that have a $R^2 > 0.6$, and then select the vertex corresponding to the maximal R^2 in each smoothed region as the center of an effect of folding development.

For each of the detected development centers, we determine the support region that represents 99% of the total energy of the associated wavelet basis function.

To visualize these results, we superimpose the support regions of these selected wavelet coefficients on the youngest newborn white matter surface and color code them to reflect the estimated development speed and age of the corresponding wavelet coefficients, as shown in Figure 7-5. For points in the overlapped support regions of two or more wavelet basis functions, color is assigned based on the estimated age and speed of the nearest wavelet basis function.

As shown in the top two rows of Figure 7-5, using the bi-orthogonal wavelet, different cortical growth regions are detected before and after the rotation of surface parameterization. In contrast, using the over-complete wavelet, the detected regions of growth are slightly affected by the rotation of the underlying spherical coordinate system, as shown in the bottom two rows of Figure 7-5.

Furthermore, comparison of the colormaps generated based on both wavelets shows that more cortical regions are detected to fit well with the Gompertz curve by using the over-complete wavelets. This result is consistent with our visual inspection and the wavelet power study results, suggesting that over-complete wavelets are more sensitive for detecting regions of growth presented in this dataset. However, we are still exploring other methods to account for the grey regions that do not fit well with the current cortical folding development model.

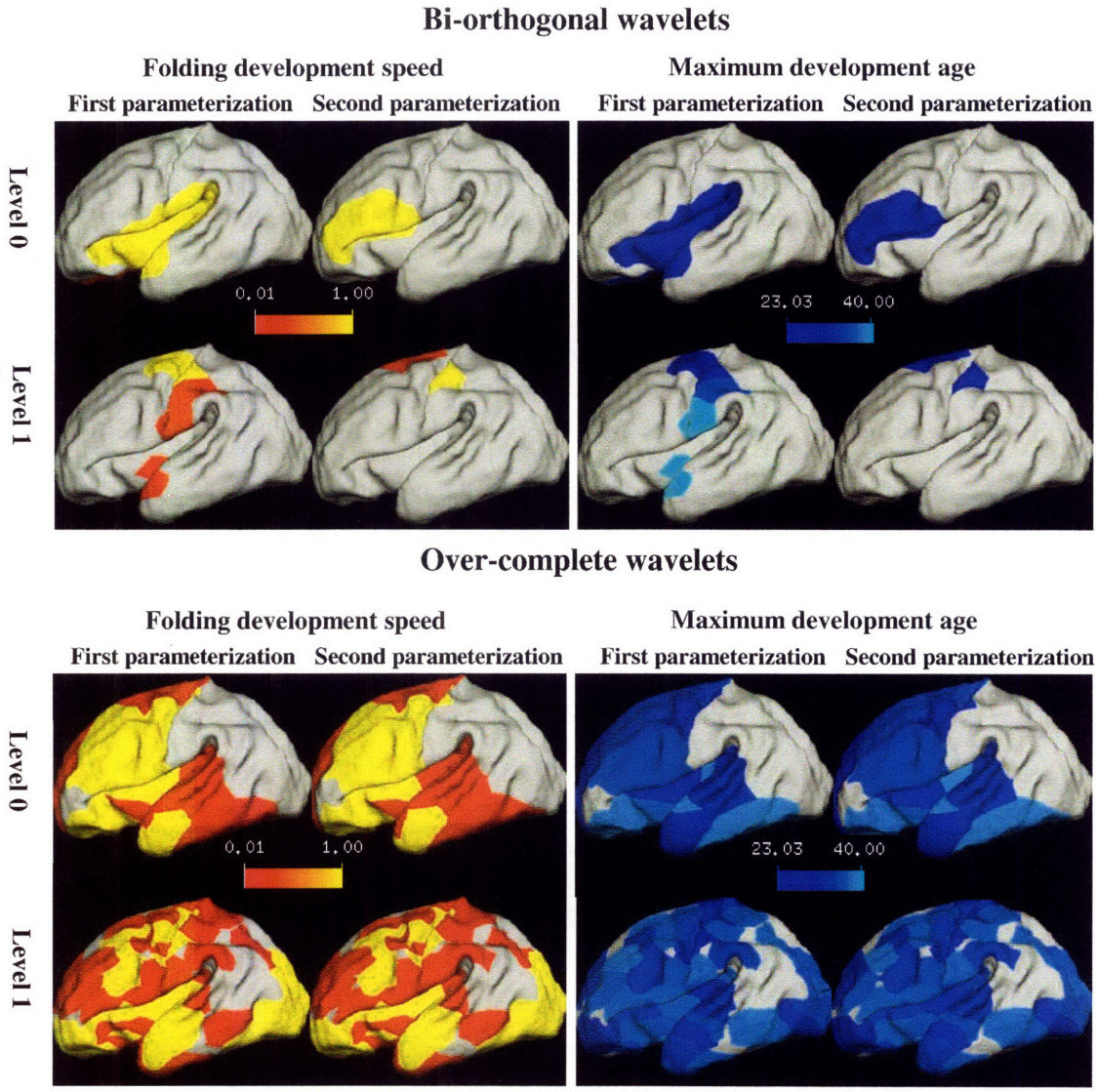

Figure 7-5: The estimated folding development speed and maximum development ages for the left hemisphere using individual wavelets at different frequency levels. Colormaps encode the estimated development speed (1/week) and age of maximum development (weeks) of selected wavelet coefficients in the support regions of their corresponding wavelet basis functions. For points in the overlapped regions of two or more wavelet basis functions, the estimated age and speed of the closest wavelet function is assigned. Rows 1-2: Estimated folding development speed and age at frequency levels 0 and 1 (top-down) of the original and reparameterized white matter surfaces (left-right) based on bi-orthogonal wavelets; Rows 3-4: Estimated folding development speed and age at frequency levels 0 and 1 (top-down) of the original and reparameterized white matter surfaces (left-right) based on over-complete wavelets.

7.4 Contributions

We demonstrate in this chapter that the over-complete spherical wavelets have significant advantages over bi-orthogonal spherical wavelets in the analysis of the geometric properties of cortical surfaces because of their invariance under rotations of the coordinate frame used to parameterize the 2D closed surfaces.

In summary, the contributions of our work presented in this chapter are the following:

1) We proposed to improve on the wavelet-based shape representation by employing the over-complete spherical wavelet transformation.

2) We built folding development models using over-complete wavelets in a dataset of newborn. The models reveal the hemispheric developmental asymmetry in the folding development, in addition to the speed, age and frequency correlation previously disclosed using the bi-orthogonal wavelets. Furthermore, we detected a wider array of regions of folding development using the over-complete spherical wavelet transform compared to the bi-orthogonal wavelets.

Preliminary results in this chapter demonstrated that the use the over-complete wavelet in shape analysis of neuroanatomical structures can greatly benefit the study of localized shape changes associated with age, gender, hemisphere and neurological diseases.

A preliminary version of this work was presented at the *IEEE Computer Society Workshop on Mathematical Methods in Biomedical Image Analysis* in conjunction with *IEEE International Conference on Computer Vision (reference)*[14].

Bibliography

[1] P. Yu, P. E. Grant, Y. Qi, X. Han, F. Segonne, R. Pienaar, E. Busa, J. Pacheco, N. Makris, R. L. Buckner, P. Golland, and B. Fischl, "Cortical surface shape analysis based on spherical wavelets,," IEEE Transaction on Medical Imaging, vol. 26, pp. 582-598, 2007.

[2] D. Nain, S. Haker, A. Bobick, and A. Tannenbaum, "Multiscale 3-d shape representation and segmentation using spherical wavelets," IEEE Transaction on Medical Imaging, vol. 26, pp. 598-618, 2007.

[3] P. Schroder and W. Sweldens, "Spherical wavelets: Efficiently representing functions on a sphere," Proceedings of the 22nd annual conference on Computer Graphics and Interactive Techniques, vol. 29, pp. 161-172, 1995.

[4] E. Simoncelli, W. Freeman, E. Adelson, and D. Heeger, "Shiftable multi-scale transforms," IEEE Transaction Information Theory, vol. 38, pp. 587-607, 1992.

[5] J.-P. Antoine and P. Vandergheynst, "Wavelets on the 2-sphere: a group-theoretical approach," Applied and Computational Harmonic Analysis, pp. 262-291, 1999.

[6] I. Bogdanova, P. Vandergheynst, J.-P. Antoine, L. Jacques, and M. Morvidone, "Stereographic wavelet frames on the sphere," Applied and Computational Harmonic Analysis, vol. 223-252, 2005.

[7] B. T. T. Yeo, W. Ou, and P. Golland, "On the construction of invertible filterbank on the 2-sphere," Technical Report, http://people.csail.mit.edu/ythomas/IFB2006.pdf, 2006.

[8] C. Brechbuhler, G. Gerig, and O. Kubler, "Parametrization of Closed Surfaces for 3-D Shape Description," Computer Vision and Image Understanding, vol. 61, pp. 154-170, 1995.

[9] B. Fischl, M. I. Sereno, and A. M. Dale, "Cortical surface-based analysis. II: Inflation, flattening, and a surface-based coordinate system," Neuroimage, vol. 9, pp. 195-207, 1999.

[10] L. Staib and J. Duncan, "Model-based deformable surface finding for medical images," IEEE Transactions on Medical Imaging, vol. 15, pp. 720-731, 1996.

[11] J. Driscoll and D. Healy., "Computing Fourier transforms and convolutions on the 2-sphere," Advances in Applied Mathematics, vol. 15, pp. 202 - 250, 1994.

[12] P. Kostelec and D. Rockmore., "A lite version of spharmonic kit," http://www.cs.dartmouth.edu/geelong/sphere/.

[13] J. Sakurai, Modern Quantum Mechanics: Addison-Wesley, 1994.

[14] P. Yu, B. T. T. Yeo, P. E. Grant, B. Fischl, and P. Golland, "Cortical folding development study based on over-complete spherical wavelets," Proceedings of the IEEE International Conference on Computer Vision,, 2007.

Chapter 8

Conclusion

This dissertation concerns the accurate and parsimonious shape representation of neuroanatomical structures, such as the cerebral cortex and the hippocampus, as well as shape-based statistical analysis in order to discover shape changes related to neurodevelopment, neurodegeneration, and neurological disease. We have made a number of contributions to advance several aspects of the field of computational anatomy and offer new research perspectives.

On the theoretical level, we introduced the concept of localized and multi-resolution shape representation into the morphological analysis of neuroanatomical structures, and studied the properties of this shape representation by using different kinds of spherical wavelets. On the methodological level, we developed novel statistical analysis frameworks to study the patterns and spatial scales of shape variations in normal populations, discriminate the shape changes associated with neurological diseases in group comparison studies, and modeled the temporal development of cortical folding in neurodevelopment. In addition, we developed a shape-guided segmentation method by incorporating shape constraints derived from the multi-scale shape representation. On the application level, we have applied the developed statistical analysis framework to the analysis of the shape of cortical surfaces, and brought out interesting neurological findings. We also applied a shape-guided surface deformation model to improve the segmentation accuracy of the hippocampus, an important subcortical structure in the human brain. To the best of our knowledge, no techniques have been previously introduced to extract multi-scale and localized shape features of the cortex, and to investigate simultaneously the locations and spatial extents of cortical folding variation with sound statistical principles.

The concept of localized and multi-resolution shape representation combines the advantages of the previously developed shape representation methods that are either multi-resolution or localized. By transforming the 2D closed surface of neuroanatomical structures using spherical wavelets, we obtain new shape features that represent the surface at multiple spatial scales and locations, We first developed a method to extract normalized shape features for a set of surfaces based on a bi-orthogonal spherical wavelet transformation, and proved that it can characterize shape variations more concisely compared with the global shape representation method based on spherical harmonic

descriptors. We further investigated the use of over-complete wavelets in our multi-scale and localized shape representation scheme, and demonstrated that this new wavelet transformation can provide more accurate and stable shape features, with a minor increase to the computational expense and complexity. In particular, our method offers a new way to analyze the convoluted shape of the surface of the cerebral cortex in multiple local regions and at multiple spatial scales across the whole surface.

Based on this shape representation, we developed a set of statistical analysis frameworks and applied them to study the shape of cortical surfaces derived from Magnetic Resonance Imaging (MRI) data. First, we developed multi-resolution shape models in the wavelet domain using Principal Component Analysis (PCA) and studied cortical shape variations in an elderly normal population. In this study we detected and visualized the most prominent patterns of shape variations in a large sample of the population. By studying the correlation of these shape variations with age, gender and a set of neuropsychological scores, we found that cortical shape variation is significantly correlated with age in the female group. We then developed a method for detecting the cortical folding differences between two groups of subjects in a classification framework. We showed that a Bayesian classification method based on predicted Automatic Relevance Determination (pred-ARD) outperforms one of the classical classification methods, Support Vector Machines (SVMs), in our shape-based patient classification study. This framework has been applied to several MRI datasets and demonstrated to generate promising classification accuracy. Thirdly, we developed nonlinear temporal models for quantitatively studying the development of cortical folding at coarse and progressively finer spatial resolutions in a dataset of newborn based on the wavelet transformation. We employed a regularization framework to improve prediction performance on novel MRI scans and developed an efficient method for model estimation. In summary, these statistical analysis frameworks can be used to detect multi-resolution shape variations in a population, localize shape changes caused by neurological disease, and predict abnormal cortical surface folding development.

Finally, we developed a surface deformation procedure for improving the segmentation of subcortical structures, such as the hippocampus, based on image models and multi-scale shape constraints in the wavelet domain obtained from training set. Our method extends the previous work in this direction by employing more comprehensive image models and allowing the shape to deform outside the space spanned by the training set. We demonstrated an improvement of segmentation accuracy using our method, in spite of imperfections in MR images.

The multi-scale and localized shape representation can benefit several research areas that rely on shape information, such as shape analysis, image segmentation, and image registration. Here, we highlight some potential directions for future research in these fields.

In our work, we use the wavelet transformation of coordinates to represent the shape, motivated by the fact that the coordinates contain the fundamental shape information, and other geometric features such as curvature can be derived from them. However, the developed procedure can also be applied to other features that are measured for every point on the surface, such as curvature and cortical thickness. By decomposing these measures using wavelets, we can obtain a multi-scale representation of the feature, which can replace the prevailing smoothing procedures where the width of the smoothing kernel needs to be optimized in order to achieve best discrimination.

Furthermore, the new shape representation based on an over-complete spherical wavelet transformation could potentially improve the classification accuracy in the shape-based classification framework introduced in Chapter 4, since it has been demonstrated to provide more stable and sensitive shape features in the cortical folding development study.

We have performed experimental study in shape-guided segmentation by developing a surface deformation method combining shape and image information. Our results have shown that shape information can preserve the object boundary that is absent from the image due to the imperfections in MRI, and improve the segmentation accuracy. However, more work is needed in this direction to develop an improved shape prior to enlarge the subspace that the surface is allowed to deform in, and to better combine image information such as edge and intensity.

Finally, the multi-resolution shape representation can be used for object registration in a hierarchical way. This type of procedure would start with an approximate registration of the surfaces at a coarse resolution, and improve the registration accuracy progressively at smaller resolutions. Combing the multi-scale shape representation into a registration scheme can be particularly helpful for datasets with a large amount of inter-subject variability.

In conclusion, in this dissertation, we developed methods to represent the surface of neuroanatomical structures, in particular the human cortex, at multiple spatial scales and locations. Based on this shape representation, we developed a set of statistical analysis frameworks and applied them to real data for studying normal cortical shape variations, disease-associated cortical shape changes, and cortical folding development in late gestation. Additionally, we presented a shape-guided surface deformation method and tested its use in improving segmentation accuracy of the hippocampus in a MRI dataset. These developed methods are implemented and incorporated into the Freesurfer software package. These tools can be used to conduct automated shape analysis on a large-scale dataset.

APPENDIX

Publications of the Author

- **Journal Articles**

1. P. Yu, P. E. Grant, Y. Qi, X. Han, F. Segonne, R. Pienaar, E. Busa, J. Pacheco, N. Makris, R. L. Buckner, P. Golland, B. Fischl, Cortical Surface Shape Analysis Based on Spherical Wavelets, IEEE Transaction on Medical Imaging, 26(4):582-598, 2007

- **Conference Articles**

1 P. Yu, B. T. T. Yeo, P. E. Grant, B. Fischl, P. Golland, Cortical Folding Development Study Based on Over-complete Spherical Wavelets, Proceedings of the IEEE International Conference on Computer Vision, Oral presentation in MMBIA 2007, Rio de Janeiro (Oral presentation acceptance rate: 18%).

2. P. Yu, X. Han, F. Segonne, A. K. Liu, R. A. Poldrack, P. Golland, and B. Fischl, Shape-based Discrimination and Classification of Cortical surface. Oral Presentation in International Conference on Pattern Recognition 2006, Hong Kong, P.R.China, Aug. 2006 (Oral presentation acceptance rate: 15%).
3. P. Yu, X. Han, F. Segonne, R. L. Buckner, R. Pienaar, P. Golland, P. E. Grant and B. Fischl, Cortical Surface Shape Analysis Based on Spherical Wavelet Transformation. Oral presentation in IEEE Computer Society Workshop on Mathematical Methods in Biomedical Image Analysis (MMBIA 2006), New York City, NY, June 2006 (Oral presentation acceptance rate: 11%).

- **Conference Abstracts**

1 P. Yu, F. Segonne, X. Han, B. Fischl, Shape Analysis of Neuroanatomical Structures Based on Spherical Wavelets. 11th Annual Meeting of the Organization of Human Brain Mapping (HBM), June 2005, Toronto, Canada.

2 P. Yu, D. H. Salat, P. Golland, D. S. Tuch, H. D. Rosas, B. Fischl, Subdividing the Corpus Callosum Based on Morphometry and Diffusion Anisotropy. International Society for Magnetic Resonance in Medicine (ISMRM), Miami, Florida, May 2005.